MOVEMENT-INDUCED ORIENTATION OF COLLAGEN FIBRILS IN CARTILAGINOUS TISSUES

by

KEITA ITO

B. S. in Mechanical Engineering, Massachusetts Institute of Technology (1985)

S. M. in Mechanical Engineering, Massachusetts Institute of Technology (1994)

Submitted to the
Harvard-M.I.T. Division of Health Sciences and Technology
in Partial Fulfillment of the Requirements for the Degree of

DOCTOR OF SCIENCE

at the

MASSACHUSETTS INSTITUTE OF TECHNOLOGY

March 1994

Signature of Author _____
Harvard-M.I.T. Division of Health Sciences and Technology
March 3, 1994

Certified by _____
Professor Robert W. Mann
Thesis Supervisor

Certified by _____
Professor Roger G. Mark
Chairman, Graduate Committee

MOVEMENT-INDUCED ORIENTATION OF COLLAGEN FIBRILS IN CARTILAGINOUS TISSUES

by

KEITA ITO

Submitted to the Harvard-M.I.T. Division of Health Sciences and Technology
on March 3, 1994 in partial fulfillment of the requirements for the
Degree of Doctor of Science in Medical Engineering

ABSTRACT

The mechanism of collagen fibril orientation is of interest in normal cartilage, a specialized connective tissue, whose function of joint lubrication and load transmission are directly dependent on its mechanical properties. Knowledge of such a mechanism would enhance understanding of prevalent pathological conditions in cartilage and suggest remedial or preventive treatments. Unfortunately, the mechanism of collagen fibril orientation in cartilage is unknown.

In this thesis, two novel collagen fibril orientation mechanisms, shear field induced orientation and drag induced orientation, are proposed and investigated. In both mechanisms, the physical environment of the extracellular matrix (ECM), under load, directly orients collagen fibrils via physical interactions between the ECM components (without direct cellular involvement). Activities of the organism (e.g. locomotion) impose load patterns, creating fluid flow within the poroelastic tissue. This fluid flow is of the interstitial fluid with respect to the proteoglycan (PG) aggregates immobilized by the extant collagen network. If these PGs are immobilized appropriately, the flow may create channels of high permeability within the PG network. These channels would then create fluid flow shear fields which may orient newly formed loose collagen fibrils parallel to the shear field (Shear Field Induced Orientation). Regardless of channel formation, the flow may drag newly formed loose collagen fibrils through the PG/collagen (solid) network. Then, the elastic response of the solid network on the loose collagen fibril would orient the fibril parallel to its trajectory (Drag Induced Orientation).

These hypothesized but never before visualized loose unbanded multimolecular collagen filaments were isolated by irrigation of PG digested full-term fetal articular cartilage explants, and found to measure Ø10.4 ± 0.5 nm x 1.06 ± 0.03 μm. These filaments were consistent with collagen fibrils isolated from chick embryo sterna, but no immunolabelling was conducted for type identification. In addition to these filaments, larger < Ø40 nm banded fibrils were isolated with tapered ends, indicating free ends of network-size collagen fibrils.

Channel formation in ECM was investigated by electron microscopy and confined consolidation of cartilage plugs. High pressure frozen, freeze substituted, and conventionally embedded articular cartilage ECM was found to be highly sensitive to ice crystal formation and its deleterious segregation effects. However, with electron diffraction determination of ice crystal presence, acetone freeze substitution was shown to provide highly detailed ultrastructural morphology of the native PG network. Using this preparation technique, no

channels were visible in osmotically compressed cartilage plugs allowed to imbibe Ø11 nm BSA-coated gold or Ø12 nm ferritin particles. Alternatively, confined consolidation of cartilage plugs were measured to detect channel formation (velocity dependent permeability). These measurements showed no evidence to support channel formation, but demonstrated the inability of current models to account for experimentally measured differences in compression and imbibing creep. Although, strain dependent permeability alone could not account for this experimentally observed phenomenon, strain dependent equilibrium modulus in addition to strain dependent permeability was shown to provide a consistent model for both compression and imbibing creep behavior of cartilage.

Quasi-static and time dependent models were developed for the drag induced orientation mechanism in gel-like materials. This model was validated by comparison to analytical results for motion of a fiber in a viscous fluid and for sedimentation experiments in 1% gelatin. Finally, this model with known parameter values (above and literature) demonstrated the potential of drag induced collagen fibril orientation in cartilage.

Thesis Supervisor: Robert W. Mann, Sc.D.
Title: Whitaker Professor Emeritus of Biomedical Engineering

MEMBERS OF THE COMMITTEE

Dr. Robert W. Mann, Sc.D.
Whitaker Professor Emeritus of Biomedical Engineering
Senior Lecturer
Department of Mechanical Engineering
Massachusetts Intsitute of Technology

Dr. Alan J. Grodzinsky, Ph.D.
Professor
Department of Electrical Engineering
Department of Mechanical Engineering
Massachusetts Intsitute of Technology
Harvard-M.I.T. Division of Health Sciences and Technology

Dr. Mark Johnson, Ph.D.
Principal Research Engineer
Department of Mechanical Engineering
Massachusetts Intsitute of Technology

Dr. Slobodan Tepic, Sc.D.
AO/ASIF Research Institute
Davos Switzerland

Dr. Ioannis V. Yannas, Ph.D.
Professor
Department of Mechanical Engineering
Department of Material Science and Engineering
Massachusetts Intsitute of Technology

ACKNOWLEDGMENTS

To the envy of my friends and colleagues, I have probably had one of the most unusual graduate school experiences. What began as general discussions about cartilage during my brief consulting period in Davos Switzerland, blossomed into a doctoral dissertation and the opportunity to work in one of the most interesting orthopaedic research laboratories in the world, the AO/ASIF Research Institute. Of course the fact that Davos is a ski resort high in the Alps, was just a bonus and a minor distraction.

Dr. Slobodan Tepic, in Davos, and Prof. Robert W. Mann, at M.I.T., are two remarkable individuals with whom I have had the privilege of working. A devoted educator, Prof. Mann has allowed me the freedom to pursue an unusual course of research, and has tolerated my less than shining moments. While many researchers these days are only concerned about the volume of research produced, Prof. Mann has always been an advocate of research education and quality. Slobodan, thank you for your tremendous energy and bottomless well of ideas. I could not have done this without your guidance. I will always remember those late nights of "alchemy", and "Slimy" will always hold a special meaning for me. I hope that we will have many more fruitful collaborations in the future.

Most of this work was conducted in the AO/ASIF Research Institute, under the directorship of Prof. Stephan M. Perren. His unwavering support of this unusual project and its goals were invaluable. Also all of the electron microscopy work was done in collaboration with Dr. Martin Müller and Dr. Paul Walther at the Laboratorium for Electron Microscopy I at the Swiss Federal Institute of Technology. They welcomed me to their facility with open arms and showed a simple engineer both the power and limitations of electron microscopy.

Dr. Stephen Bresina, in Davos, and my old colleague through grad school, Dr. Pat Lord, both deserve special thanks. Both are special friends who have shared in the ups and downs of research. Our adventures together will always remain a part of my graduate school experience.

Much of the work presented in this thesis was done with the support of the technical staff at Davos: Emir and Claudia the photographers, illustrations by Jan Piet, Benni in the machine shop, Mike in the video studio, Röbi for ordering my unusual parts, Hausi for the endless literature searches, and Barbara for helping me cope with my bad German. Thank you all.

Finally, my family. I could not ask for a more supportive nucleus. Without the guidance of my father I would not be here. To my mother and sister, thank you for always taking care of the baby. And to Christiene, who put up with all the late nights, and constant delays. Thanks for making my life so wonderful. I hope someday, that I can do the same for you.

This research was performed in the AO/ASIF Research Institute (Davos, Switzerland), Laboratorium for Electron Microscopy I at the Swiss Federal Institute of Technology (Zürich, Switzerland), and the Eric P. and Evelyn E. Newman Laboratory for Biomechanics and Human Rehabilitation at MIT. Funding was provided in part by the following: AO/ASIF Research Institute; AO Foundation, project 91-T32; U.S. Dept. of Education, National Institute on Disability and Rehabilitation Research, Rehabilitation Engineering Center grant #133E80024; and the Harvard-MIT Division of Health Sciences and Technology.

Aan P. Noga

Hopelijk realiseer je je, dat op vlakke
bodem misschien uithoudingsvermogen
gekweekt kan worden,

maar dat karakter en kracht slechts je
deel worden indien moeilijk
begaanbare hellingen overwonnen
worden.

CONTENTS

CHAPTER
ONE

INTRODUCTION

1.1 ISSUES

Cartilaginous tissues provide lubricated surfaces for the transmission of load across the joints of the skeleton. This structural function makes the mechanical properties of cartilage of utmost importance. Although such properties are determined by both the cells and the much more abundant extracellular matrix (ECM), each contribution is distinct in a temporal sense. Since the cells produce and maintain the extracellular components, they affect the slowly evolving mechanical properties of the tissue, whereas the immediate properties are primarily determined by the ECM. The latter is a biopolymer, a fibrous network of collagen fibrils impregnated with a gel-like ground substance consisting primarily of proteoglycan (PG) aggregates, and ionized aqueous fluid. Individually, the PGs resist compressive deformations, while the collagen fibrils exhibit a significant tensile strength. Since the collagen network also inhibits the gross motion of the PGs, collagen fibril orientation within the fibrous network contributes to all mechanical properties and the function of cartilage. However, the physiological mechanisms which establish and maintain the orientation of individual collagen fibrils within the highly organized fibrous framework of normal cartilage remain essentially unknown.

1.2 OBJECTIVE

From the pioneering works of Wolff and Roux [82, 101] to modern times, teleological arguments have dominated the interpretations of the structure of load bearing tissues. While morphological studies of cartilage ECM have advanced our knowledge of the structural organization, the mechanism by which the apparently optimal organization of the ECM is attained continues to elude us. One may argue that as long as cartilage is appropriate for its function, we need not be concerned with the mechanism. However, understanding of collagen fibril orientation mechanisms is prerequisite to a rational approach to controlling the process of tissue repair e.g. optimum cartilage callus formation in fracture healing or repair of articular cartilage in osteoarthritis. Current approaches to fracture healing are mostly empirical, and not surprisingly, result in a variety of outcomes. Our ability to treat injured articular cartilage is very limited. Understanding a naturally occurring process, even to the level of being able to model it, and thus predict its response to external stimuli, is no guarantee for successful control, but no rational approach to control is possible without such understanding.

1.3 BACKGROUND

Articular cartilage is a shiny smooth tissue, 1-5 mm thick, covering the articular surfaces of bones in diarthroidal joints. The tissue is aneural and avascular. It is sparsely populated by chondrocytes and consists primarily of ECM. Although the cells and matrix are functionally interdependent, they are structurally separate (chondrocytes synthesize matrix components, but do not affect mechanical properties in and of themselves). Hence in biomechanical terms, cartilage (i.e. its ECM) is a poroelastic material, consisting of an organic solid matrix and interstitial aqueous fluid.

Normal mature cartilage is composed of 65-75% w/w water [54, 100], containing a variety of electrolytes. The solid matrix is composed predominantly of collagen fibrils (65% dry weight) [70], of mostly type II with some type IX and XI. The fibrils are organized in a highly specific architecture which is separated into four depth zones [15, 59]. The superficial tangential zone (STZ), nearest the articular surface, consists of collagen fibrils arranged tangential to the surface with the lamina splendans, a woven sheet of almost purely collagen fibrils, at the actual surface. The fibrils in this zone appear to be aligned, within the tangential plane, to the split-line patterns (splits created by crack propagation induced by puncturing the surface with an awl)[11]. In contrast the collagen fibrils in the middle zone (MZ), just below

the STZ, are randomly oriented and larger in diameter. In the deep zone (DZ), the collagen fibrils are largest in diameter and are oriented perpendicular to the tidemark, the calcified cartilage border. These fibrils continue into the calcified zone (CZ), crossing the tidemark and anchoring the tissue to the bone. Finally, the other major component of the solid matrix is proteoglycan aggregates, which comprise 20-30% of the dry weight [70]. These large macromolecules are up to 200×10^6 MW and ~2 μm in length [80]. They are composed of PG monomers (subunits) bound to hyaluronate backbones with a stabilizing link protein [30]. The PG subunits themselves are composed of 50-100 mostly chondroitin sulfate with few keratan sulfate, glycosaminoglycans (GAGs) covalently bound to the core protein. The organization of the solid matrix is that of a coarse fibrous collagen network within which the PG aggregates form an entangled fine molecular network. These PG aggregates are immobilized by the collagen network in which they are both entangled and possibly ionicly bound [66, 72, 76], Figure 1.1.

The stiff collagen network dominates the tensile response of cartilage, but is unable to withstand compressive forces due to the high aspect ratio of the collagen fibrils. The PGs

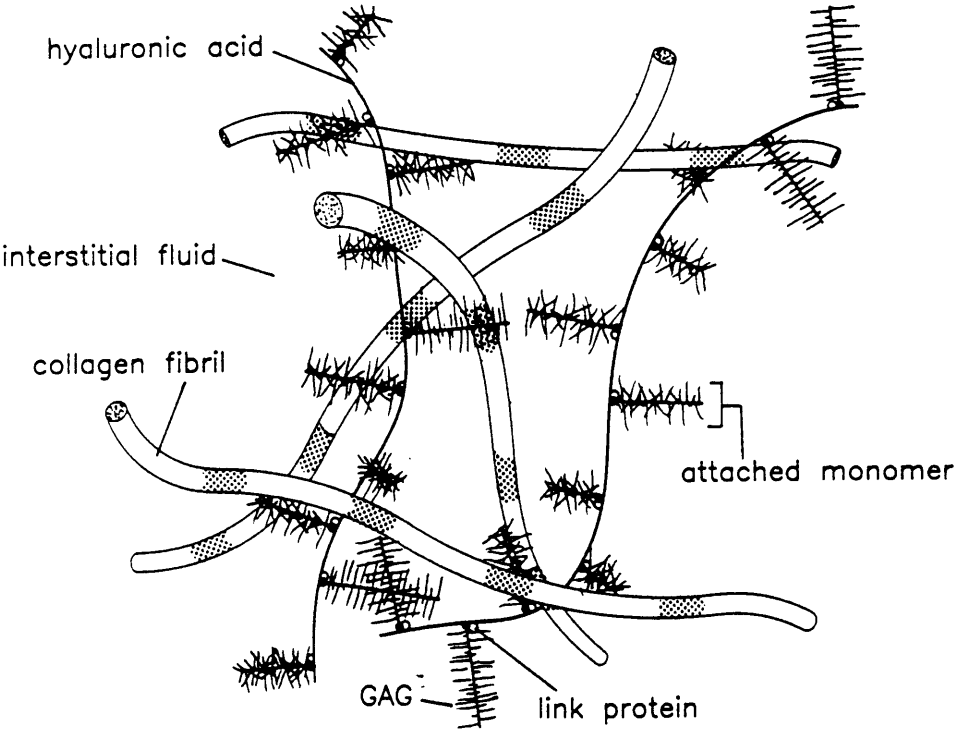

Figure 1.1 Illustration of the molecular organization of cartilage ECM.

serve this latter function. They contain many negatively charged sulfate groups on the GAGs which, along with the freely mobile ions in the interstitial fluid, give the tissue a high capacity to swell (Donnan osmotic pressure) [49] and to resist the movement of interstitial fluid. This internal osmotic pressure can range up to 0.2 MPa [51], and, in the uncompressed state, preloads the collagen network under a tensile stress because the PGs are limited to as little as 20% of their fully expanded state by the collagen network [28]. When compressive loads are applied, the solid matrix is deformed exuding the interstitial fluid (Figure 1.2)[57]. At equilibrium, the load is balanced again by the osmotic pressure of the more densely compressed PGs. However, these osmotic pressures are insufficient to withstand the higher transient loads which are instead carried by the PG resistance to ionized interstitial fluid motion. This resistance to fluid motion in the compressed cartilage of joints is sufficient to form local interarticular seals [94] which can support *in vivo* measured transient loads as high as 18 MPa [32]. Although collagen fibrils are themselves unable to withstand compressive loads, they immobilize the entangled PGs with respect to the movement of interstitial fluid, thus influencing, not only the tensile properties, but all aspects of cartilage mechanical properties and thus function.

Collagen molecules are composed of three polypeptide chains, called α-chains. These chains are twisted into a triple helix to form a stiff rope-like molecule, Ø1.5 x 300 nm long. After secretion into the ECM as procollagen, the propeptide regions are removed by specific proteolytic enzymes. These tropocollagen units then associate in the ECM to form larger collagen fibrils. The individual molecules are packed lengthwise within the fibril leaving a gap of 35 nm from the end of one molecule to the end of the next molecule. They also have a staggered packing arrangement between adjacent molecules which displaces them longitudinally by almost one quarter of their length (67 nm) and gives rise to the cross-striation patterns seen in larger collagen fibrils (> Ø30 nm) viewed with negative staining on an electron microscope [72].

Hypotheses on the control of collagen fibril orientation have been approached from two separate disciplines: biological and biomechanical. The typical biological view is centered on the cell. Birk and Trelstad have presented morphological evidence indicating cellular control of fibril orientation in chick embryo cornea [5, 6]. They contend that collagen fibrils are formed within small cellular surface recesses which laterally fuse with other recesses to form collagen lamellae and bundles, thereby determining the architecture of the collagen network. However, no mechanistic evidence has been correlated with their morphological interpretations. Although their theory is plausible for the organization of the ECM near the

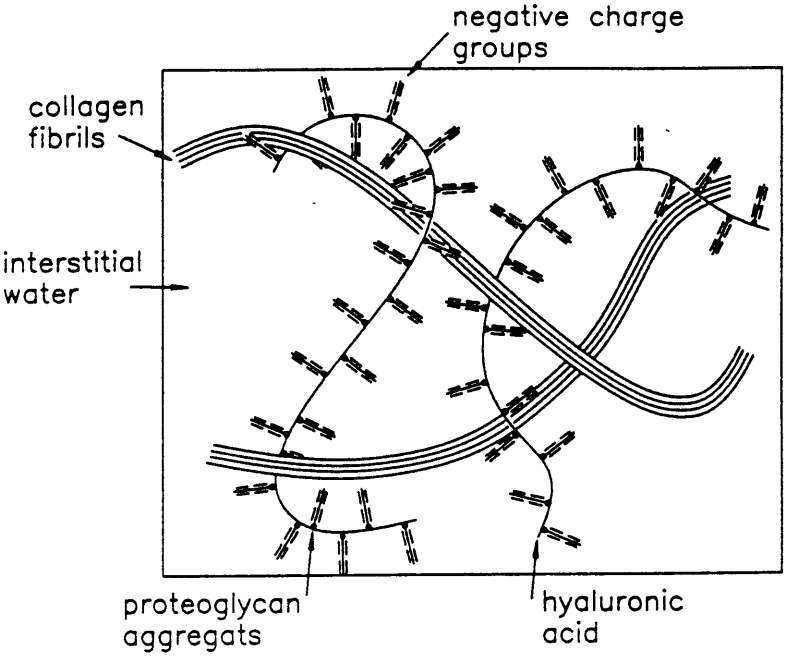

(a)

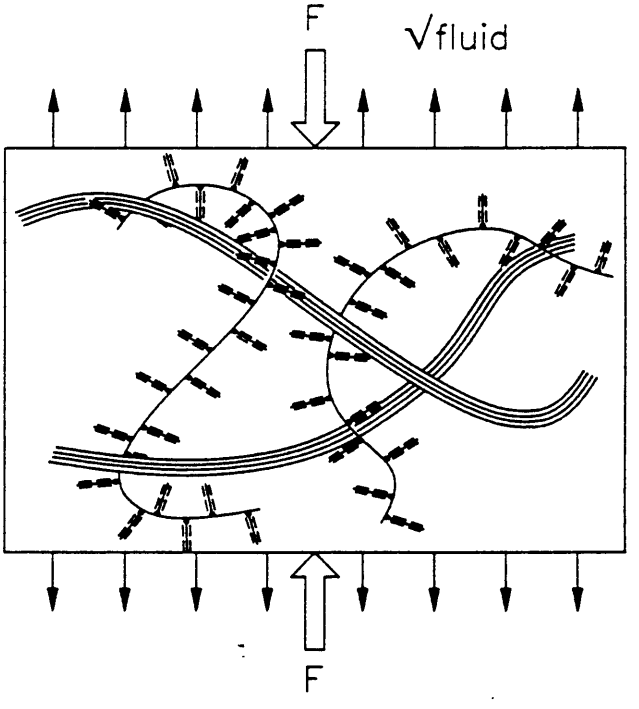

(b)

Figure 1.2 Schematic representation of cartilage depicting a porous solid matrix of collagen and proteoglycan aggregates swollen with water; (a) unloaded and (b) under load.

cells (pericellular matrix) and in cellularly dense tissue, it is difficult to envision the means by which chondrocytes could orient fibrils in cartilage ECM when the tissue is so sparsely populated by cells and experiences repetitive deformation of its solid network and flow of its interstitial fluid. Alternatively, molecular biological views address this issue. The molecular attributes of collagen secreted by the chondrocyte may determine the organization of the network far away from the cells (interterritorial matrix) [21]. The main challenge to this hypothesis is the local variability of the network organization, i.e. orientation of the collagen in the STZ varies within the joint to such an extent that collagen molecules separated by only a small distance would be required to carry different attributes. In addition, if a collagen molecule carried attributes to determine its orientation, it must be only relative to its surroundings, but the problem of placement with respect to global coordinates (e.g. depth zones) is left unresolved.

In biomechanics, the prevalent approach has been that cartilage is optimal and the task is to find the criteria of optimality which will match the morphological attributes of the ECM. The investigations to date have shown that this optimal criteria may act through the physical environment of the ECM. Pauwels and his collaborators contend that collagen orientation in cartilage reflects its role as the tension resisting element [77]. Split-line patterns, from fifty glenoid cavity cartilage specimens were correlated to the stress patterns from photoelastic gels with corresponding geometrical and material defects. Although no mechanisms were presented, they suggest that the distribution of tension in the ECM *per se* orients the collagen. This investigation implies that stress in the ECM is the optimality criteria, but unless the orientation mechanism can be understood, it is difficult to apply this theory. While a biological system may indeed function governed by principles of optimality when intact, our intervention to treat it when it fails (e.g. fracture treatment or prosthetic replacement) may be misguided by assumptions of optimality. With normal conditions changed by injury or pathology, even a seemingly correct criterion may lead our treatment efforts in the wrong direction. Thus, it is not enough to identify the optimality criteria, but the mechanism must also be understood.

Observations from other investigations indicate that collagen fibril architecture may be controlled by the physical environment of the ECM. Stopak *et al* [89], using a developing chicken limb bud model, concluded that forces exist within embryonic tissues which can arrange extracellular matrices into anatomical patterns. Fluorescently labeled type I collagen fibrils digested from rat tail tendons were injected near the developing shaft of a long bone. By confronting the embryo with preformed collagen fibrils, mechanisms occurring during

collagen deposition were avoided, yet these exogenous fibrils were found properly incorporated within the normal connective tissues of the developed wing. Again, no mechanisms were hypothesized, but the role of a feedback signal was apparent in their model. O'Conner *et al* found that split-lines on the rat femoral condyles are well defined only in the major load bearing areas of the articular surface [73]. Tepic, comparing the femoral head of a newborn calf to that of a mature cow, found that these split-lines develop postnatally [94]. Also, both Woo [102] and Roth [81] report anisotropic tensile properties (reflecting an ordered collagen fibrillar architecture) as much more isotropic in skeletally immature compared to mature cartilage. The work of Tepic, Roth and Woo all indicate that collagen orientation develops during the post-natal growth period, and before skeletal maturity. Assuming smaller joint loads *in utero*, these observations are all consistent with the hypothesis that collagen orientation in cartilage is driven by forces generated within the ECM by physiological joint loads.

This type of mechanism is also teleologically appealing. A mechanism, in which the morphology and hence the load bearing function of the tissue is directly controlled by the load itself is optimal and is consistent with the simple yet elegant control mechanisms prevalent in biology. Thus, for this study, an acellular mechanism driven by the forces within the ECM was identified as the most likely class of control mechanism for collagen orientation in cartilage.

1.4 APPROACH

Cartilage is poroelastic and its loading entails fluid movement as well as deformation. In this thesis, it is proposed that collagen orientation is induced by interstitial fluid movement, and two novel mechanisms are presented: (i) orientation of collagen fibrils induced by their movement through the gel-like medium of the fluid-saturated PG network, (ii) orientation of collagen fibrils by flow-induced interstitial fluid shear fields. In the former, orientation arises through the elastic interaction of the fibril and the PG network, while the driving force is the viscous drag of the fluid against the fibril (drag induced orientation, DO). In the latter, although global tissue flows do not generate shear fields of sufficient intensity, flow channels created through the process of flow-induced PG network disentanglement could generate local collagen-network-scale velocity gradients (shear flow induced orientation, SFO).

Since present knowledge of the physical properties and interactions among the ECM components are insufficient, and their determination is not within the scope of this thesis,

undeniable demonstration of these hypotheses is not possible. Nevertheless, their mechanistic potentials are demonstrated, and in the process, knowledge of the physical interactions among ECM components in all cartilaginous tissues are expanded.

1.5 THESIS OVERVIEW

This section contains a brief summary of the remaining chapters. The chapters describe separate investigations with experiments. They are written much like stand-alone journal articles: each with their own specific introduction, material and methods, results, and conclusions.

Chapters 2 and 3 pertain to investigations on the shear field induced collagen orientation mechanism. They present two different modalities for the detection of flow channels created through the process of flow-induced PG network disentanglement. In Chapter 2, the shear flow induced orientation mechanism is presented. Then the high pressure freezing cryoimmobilization technique is applied to normal cartilage to determine unloaded PG network ultrastructure. Cryosection techniques are used to differentiate between PG network patterns and ice crystal segregation patterns. Two different freeze substitution techniques with conventional embedding are compared for ultrastructural detail preservation. Finally, these techniques are applied to cartilage which has been osmotically compressed and allowed to imbibe electron dense particles which would outline existing flow channels. In Chapter 3, confined consolidation compression and imbibing creep experiments are presented. These results are used with various models to determine the presence of velocity dependent permeability as evidence of flow induced PG disentanglement.

Chapters 4 and 5 pertain to investigations of the drag induced collagen orientation mechanism. In Chapter 4, the drag induced orientation mechanism is presented. Then the isolation of loose collagen fibrils in articular cartilage is discussed. In Chapter 5, models are developed for this mechanism, and they are validated and finally applied to loose collagen fibrils in cartilage with available parameter values from the literature.

The conclusions in Chapter 6 summarize the results obtained from Chapters 2 to 5 of the thesis. The significant findings of the investigations are reemphasized and interpreted in terms of the more general issues presented in Section 1.1. This chapter also provides several potential directions for future research.

CHAPTER
TWO

ELECTRON MICROSCOPY

2.1 SHEAR FLOW INDUCED ORIENTATION

Shear induced orientation of fluid suspended fibers was first analyzed by Jeffrey in 1922 [39]. He derived the equations of motion of the prolate spheroid "tumbling" through the fluid in shear, Figure 2.1, which was later specialized to a fiber by Forgacs and Mason [22]. The fiber rotation is fast when parallel to the shear gradient and slow when perpendicular to it. The aspect ratio (length to diameter) of the fiber determines the angular velocity as a function of orientation within the shear field, Figure 2.2. From this one can determine the probability of observing the fiber at any given angulation, Figure 2.3. A simple experiment can be used to demonstrate shear-induced orientation (and has been used, in this study, to confirm the theory). Some short fibers (carbon fiber) are suspended in a viscous fluid (glycerin) and placed between two glass discs. Steady rotation of one disk establishes a radial velocity gradient within the fluid and the resulting shear field tumbles the fibers as predicted by Jeffrey. Since the tumble of the fibers is very fast when they are normal to the fluid velocity vector (oriented radially with respect to the disc), and very slow when parallel (tangential to the disc), the average orientation is tangential.

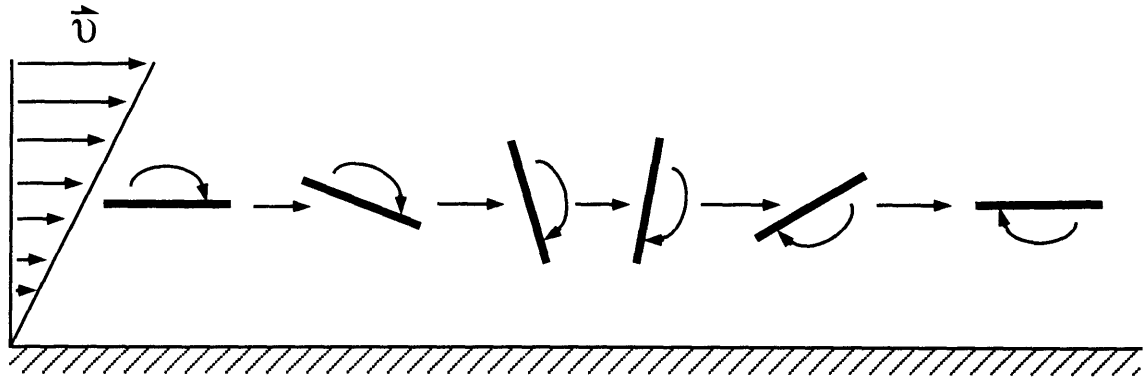

Figure 2.1 Fiber "tumbling" in a shear field.

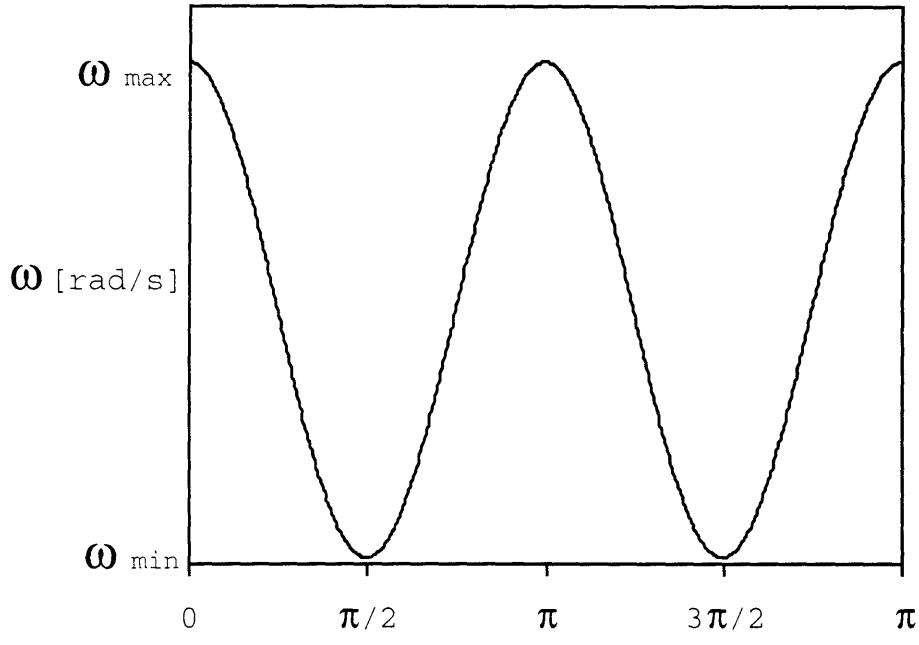

Figure 2.2 Angular velocity vs. orientation (w.r.t. shear gradient) of the fiber "tumbling" in a shear field.

The global shear field produced by the fluid flow between the opposing layers of cartilage has been modeled [95]. These were found to be of low intensity and do not correspond to observed patterns of collagen orientation in the superficial layer. If the shear field plays a role, it must be of a different scale and nature. This has led to the proposal of the existence of non-uniformities in flow fields within the tissue on the scale of the openings in the collagen network. Most of the resistance to fluid flow through cartilage is due to PGs. Flow channels

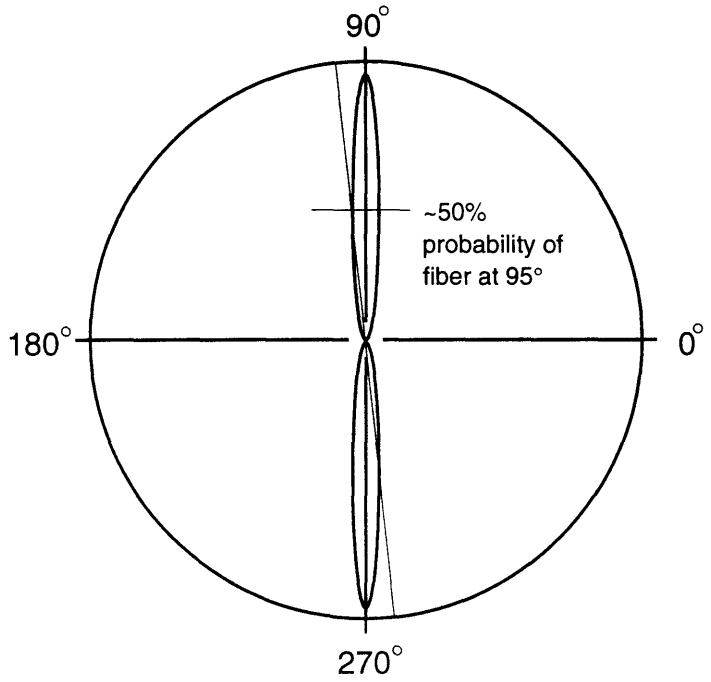

Figure 2.3 Probability of instantaneous orientation (w.r.t. shear gradient) of a fiber "tumbling" in a shear field.

do exist but the question is only on what scale: molecular, where the fluid would flow through the inter-PG-network spaces (40-90Å) [51, 58]; or on the collagen network scale with clusters of PGs disentangling to open up channels. The mechanism of PG immobilization within the collagen network is not fully understood. The work of Skerry *et al* [87] on the load induced orientation of PG clusters in bone may be an indication of such arrangements in other tissues as well. While the observed condensed clusters of PGs are probably an artifact of tissue preparation, they do indicate the discrete nature of their structural organization. If clusters of PGs are in fact separate clusters attached to the collagen network at discrete locations and only entangled at the cluster boundaries, forced fluid movement through the tissue may lead to separation (disentanglement) of individual clusters. Flow channels would open up and the velocity field would become non uniform, generating shear fields on the scale of PG clusters (and the openings in the extant collagen network), Figure 2.4.

Thus, loose collagen fibrils within the PG gel would be now oriented parallel to the flow by the mechanism described by Jeffrey. The expected orientation is along the streamlines of

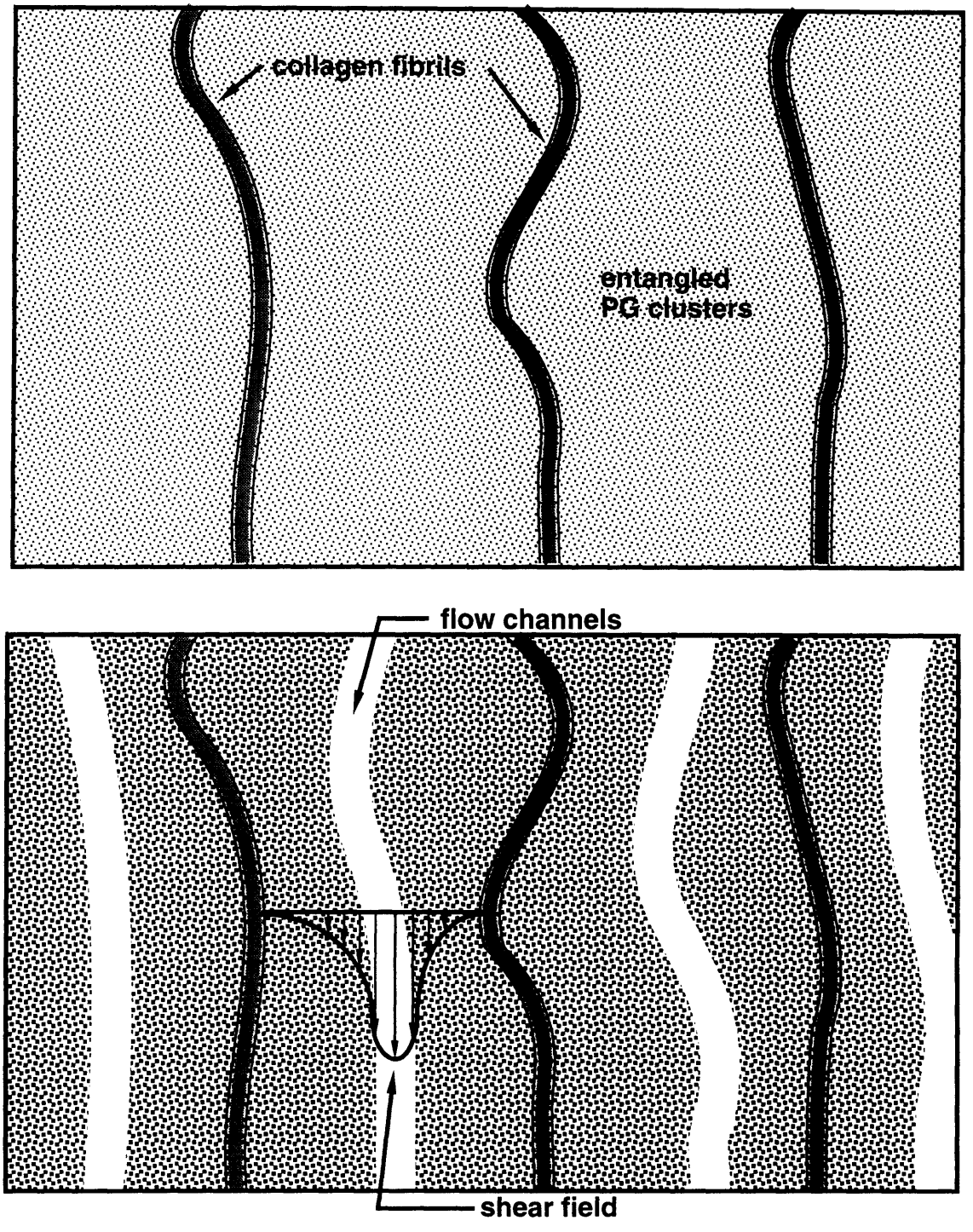

Figure 2.4 Cartoon of PG network within the collagen network (top) and their disentanglement (bottom) with consequent interstitial fluid shear field, produced by tissue loading and deformation.

fluid flow. The flows are not stationary, but with this mechanism, the integration of the orientation effects of variable flows should not present a major problem. In order for this mechanism to function, flow channels must exist in the ECM as a result of PG network disentanglement. To visualize these channels under electron microscopy, first, state of the art cryoimmobilization techniques were employed to observe PG network ultrastructure in the unloaded state. These techniques were then applied to cartilage samples in search for channels.

2.2 UNLOADED PROTEOGLYCAN NETWORK ULTRASTRUCTURE

2.2.1 INTRODUCTION

The high density of negatively charged GAGs, important for cartilage function, is the main obstacle to proper chemical fixation for examination of PG ultrastructure morphology. Early on, the PGs were extracted from the ECM by aqueous fixation media due to their high solubility in water [19, 35].This problem of PG solubilization was overcome by use of various cationic dyes (i.e. ruthenium hexaamine trichloride, [35] and others, [13, 27, 45, 83-85, 96]). These dyes immobilize PGs by precipitation from the aqueous media, but this condensation of PGs into granules destroys their molecular structure, [27]. In addition, osmium tetroxide post-fixation with the use of dyes worsens PG loss by disrupting the precipitated PGs, [37]. Finally, swelling of tissue occurs when exposed to aqueous fixation media due to the natural under-hydrated state of PGs. This distortion is amplified during dehydration and embedding processes.

In the last decade, cryofixation techniques have been developed to partially overcome the problems associated with chemical fixation. Of the many techniques available to rapidly freeze the sample ([2, 24, 31, 71]), high pressure freezing (HPF) alone is capable of immobilizing aqueous specimens of significant proportions necessary for tissue studies, [64]. With HPF, the pressure is raised to over 2100 bar, depressing the freezing point to 251°K, where crystal growth and nucleation rates are drastically reduced allowing for adequate cryoimmobilization of thick specimens, [38]. After cryoimmobilization, acetone or methanol can be freeze substituted (FS) for water. Finally, the specimen is either conventionally embedded (CE) above 273°K (e.g. Epon/Araldite) with stabilizing agents (e.g. osmium tetroxide, glutaraldehyde, uranyl ions) in the substituting organic solvent, or low temperature embedded (LTE) (e.g. Lowicryl).

Presently, cryotechniques are regarded as the best method for ultrastructural studies of cartilage ECM. However, the effects of high pressure on cryoimmobilization are not completely understood. Hunziker and Hermann used HPF + FS + embedding to study the cartilage ultrastructure [34]. They found the morphology of the chondrocyte and pericellular matrix to be similar in specimens prepared with LTE as compared to CE. They also found the immunosensitivity of the CE specimens to be 93-97% of LTE specimens. In this study, the accepted criterion of non-segregated nuclear chromatin in the chondrocyte was used as an indication of the absence of ice crystal damage throughout the tissue. In normal tissue where larger amounts of water are intracellularly located, this is an early and sensitive measure of ice crystal damage. However, in a tissue like cartilage, the ECM which contains 80% water may be a more sensitive indicator, but also the fine network structures of PGs may be impossible to differentiate from the destructive segregation patterns produced by the formation of ice crystals.

In our study, HPF specimens of cartilage from the knee articular surfaces of full term bovine fetuses were cryosectioned and electron diffraction patterns were measured to determine the presence of ice crystals. Then these same specimens were split, FS with two different solvent mixtures, and conventionally embedded. Finally, sections were viewed under TEM for examination of ice crystal effects and comparison of the PG network structure, in regions free of ice crystal (as determined by electron diffraction), for the two different FS solvents.

2.2.2 MATERIALS AND METHOD

Cartilage Tissue Preparation

Ø 6.0 mm cartilage plugs (with subchondral bone) were cored under irrigation with 0.9% PBS (with 20mM EDTA, 0.2 mM PMSF, 5 mM benzamidine-HCl, 5 mM NEM, 100 I.U./ml penicillin and streptomycin at ph 7.2, 4°C) from femoral condyles of full term bovine fetuses (several hours post-mortem). The plugs were kept in Dulbecco's modified Eagle's medium (DMEM) at 4°C after coring, during sectioning, and before HPF (2 hr). A vibratome was used to cut sections as near as possible to the articulating surface and with a uniform thickness. Finally, a punch (Grieshaber, Schaffhausen) was used to produce specimen disks suitable for high pressure freezing (Ø 2.0 x 0.2 mm and Ø 2.0 x 0.4 mm, measured by an electronic micrometer, Mitutoyo).

High Pressure Freezing

A commercial high pressure freezer (HPM 010; Bal-Tec) was used, [63]. The specimen disks were immersed in 1-hexadecene and sandwiched between two supporting aluminum platelets manufactured with depressions to fit the specimens exactly ([90] and also commercially available from Bal-Tec). 1-hexadecene optimizes the thermal and barometric transfer during high pressure freezing, [90]. It is not miscible with water and, therefore, osmotically inactive. The specimen sandwich was loaded into the holder and frozen at high pressure. Finally, one of the platelets with the specimen was stored in liquid nitrogen until further processing.

Cryosectioning and Electron Diffraction

Cryosections were cut as described in [61] on a Reichert Ultracut S microtome equipped with an FCS cryo-attachment. 45° diamond knives (Diatome AG) with a clearance angle of 6°, and an ionization device (Static Line, Diatome AG) with a primary voltage of 7-8 kV. Imaging and electron diffraction (camera length of 40 cm) of the cryosection was conducted on a Zeiss EM 902, [62].

Freeze Substitution and Embedding

The same specimen used for cryosections were freeze substituted as described by [71] in a Bal-Tec FSU 010. Frozen tissue water was substituted by two organic solvents in four stages; 8 hr at 183°K, 6hrs at 213°K, 8 hr at 243°K, and 1hr at 273°K. The organic solvents used were either absolute acetone with 2% OsO_4 or methanol containing 2% OsO_4 , 0.5% uranyl acetate, 3% glutaraldehyde, and 3% water. All specimens were washed with anhydrous solvent prior to infiltration with resin. Specimens were then embedded in Araldite/Epon in four stages; 30% resin for 6 hr, 70% for 14 hr (both at 277°K), 100% for 6 hr at 293°K, and polymerized at 333°K for 14 hr.

Tissue Sectioning and Staining

Sections of 50-60 nm thickness were cut from the blocks on a Reichert ultramicrotome Ultracut E with a diamond knife. After mounting on 100 or 200 mesh carbon coated colodion film copper grids, the sections were stained with saturated aqueous solutions of uranyl acetate and lead citrate, [79], for 7 min each with aqueous washings in-between. Electron microscopic examination was conducted on a Hitachi 600 TEM.

2.2.3 RESULTS

A typical articular chondrocyte, freeze substituted by acetone solvent, is presented in Figure 2.5. The intracellular organelles are well preserved with an intact nuclear membrane exhibiting nuclear pores. The chondrocytic plasmalemma is maintained intact and in almost complete apposition with the pericellular matrix. The non-segregated heterochromatin and euchromatin in the nuclei indicates adequate cryoimmobilization, and the absence of a "lacuna" indicates minimal loss of PGs, [35, 37].

However, the traditional criterion for freezing without ice crystal formation may not be adequately sensitive for articular cartilage. Figure 2.6 shows the plasmalemma-pericellular matrix interface for two regions within the same specimen. Figure 2.6.A is from the chondrocyte shown in Figure 2.5. and is located near the center of the specimen. Figure 2.6.B is from another similar chondrocyte located near the specimen surface. In both micrographs, the plasmalemma-pericellular interface is intact showing numerous contact sites. However, the PG network structure is much more coarse in the mid-specimen area. Figure 2.7 is representative of the interterritorial matrix, again comparing the mid-specimen to surface regions (2.7.A vs. 2.7.B). In contrast to the pericellular matrix, collagen fibrils are apparent. Cross-banding patterns of the fibrils in the plane of the section are rare, but can be discerned with clarity when present. Both micrographs further exhibit the difference in the PG network separation. This coarser network structure may be segregation patterns produced by ice crystals, although no segregation patterns are evident in the chondrocyte nucleus (see discussion).

Cryosections and electron diffraction patterns of other HPF specimens were then used to determine the true state of solid ECM interstitial water and to detect the difference between mid-specimen and surface regions. Figure 2.8 is a plate of cryosection electron micrographs with corresponding electron diffraction patterns of the ECM from these two regions, respectively. In both, many collagen fibrils are evident. The chondrocyte in the mid-specimen region is nicely preserved with intact membranes and organelles (Figure 2.8.A). However, the diffraction pattern from the mid-specimen has a hexagonal diffraction pattern indicative of ice crystals (Figure 2.8.B), whereas that from the surface region (Figure 2.8.C) shows diffuse rings indicative of vitrified solid water (in an amorphous state, Figure 2.8.D), [17]. Vitrified regions, determined by diffraction patterns, were limited to within 15-25 μm of the specimen surface (for all 0.2 and 0.4 mm thick specimens).

Figure 2.5 Electron micrograph of an articular cartilage chondrocyte (mid-specimen) and its surrounding ECM after HPF+FS(acetone)+CE. Intracellular organelles (e.g. rough endoplasmic reticulum (**RER**)) are well preserved. The nuclear membrane is intact with nuclear pores (**NP**) and distinct heterochromatin (**H**) and euchromatin (**EU**). The plasmalemma (**PL**) is also intact and in almost complete apposition with the surrounding ECM. Bar = 1 μm x 10,000.

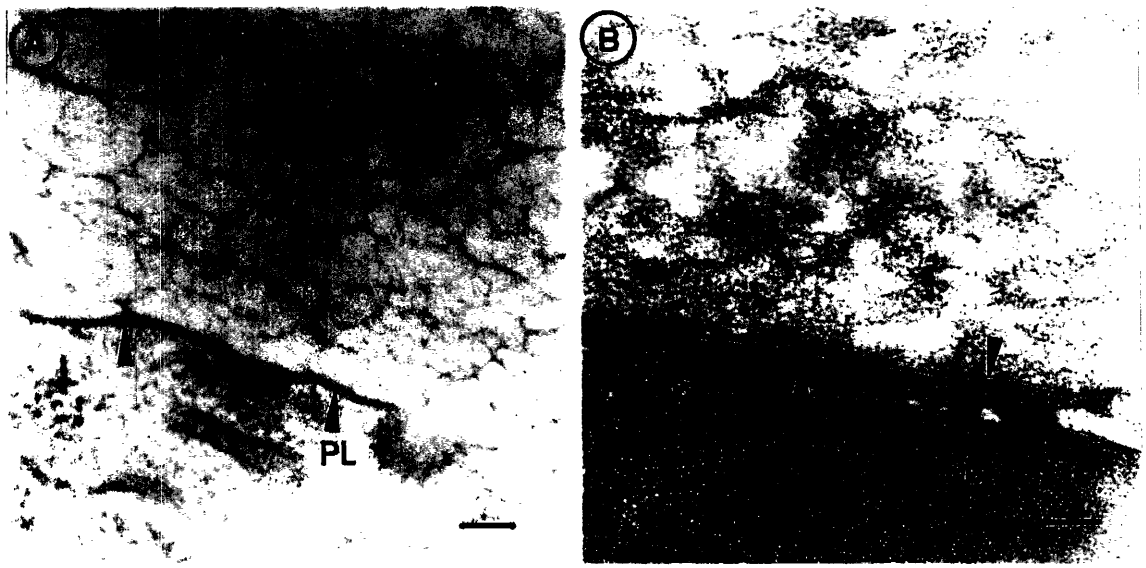

Figure 2.6 Electron micrographs of the plasmalemma (**PL**)-pericellular matrix (**PCM**) interface after HPF+FS(acetone)+CE. (A) is from the chondrocyte shown in Fig 1. (mid-specimen), and (B) is from a similar chondrocyte near the surface of the specimen. The **PL-PCM** interface is intact with some contact sites (arrows) in both micrographs. The PG network structure is coarser in the mid-specimen region. Bar = 0.1 μm x 73,000.

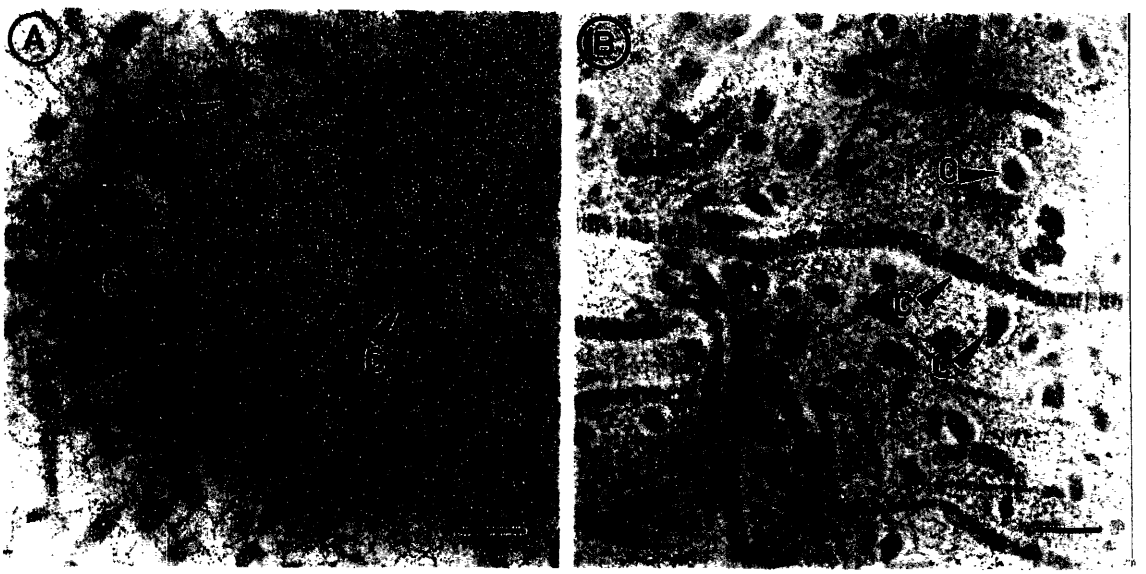

Figure 2.7 Electron micrographs of the interterritorial ECM corresponding to the regions shown in Figure 2.6, (A) mid-specimen and (B) surface region. Cross-banded collagen fibrils (**C**) are evident mostly in oblique cross section and occasionally in-plane. The coarser PG network structure in the mid-specimen region (A) may be segregation patterns due to ice crystal formation. Bar = 1 μm x 85,000.

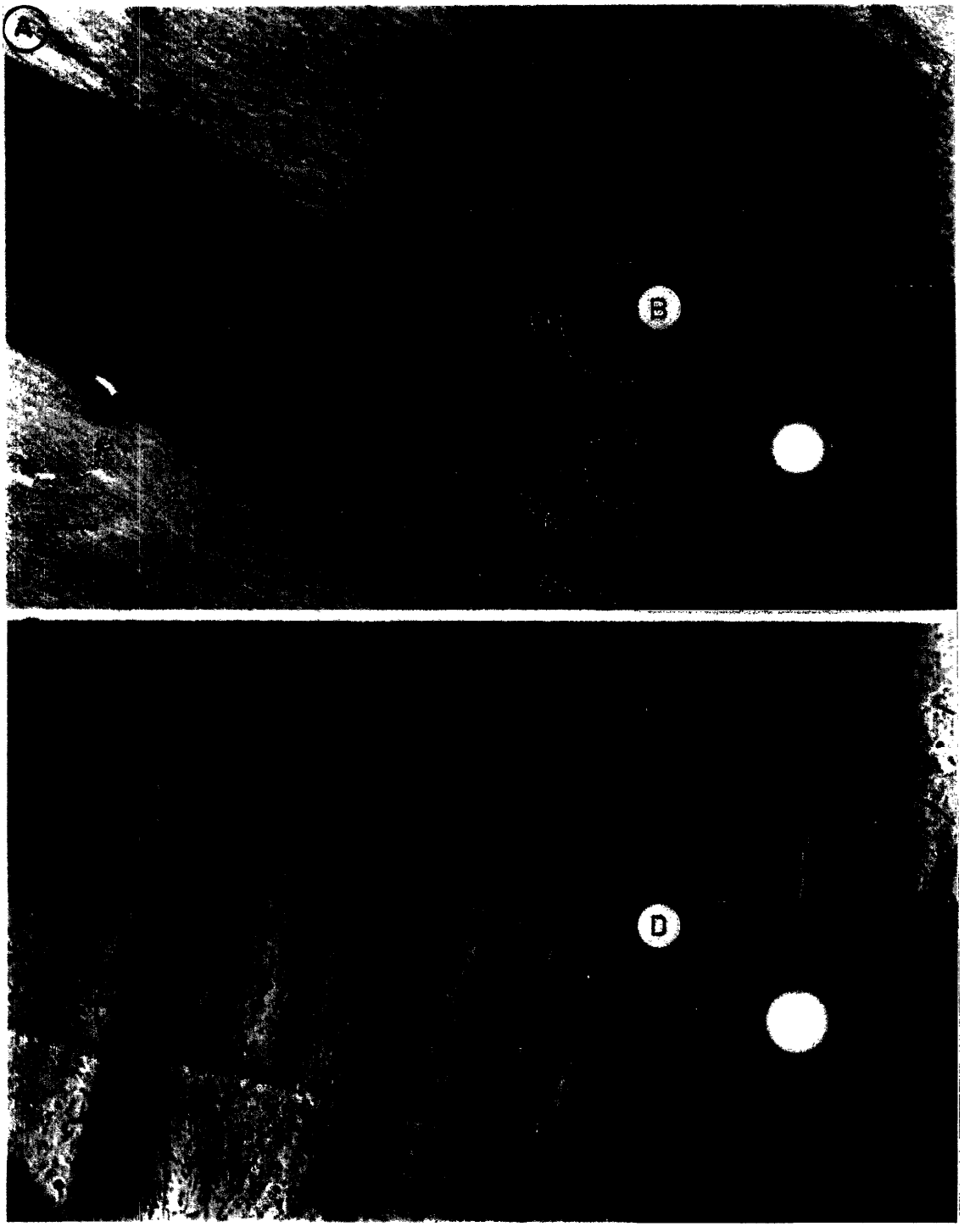

Figure 2.8 Electron micrographs of cryosectioned articular cartilage tissue after HPF (A) from the mid-specimen and (C) surface regions with corresponding electron diffraction pattern of the ECM, (B) and (D) respectively. Chondrocyte (**CH**) is well preserved and numerous collagen fibrils (**C**) are evident in the ECM (a and c). The sharp light spots on the diffraction pattern indicates the presence of ice crystals (B) whereas the diffuse rings and a lack of sharp dark spots on the diffraction pattern indicates the absence of ice crystals (D). Bar = 0.6 μm x 18,000 in (A) and 0.3 μm x 25,500 in (C).

Keita Ito, Sc.D.

The same specimens used for cryosections were divided in half and processed similarly, but in two different FS solvent mixtures. Only those regions determined by electron diffraction to contain vitrified solid water were examined by TEM. Figure 2.9 displays chondrocytes and their surrounding ECM from a specimen FS with methanol (Figure 2.9.A) or acetone (Figure 2.9.B). The nuclear structure is similar, with good distinction of the peripheral heterochromatin and more central euchromatin in both. The organelles are more distinctive and the plasmalemma is better preserved in the latter. In addition, the plasmalemma-matrix interface is more intact in the latter. Although contrast of collagen fibrils in the ECM is better in the methanol FS specimen half, fibrils are evident in both. Also the higher ratio of PG/collagen fibrils in the pericellular matrix over that in the interterritorial matrix is more evident in the methanol FS specimen half.

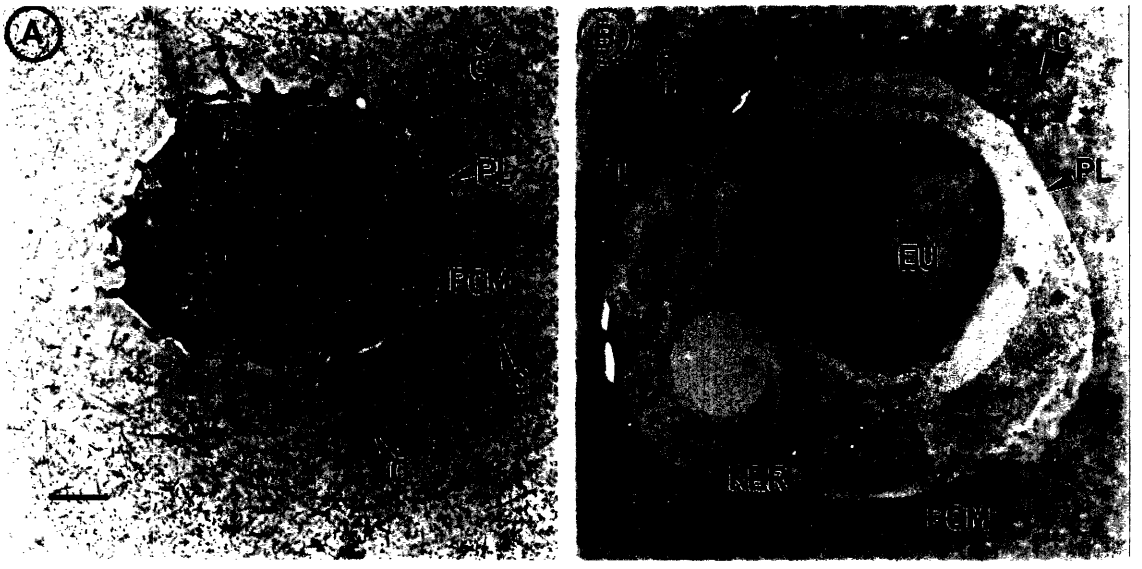

Figure 2.9 Electron micrographs of articular cartilage tissue after HPF+FS+CE, from well vitrified regions verified by electron diffraction. (A) is a specimen prepared by FS with a methanol solvent mixture, whereas (B) was prepared by FS with an acetone solvent mixture. The nuclear structures are similar with distinct euchromatin (**E U**) and heterochromatin (**H**). Organelles (e.g. rough endoplasmic reticulum (**RER**)) are more distinctive and the plasmalemma (**PL**)- pericellular matrix (**PCM**) interface is more intact in the acetone FS specimen (B). Collagen fibrils (**C**) and the higher ratio of PG/collagen fibrils in the pericellular matrix is more evident in the methanol FS specimens. Bar = 1 μm x 7,700.

Figure 2.10 displays at higher magnification, the interterritorial ECM near those chondrocytes shown in Figure 2.9. The contrast from the methanol FS specimen half is sharper and exhibits clearly the banding pattern of the in-plane collagen fibrils (Figure 2.10.A). However, the most distinctive difference in these two preparations is the preservation of the PG network structure. The PG network is finer and the detail of the substances between the more electron dense fibrous structures is preserved in the acetone FS specimen half (Figure 2.10.B). It may appear that this finer more detailed PG network is simply a loss of contrast in the micrograph. However, an even higher magnification of the PG rich pericellular region shows the detailed preservation of the PG network (Figure 2.11).

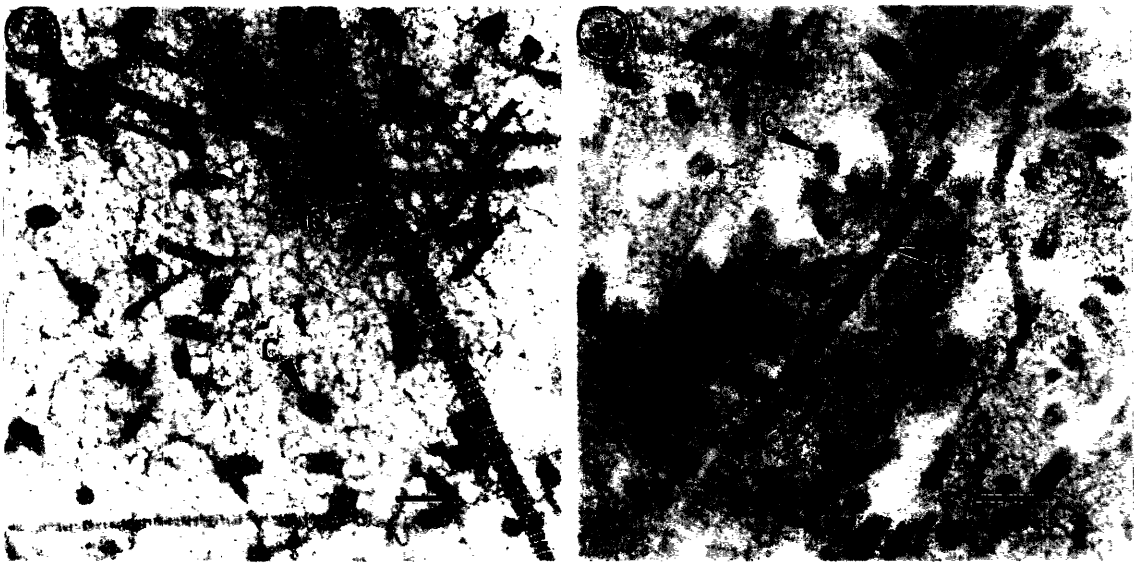

Figure 2.10 Electron micrograph of the interterritorial ECM near chondrocytes shown in Figure 2.9, (A) and (B) correspondingly. Contrast is greater in the methanol FS specimen (A) with clear cross-banding of the in-plane collagen fibril (**C**). The PG network is finer and more detailed in the acetone FS specimen (B). Bar = 0.1 μm x 85,000.

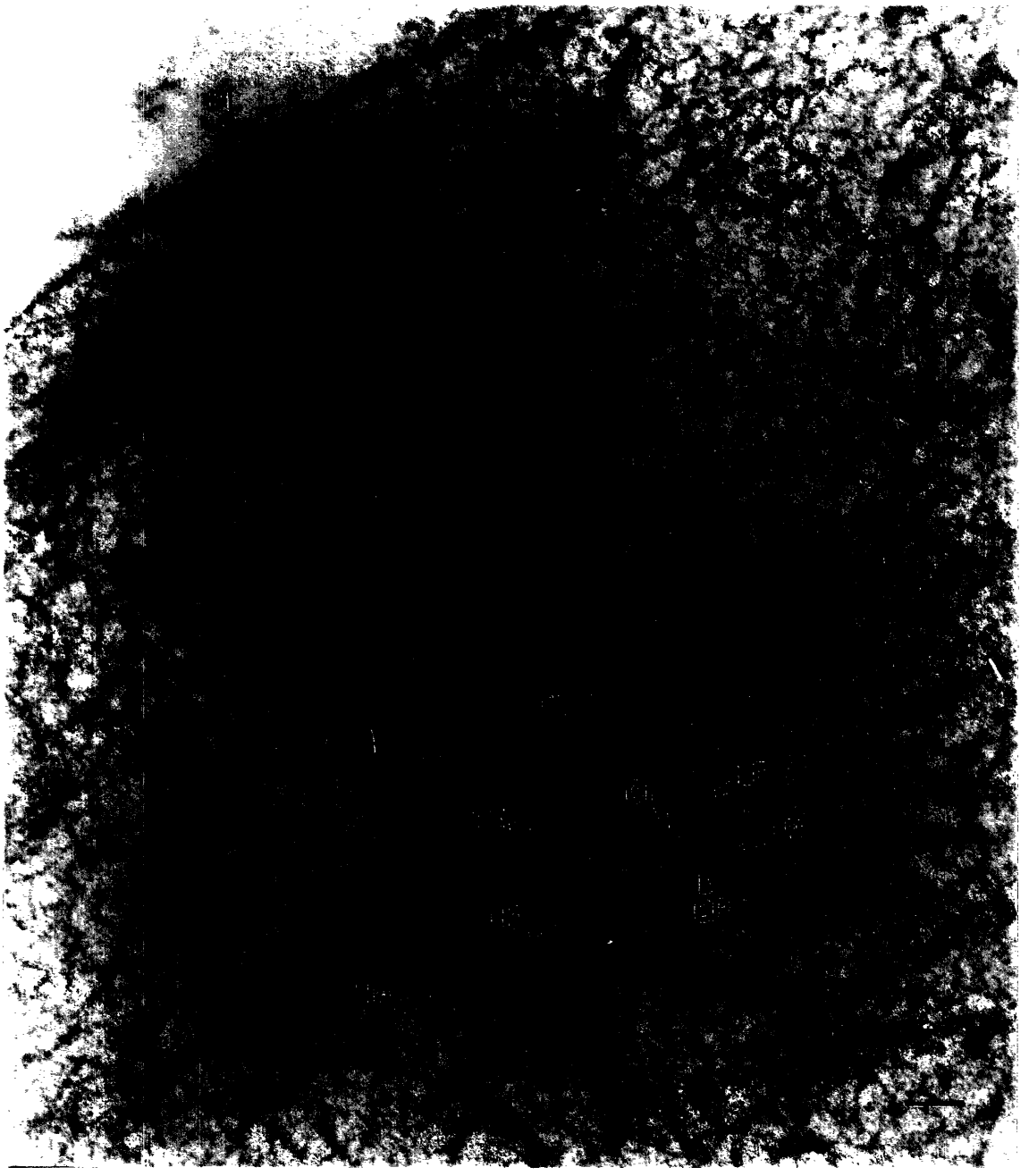

Figure 2.11 High magnification electron micrograph of the plasmalemma and pericellular ECM from the chondrocyte shown in Figure 2.10.b. There are a diversity of fibrous structures quite similar to those seen in isolated PG aggregates prepared with Kleinschmidt technique (i.e. hyaluron backbone (**HA**), core protein (**CP**), link protein region (**LP**), and chondroitin sulfate chains). Bar = 0.04 μm x 250,000.

2.2.4 DISCUSSION

With chemical fixation techniques, the accepted criteria for good preservation of cartilage tissue morphology to determine loss of PGs from the ECM has been based on the structure of the chondrocyte. Since the ECM pericellular compartment is rich in PGs, it is highly sensitive to suboptimal preparation conditions which could cause the loss of PGs, [34]. Furthermore, since the plasma membrane has been found to form a continuous surface with this surrounding pericellular matrix, [2], structural abnormalities at this interface may indicate loss of PGs. In fact, PG matrix loss of only 2-4% is sufficient to cause destruction of the cell-matrix interface producing shrinkage and/or collapse of the chondrocyte with formation of a "lacuna," [35, 37]. Thus, the chondrocyte/pericellular interface is often used to determine adequate fixation of the tissue with minimal PG loss.

Cryotechniques however, are also not free from artifacts. High pressure freezing is not yet completely understood and suboptimal cryoimmobilization can still occur. Among these artifacts, ice crystal formation results in segregation patterns which destroy fine structural details. Hence, with the advent of cryotechniques, the accepted indicators for optimal cryoimmobilization and fixation have been 1) no PG loss as seen by integral plasmalemma-matrix interface with no cell shrinkage and detachments from the matrix causing formation of "lacunae," and 2) the presence of non-segregated chromatin as an indicator of adequate freezing of interstitial water. However, in cartilage where the more water is located in the ECM (80%) than in the chondrocyte nucleus, non-segregation of the nucleus may not be indicative of the state of solid water in the ECM.

By traditional standards, HPF + FS + CE can produce well preserved specimens (Figure 2.5). The organelle and membrane structures of the chondrocyte are intact. The plasmalemma/pericellular matrix is nearly in full apposition with almost no "lacunae" formation indicative of minimal PG loss. Also there is no segregation of nuclear chromatin. These results are consistent with the previous work of [36]. By inspection of the chondrocyte, this specimen appears well preserved with no segregation patterns, and in the ECM, the PG network cannot be differentiated from any ice crystal segregation patterns. However, comparison of mid-specimen (Figures 2.5, 2.6A and 2.7A) to surface regions (Figures 2.6B and 2.7B) within the same specimen, reveals the presence of a coarser PG network in the former. These regions were then examined by electron diffraction of frozen-hydrated cryo-sections and ice crystals were found in those regions with these coarser PG networks (Figures 2.8AB vs. 2.8CD). Thus, in order to insure adequate cryoimmobilization of cartilage with

vitrified solid water free from ice crystal segregation artifacts, it is necessary to not only inspect the chondrocyte, but also to inspect the ECM for crystalline segregation patterns and use diffraction methods to detect crystalline solid water.

In addition to interstitial water crystallinity determination, frozen-hydrated cryosections were used to directly visualize the specimen without freeze substitution and embedding (Figures 2.8A and 2.8C). At present, this represents the most direct approach for imaging of cryoimmobilized biological specimens. Unfortunately, present technology does not allow for sufficient examination of cartilage ECM ultrastructure and the specimen must be further processed for TEM (Figure 2.8C). Also, in the process of comparing various regions in the same specimen, it was found that regions of mostly vitrified water existed only within 15-25 μm of the surface in 0.2 and 0.4 mm thick specimens. This inadequate cryoimmobilization throughout the specimen may have been caused by insufficient thermal transfer resulting from the large mass of the tissue, and exhibited by mid-specimen ice crystals. This is also consistent with the fact that 0.4 mm thick specimens had thinner regions of vitrified water at the specimen surface than the 0.2 mm thick specimens.

In comparisons of vitrified water regions (as determined by electron diffraction), FS with an acetone solvent mixture was found to preserve chondrocyte detailed structures better than FS with a methanol solvent mixture (Figure 2.9). The methanol FS specimens show a coarser patterns with little substance in-between electron dense fibrous structures, whereas acetone FS appears to exhibit finer structural complexity of the ECM PG network (Figure 2.10). Since these regions are adequately vitrified, the coarser pattern in methanol treated specimens are probably not due to segregation patterns. Although both solvents substitute for water quickly, methanol has been found to substitute faster and to be more aggressive due to it's higher polarity at lower temperatures, [33]. This more aggressive substitution of water by methanol may have resulted in the coarser PG network, [18].

Finally, investigators have seen a diversity of fibrous structures in the PG network. They have speculated that the finer thread-like structures are chondroitin sulfate side chains, the thicker are PG core proteins, and that the coarsest are hyaluron-binding region/link proteins of PG aggregates, [20, 38]. These various structures are also evident, and are identified in the highly magnified electron micrographs of the acetone FS specimen (Figure 2.11). Although more sensitive techniques (e.g. immunostaining) are required to identify these PG aggregate components, the labeled components are similar to isolated PG aggregates prepared with the Kleinschmidt technique, [80]

2.3 EM OF CHANNEL FORMATION

2.3.1 INTRODUCTION

As discussed previously, the hydrophilicity of the entangled PGs, entrapped within the collagen network, makes cartilage a poroelastic material swollen with water. Based on equality of partition coefficients for tritiated water to that of the total water content of the tissue [48, 55, 56], most of the 65-75% w/w aqueous interstitial fluid in cartilage (whether extra- or intrafibrillar) is freely exchangeable. Therefore most of the fluid within the ECM is free to move through the organic solid matrix.

This ability of the fluid to flow through the matrix has been quantified by measurement of tissue permeability, a bulk measure of the flow resistance, [47, 53, 58]. In all of these investigations, fluid is forced to move by application of a pressure difference across a cylindrical disc of cartilage. The apparent permeability of cartilage is then calculated by Darcy's Law, for one dimensional flow, applied to the measured flow rate at equilibrium. McCutchen, [58] and later Maroudas, [51] used these permeabilities with the Poiseuille formula for steady-flow through a circular cylinder, to calculate average pore sizes of 40-90 Å through the cartilage specimen. These pore sizes were then used to interpret results large molecule diffusion into the ECM, [50, 88]. Maroudas *et al* observed that larger particles are able to penetrate through the ECM [50]. They measured the partition coefficients of various size solutes in the interstitial fluid at equilibrium, and found that partition coefficients of larger molecules allowed to diffuse into cartilage plugs are on the same order of magnitude as much smaller particles like serum albumin (Stokes radius ≅ 35Å), which was shown to have a relatively high diffusion coefficient [88]. These results were felt to suggest the existence of a small fraction of "pores" larger than those calculated from permeability measurements and much larger than these penetrating particles.

However, the circular cylindrical pore assumption does not represent the true geometry of fluid flow in the ECM, and the actual value of the pore size has no physical representation. More recently, the ECM has been viewed as a sieve-like fiber meshwork, with the interstitial fluid flowing through fibers with an average interfiber spacing. Although the interfiber spacing, calculated from the measured permeabilities, would be of approximately one order of magnitude smaller than the cylindrical pores, and smaller than these particles observed to diffuse into the ECM, their diffusion through the network does agree with transport properties through entangled meshworks observed by Laurent *et al* [42]. The hypothesis that

these entangled networks are able to relax are consistent with observations that although the equilibrium penetration of large particles are equal to that of smaller particles, their rates of penetration are much slower [88].

However, with induced interstitial fluid flow, as is the case under physiological loading, transport rates of larger particles were found to be more enhanced than smaller particles. Tomlinson and O'Hara, using techniques similar to Maroudas *et al,* found that the absorption and desorption rates of serum albumin increased by twice to tenfold under physiological cyclical loads, whereas the contribution of fluid flow to overall transport of smaller particles were negligible [74, 98]. They concluded that this increase might be due to the relaxation of the PG network under fluid flow, causing formation of larger interfiber openings in the PG network.

These larger openings may constitute channels which would give rise to interstitial fluid flow shear fields within the ECM. Two different methods were developed to observe these channels. The first method was to HPF the cartilage specimen during compression to directly observe the channels, and the second method was to HPF cartilage specimens which had been allowed to imbibe a colloidal suspension of electron dense particles following compression, blocking open the channels. In both methods, the specimens were prepared according to FS and CE techniques described earlier in Section 2.2, after which open channels and or particle filled channels were searched for by TEM.

2.3.1 MATERIAL AND METHODS

High Pressure Freezing during Compression

Ø2.0 mm x ≈440 μm cartilage specimens were prepared as described in Section 2.2.2. These specimen disks were immersed in 1-hexadecene and sandwiched between two supporting aluminum platelets manufactured with 200 μm depressions in each platelet. These specimen-platelet sandwiches were loaded into a modified holder, containing a Bellevile washer for compression (Figure 2.12), and frozen with a Bal-Tec HPM 010 high pressure freezer. After removal of one platelet, the specimens were stored in liquid nitrogen until further processing.

The Bellevile washers were manufactured by pressing laser cut 1.5 mm I.D. x 3.0 mm O.D. x 80 ± 2 μm thick hardened spring steel washers with a 140° cone to produce a 115 μm deflection. These washers produce a maximum force of 0.35 N at 75 - 100% compression. Assuming an equilibrium modulus of 1 MPa, the cartilage specimens were expected to creep

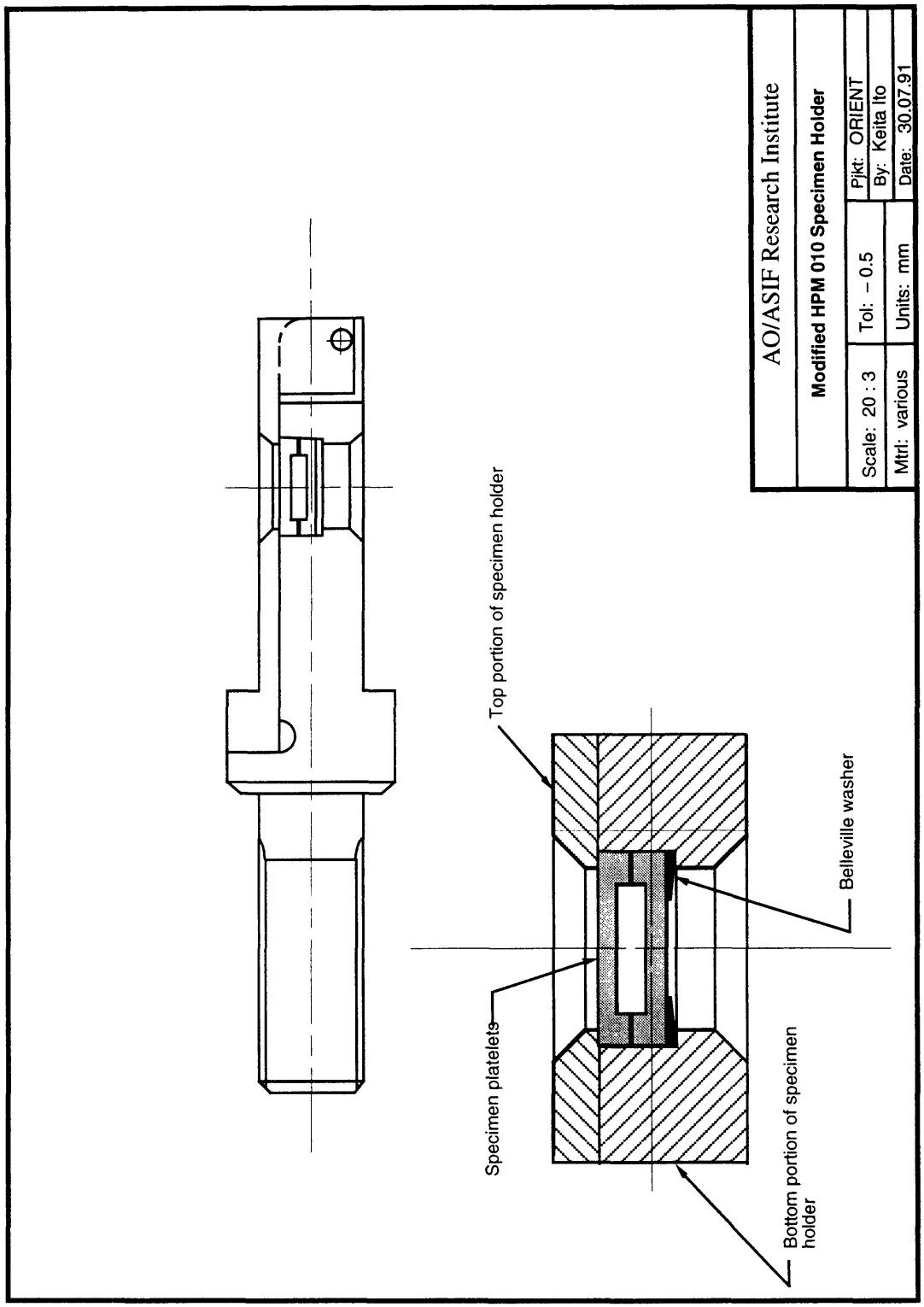

Figure 2.12 Compression apparatus for high pressure freezing

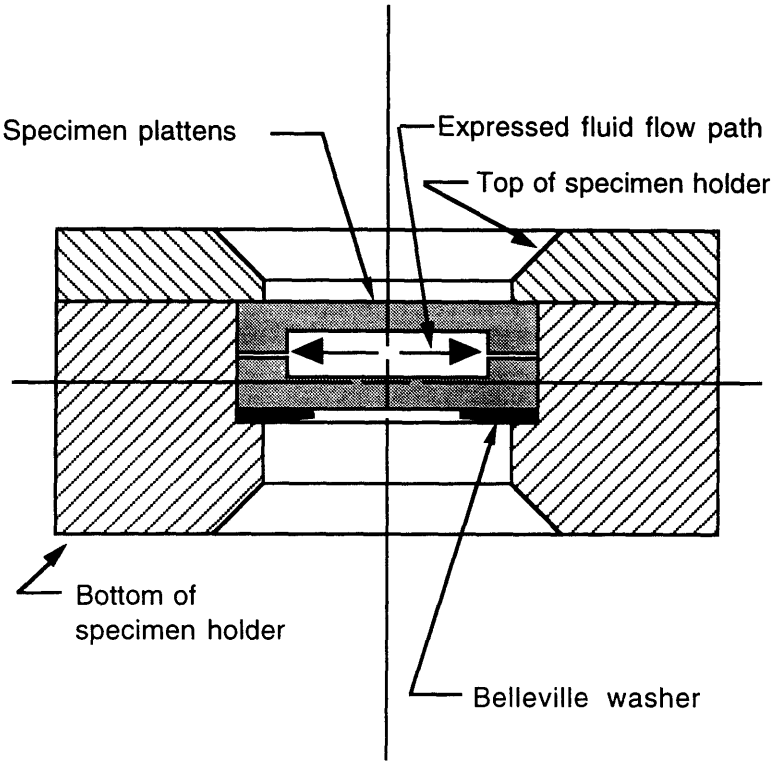

Figure 2.13 Expressed fluid flow from the cartilage specimen-platelet sandwich during compression in the high pressure freezing holder.

≈40 μm over ≈30 min. in the closed holder, and the expressed fluid was expected to flow radially out of the specimen-platelet sandwich (Figure 2.13).

Imbibing of Large Electron Dense Particles

Ø10.0 mm cartilage plugs were cored from the intertrochlear femoral surface of full term bovine fetuses (several hours post-mortem), as described in Section 2.2.2, and stored in 0.9% PBS (with 20 mM EDTA, 0.2 mM PMSF, 5 mM benzamidine-HCl, 5 mM NEM, 100 I.U./ml penicillin and streptomycin at ph 7.2, 4°C) during sectioning (30 min.). The plugs were confined in a plexiglass holder, and surfaces perpendicular to the plug axis were cut with a razor blade (Figure 2.14). Motion of the plug within the holder was controlled by a micrometer to produce 2 mm uniform thick plugs as close to the articular surface as possible (without lamina splendans).

The plugs were then osmotically compressed by techniques similar to Maroudas *et al* [52]. A polyethylene glycol solution was prepared by dissolving 250 g of 20,000 MW PEG in 1 *l* of

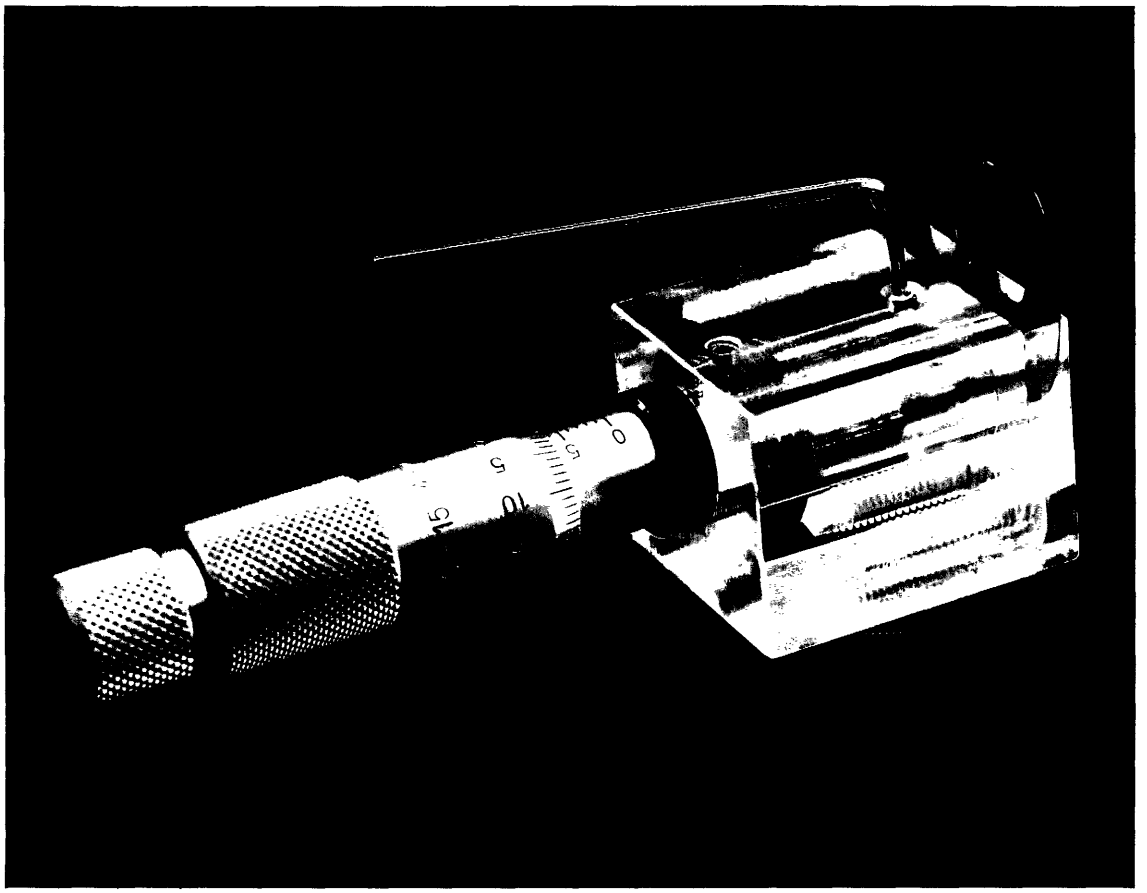

Figure 2.14 Confined plexiglass holder with micrometer positioner for cutting known thickness cartilage sections from Ø10.0 mm cored plugs.

0.15 M NaCl. This solution has an osmotic pressure of 0.6 MPa [52]. The plugs were placed between 12,000-14,000 MW Spectrapore 2 dialysis tubing filled with this PEG solution, and left in a humidified closed chamber for 2 hr at 4°C. After 1 hr the plugs were measured with a Mitutoyo electronic micrometer and found to be 35% compressed.

Two colloidal solutions were prepared containing Ø11 nm bovine serum albumin (BSA) coated gold particles and Ø12 nm ferritin particles. The BSA-Au particles were obtained from BioCell Research Laboratories as 1.7 x 10^{13} particles/ml in 1% Tris / BSA buffer solution. The ferritin solution was obtained from Sigma Chemical Co. as 100 mg/ml type I horse spleen ferritin in 0.15 M NaCl. Both solutions were dialyzed in 6,000-8,000 MW Spectrapore 1 tubing against 0.9% PBS (ph 7.2) for 1 hr x 3 while shaking at room temp.

After osmotic compression, the plugs were placed in a glass confined consolidation column and covered with 0.5 ml of either BSA-Au or ferritin containing colloidal solutions. These plugs were left overnight at 4°C and then prepared for HPF as described in Section 2.2.2. HPF specimens were cut from 200 μm sections including the surface exposed to the colloidal solutions. The specimens from both types of particle imbibing were freeze substituted with an acetone mixture, conventionally embedded in Epon/Araldite, and examined with TEM as described in Section 2.2.2.

2.3.2 RESULTS

Although several geometries were used, sustained compression creep was not possible within the confines of the high pressure freezing apparatus holder. Typically, the 440 μm thick plugs compressed 5 μm over the first 30 sec, as measured by an electronic micrometer, then remained at this thickness for up to 60 min. with sometimes 2-3 μm more compression. Hence, no specimens were frozen during compression due to technical difficulties.

From HPF studies discussed in Section 2.2.4, the regions most likely not to contain ice crystal segregation pattern damage correspond to the regions closest to the surface and exposed to the colloidal solution of particles. These regions were found on the TEM grids and examined for dispersed and collected particle formation. In both BSA-Au and ferritin particle imbibed specimens, no particles were found in either dispersed or collected states. A typical section is shown in Figure 2.15. The specimen surface is evident in the lower left corner and clear cross-banding of the in-plane collagen fiber is observable. The fine PG network shows no evidence of ice crystal segregation patterns and is similar to those micrographs in Section 2.2.3.

2.3.5 DISCUSSION

It was unfortunate that cartilage specimens could not be HPF during compression. Individual specimen disks were sandwiched between the aluminum platelets and loaded with a weight equivalent to the force generated by the Bellevile washers. This produced a compression creep curve with a final displacement of 35 ± 4.5 μm over 60 min. However when placed in the high pressure freezing holder no creep occurred. It was thought that possibly the gap between the platelets was limiting the flow of expressed fluid and platelets with grooves along this surface were tested. These grooved platelets worked only slightly better and it was not determined whether this slight improvement was due to increased flow of fluid between

the platelets or whether the cartilage deformed to fill the grooves. Nevertheless, it was discovered that the gap between the platelet and the holder was only 10 μm, and that this gap was reduced even further when the holder was closed. It was concluded that the holder geometry did not allow for flow of the expressed fluid. Furthermore in retrospect, the HPF investigation discussed in section 2.2.4 would have produced the greatest fluid velocity , and thus the channels, in the middle of the cartilage specimen where ice crystal segregation patterns were later found to be unavoidable for Ø2.0 x 0.4 mm cartilage specimens, used in this study.

Unlike the HPF during compression studies, the expected location of channel formation with the particle imbibing study corresponds to the regions most likely not to contain ice crystal segregation pattern damage, at the surface of the plug. Unfortunately these regions showed no evidence of channel formation. Also unexpected was the absence of dispersed particles within the ECM. From the diffusion experiments of Maroudas with large solute particles [50], it was expected that few dispersed particles would be evident in the ECM. It was noted that this exclusion was possibly due to negative charges on the particles. Pure gold particles are normally suspended in a colloidal solution because of electrostatic repulsion from their negative charges. However, since these charges would also inhibit imbibing of the particles into the high negatively charged ECM, they were coated in BSA, making them practically neutral [12]. Also for this reason, neutrally charged ferritin particles of similar size were used [86]. Ideally a control with smaller Au particles showing dispersed transport into the ECM was desired, but these smaller particles are difficult to observe under TEM and not likely to be completely coated with BSA [12].

Finally, although no evidence for channel formation was observed, the observations of Maroudas' group on the transport of large solute particles through the ECM persists and gives rise to speculation that larger pores than are calculated from transport studies are possible [50, 51, 74, 98]. The one major difference between our experiments and the experiments of Maroudas is the manner of loading the cartilage specimens. Our specimens were loaded through a single cycle of loading and unloading whereas Maroudas used cyclical loading over many cycle. Perhaps the formation of channels or larger pores only occurs under prolonged cyclical loading as seen under physiological conditions.

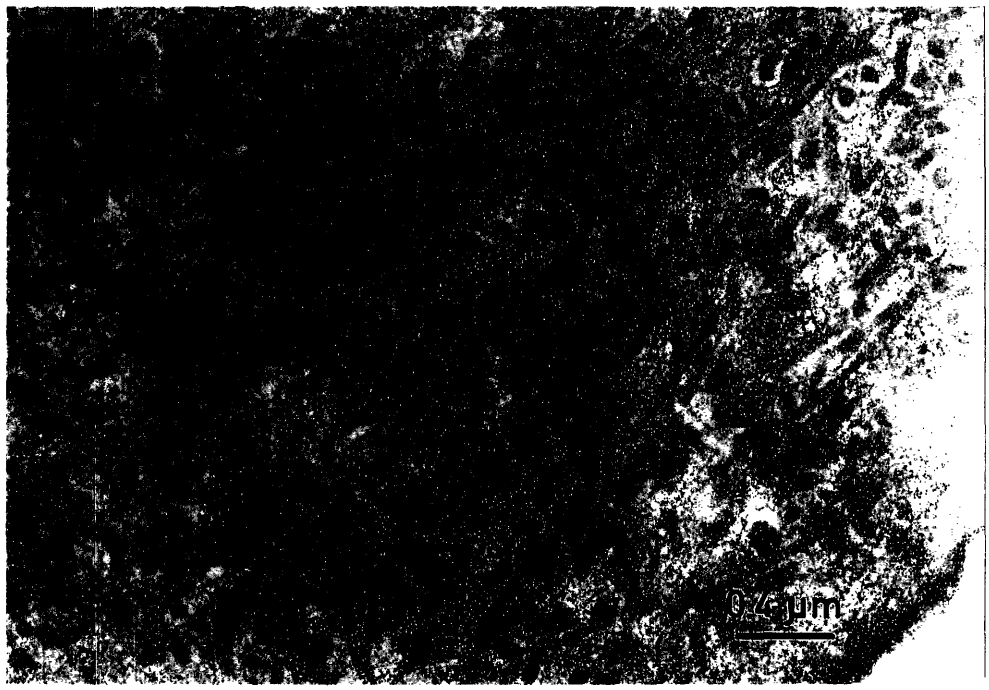

Figure 2.15 Typical electron micrograph of the specimen surface and interterritorial ECM from a cartilage plug allowed to imbibe BSA-Au particles (ferretin gives similar results). Clear cross-banding of the in-plane collagen fibril (**C**) is evident and the fine PG network shows no evidence of ice crystal segregation patterns. No flow channels are evident as a collection of particles nor are there any dispersed particles within the ECM. Bar = 0.4 μm x 33,000.

2.4 CONCLUSIONS

High pressure freezing, freeze substitution, and conventional embedding were used to prepare articular cartilage tissue for the study of unloaded PG network structure in the ECM. The absence of visible ice crystal induced segregation patterns as the traditional criterion of adequate freezing was compared to direct electron diffraction measurements of ice crystal formation in cryosections from the same high pressure frozen specimens. Ice crystals were found by electron diffraction in regions exhibiting adequate freezing by the above traditional standard. The ECM was found to be an even more sensitive indicator of ice crystal presence than the chondrocytic nuclear chromatin.

Specimens shown to exhibit regions of vitrified cryoimmobilization by electron diffraction patterns on cryosections were split then FS by acetone or methanol solvent mixtures. Both preparations showed well preserved chondrocytes and ECM with fine structures. However, specimens FS with acetone were found to exhibit finer PG network details. Although no immunostaining was conducted to identify PG aggregate subunits, distinctive structures similar to isolated PG aggregates (Kleinschmidt technique, [80]) were evident.

Specimens osmotically compressed a single cycle and allowed to freely imbibe colloidal solutions of Ø11 nm BSA-Au or Ø12 nm ferritin showed no evidence of channel or larger pore formations under examination by TEM after HPF+FS+CE. However, since these cartilage specimens were only exposed to one cycle of loading, channel or large pore formation may still occur under prolonged cyclical loading as experienced during physiological activities.

CHAPTER
THREE

PERMEABILITY

3.1 INTRODUCTION

In addition to the search for flow channels by electron microscopy, transient changes in permeability during creep were expected as a consequence of possible flow channel formations in the cartilage ECM. Since most of the water in cartilage is exchangeable [48, 55, 56], flow of interstitial fluid is created when cartilage is loaded. The resistance to this interstitial flow has been quantified by measurements of tissue permeability, a bulk measure of the flow resistance, [41, 47, 53, 58, 68]. In these earlier investigations, the resistance to fluid flow was measured with the application of a pressure difference across a cylindrical disc of cartilage. Then, Darcy's Law, for one dimensional flow, was applied to the measured steady flow rate to calculate the permeability of cartilage. Although these measurements provided a general measure of the apparent permeability, their utility was limited. Since the solid matrix of cartilage is a compliant network, the permeability of the tissue decreases with compressive strain. When a pressure differential is applied across the cartilage disk, the compressive strain increases and the permeability decreases with increasing pressure differential . With an equilibrium modulus of 0.7 - 1 MPa [46, 67] and a pressure differential > 1 atm, this decrease in permeability is significant and must be considered.

In more recent studies, investigators have used creep indentation, [3, 65] and frequency response measurements of cartilage to calculate the permeability [23]. However, all of these techniques require modeling of the mechanical response of the tissue, and thus the calculated permeabilities are influenced by the assumptions incorporated into the model (e.g. only constant permeability linear models were used). In our investigation, creep responses for both compression and imbibing in confined consolidation conditions were experimentally measured by ultrasound. These responses were then compared to various models to determine the most important necessary physical characteristics. Although this approach does not exclude all modeling assumptions, the influence of these assumptions on the calculation of permeability are minimized by determining the most important physical characteristics of the model directly from the experimental data. Finally, since the necessary disentanglement of PG would occur only under sufficient drag forces produced by the fluid flow, the dependence of permeability on the fluid velocity was examined to determine if there was any indication of channel formation.

3.2 MATERIAL AND METHODS

3.2.1 EXPERIMENTAL

Cartilage Tissue Preparation and Confined Consolidation Apparatus

Three-month-old bovine knees were obtained from the local slaughterhouse and stored at 4°C. Within 4 hr post-mortem, Ø10.2 mm cylindrical cartilage plugs (with subchondral bone) were cored from the femoral condyles under irrigation with sterile 0.9% PBS (with 100 I.U./ml penicillin and streptomycin, 0.2 mM PMSF, 20 mM EDTA, 5mM benzamidine-HCl, and 5 mM NEM at ph 7.2, 4°C, standard). After rinsing with PBS, the plugs were confined in a plexiglass holder (Figure 2.14), and sectioned to 1.5 mm uniform thick plugs as described in Section 2.3.1. On average, the most superficial 50-100 μm of the articular surface was removed to produce uniform thickness cartilage plugs (1.500 ± 0.005 mm as measured by electronic micrometer). The plugs were kept in sterile 0.9% PBS at 4°C after coring, during sectioning, and prior to consolidation.

For all measurements, the plugs were placed inside the confined consolidation chamber shown in Figure 3.1. The chamber and plug were assembled under PBS, and care was taken to remove all possible air bubbles. The chamber was then covered with a latex sock and placed in the temperature controlled bath (Figure 3.2). All measurements were made at 25°C. The plug was loaded by placing weights on the platform, and the displacement of the

interface between the porous piston and cartilage plug was recorded with a 10 MHz Panametrics ultrasound contact transducer driven by a Panametrics ultrasonic analyzer, model 5600, at a repeat rate of 500 Hz. The reflection traces were captured on a Gould 4072 digital oscilloscope and stored on a DEC MicroVax II. Initially, a signature of the first reflection was stored as an average of 128 traces. Then the correlated receiver technique was used to find the time shift between the signature and a reflected signal averaged over two consecutive traces. This was done in the frequency domain by multiplying the Fast Fourier Transform (FFT) of the signature with the complex conjugate of the FFT of the signal. Then the location of the maximum in the inverse FFT of the product corresponds to the desired time shift.

Speed of Sound

The surface displacement, δ, is measured as the time delay between the surface reflection at reference (preload) and the surface reflection at δ.

$$2\delta = c\left(t_{pre} - t_{\delta}\right) \tag{3.1}$$

where c is the speed of sound, t_{pre} is the twice the time of travel between the transducer and the cartilage surface at preload, and t_{δ} is twice the time of travel between the transducer and the cartilage surface at displacement, δ. However, as the cartilage consolidates, the speed of sound does not remain constant and must be measured.

First, the speed of sound in a swollen plug, c_o, was calculated by measuring the swollen plug height, h_o, with an electronic micrometer, and the time delay between the near and far surface, Δt, with a 10 MHz focused ultrasound transducer:

$$c_o = \frac{2h_o}{\Delta t} \tag{3.2}$$

Then simultaneous mechanical and ultrasound displacement measurements were made with various loads, after the plug was allowed to reach equilibrium (3 hr). The ultrasound displacements were calculated with a constant speed of sound, c_o, and the mechanical measurements were made with a gage attached to a micron resolution Micro Control VP 30-25 linear actuator driven by a Micro Control IT6DCA controller (Figure 3.3). Also, the mechanical measurement were adjusted for the compliance of the confined consolidation apparatus, measured separately without the cartilage plug.

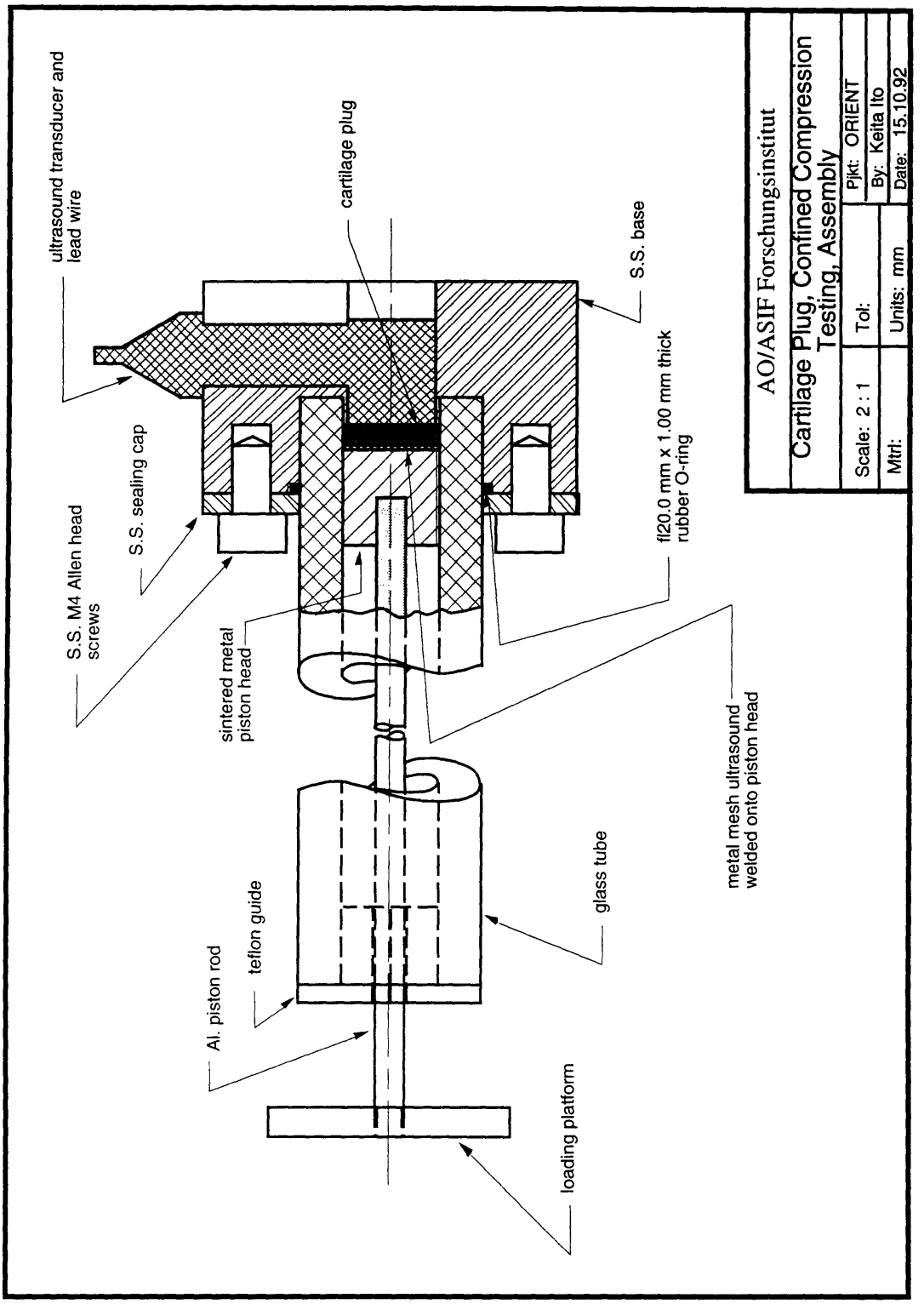

Figure 3.1 Confined Consolidation Chamber Cross-Section.

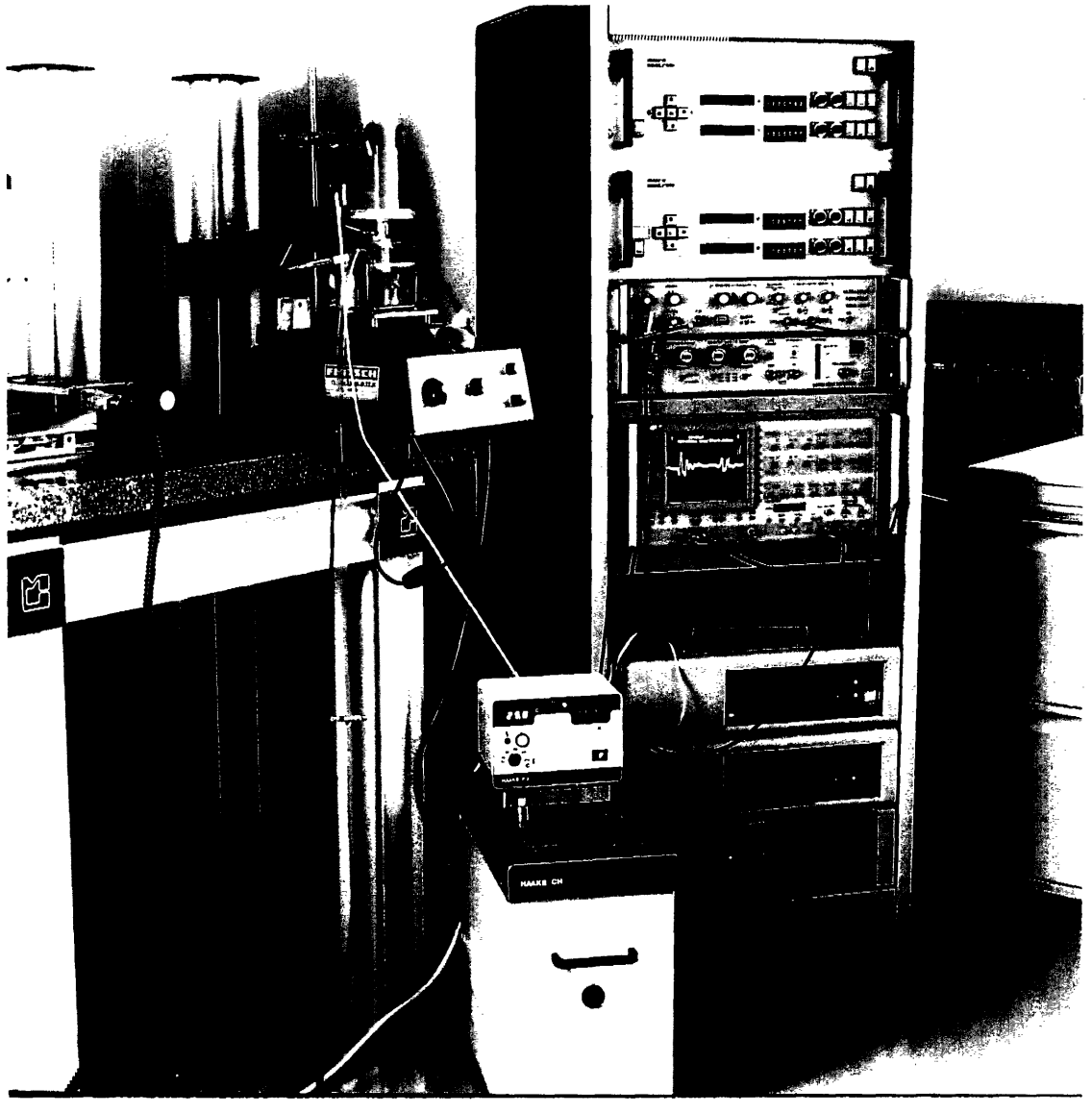

Figure 3.2 Confined Consolidation Chamber in Temperature Controlled Bath on a Dithering Platform shown connected to the Ultrasound Controller, Gould Oscilloscope, Linear Actuator Controllers, and MicroVax II.

Finally the speed of sound, c, can be calculated as a function of strain, ε :

$$c(\varepsilon) = \frac{c_o(1-\varepsilon)}{(1-\delta_{us}/h_o)} \quad \text{from} \quad \varepsilon = \frac{\delta_m}{h_o},\ 2h_i = c_i t_i,\ \text{and}\ 2\delta_{us} = c_o(t_o - t_\delta) \tag{3.3}$$

where: t_o is twice the time of travel between the transducer and the cartilage surface for the swollen plug; δ_{us} is the displacement measured by ultrasound; δ_m is the displacement measured mechanically and adjusted for apparatus compliance; and h_i, c_i, and t_i are the height of the plug, the speed of sound, and twice the time of travel between the transducer and the plug surface at some instance i, respectively.

Equilibrium Modulus

The equilibrium modulus, L, was measured for two plugs by ultrasound with a dithering platform shown in Figure 3.1. The signature was taken at zero load, and the displacements were measured for every +200 g load up to 2200 g, after allowing the plug to reach equilibrium (3 hr). The traces were captured with a resolution of 2.44×10^{-9} sec, or with a nominal speed of sound of 1500 m/sec, a displacement resolution of 1.83 μm (Eqn 3.3). The displacements were calculated initially with a constant speed of sound (that of the swollen plug) and later corrected by the actual speed of sound as a function of the strain measured as described above.

Consolidation

The consolidation was also measured using the set-up in Figure 3.1. Cartilage plugs were placed in the consolidation chamber and allowed to equilibriate overnight with a preload of 1704g at 4°C and dithering. After the temperature was increased to 25°C and no thermal drift was detectable (1hr), the consolidation was measured with dithering for: 1) compression with +568g from preload, 2) imbibing with -568g back to preload, 3) further imbibing with -568g from preload, and 4) final compression with +568g back to preload. The signals were sampled every 2 sec, averaged over two consecutive traces (repeat rate of 500 Hz), over a 3 hr period for each weight. The trace resolution and calculation of the displacements were the same as that described for the equilibrium modulus measurements.

3.2.2 THEORETICAL

Over the last three decades, various models have been developed to model the mechanical response of cartilage tissue. The theory of viscoelastic materials was applied as a phenomenological description of cartilage response. Initially, simulations in the time domain agreed relatively well with experimental data, and later as discrepancies were discovered, the number of parameters in the model was increased to agree with experimental results [29]. There are also the continuum models, utilizing mixture theory [67] and Biot's soil mechanics

[58]. These models have been widely used, and may eventually prove to be the most useful. However, they are quite complex which makes it difficult to derive insights into the physical interaction of ECM components.

Analytical Model

In this study, cartilage will be modeled as an elastic network moving through an incompressible Newtonian fluid, with uniaxial strain conditions. The modeling assumption of one homogeneous network (although the solid network is composed of collagen and PG) is valid because the PGs and collagen move together (PGs are entrapped and possibly bound to the collagen network), and also because the response of the collagen is much quicker than the PGs which dominate the compression characteristics of the tissue. The equation of motion for the solid network is a diffusion equation developed from gel theory [91],

$$\frac{\partial u(z,t)}{\partial t} = D\frac{\partial^2 u(z,t)}{\partial z^2} \tag{3.4}$$

where u is the displacement of the network (+ve for compression) at some depth, z, and time, t; D = L/f is the diffusion coefficient; L is the uniaxial strain equilibrium modulus of the network; and f is the force per unit volume (of the network) moving through the fluid with unit speed. The diffusion coefficient, D, can also be written as D = Lk, where k is the permeability.

For uniaxial confined consolidation, the boundary conditions are:

$$\begin{aligned} &u = 0 \text{ at } z = h \text{ (bottom)} \\ &\frac{\partial u}{\partial z} = -\frac{\delta_o}{h}L = -\sigma_o \text{ at } z = 0 \text{ (surface)} \end{aligned} \tag{3.5}$$

where δ_0 is the final displacement (+ve for compression); h is the depth (height) of the plug; and σ_0 is the applied stress at the surface. For a step load the initial conditions are:

$$u = 0 \text{ at } t = 0 \tag{3.6}$$

The solution of Eqn 3.4 with boundary conditions 3.5 and initial condition 3.6 is given by:

$$u(z,t) = \delta_o\frac{h-z}{h} + \sum_{n=1}^{\infty}\frac{(-1)^{2n-1}}{(2n-1)^2}\frac{8\delta_o}{\pi^2}e^{\frac{-(2n-1)^2\pi^2 Dt}{4h^2}}\sin\frac{(2n-1)\pi(h-z)}{2h} \tag{3.7}$$

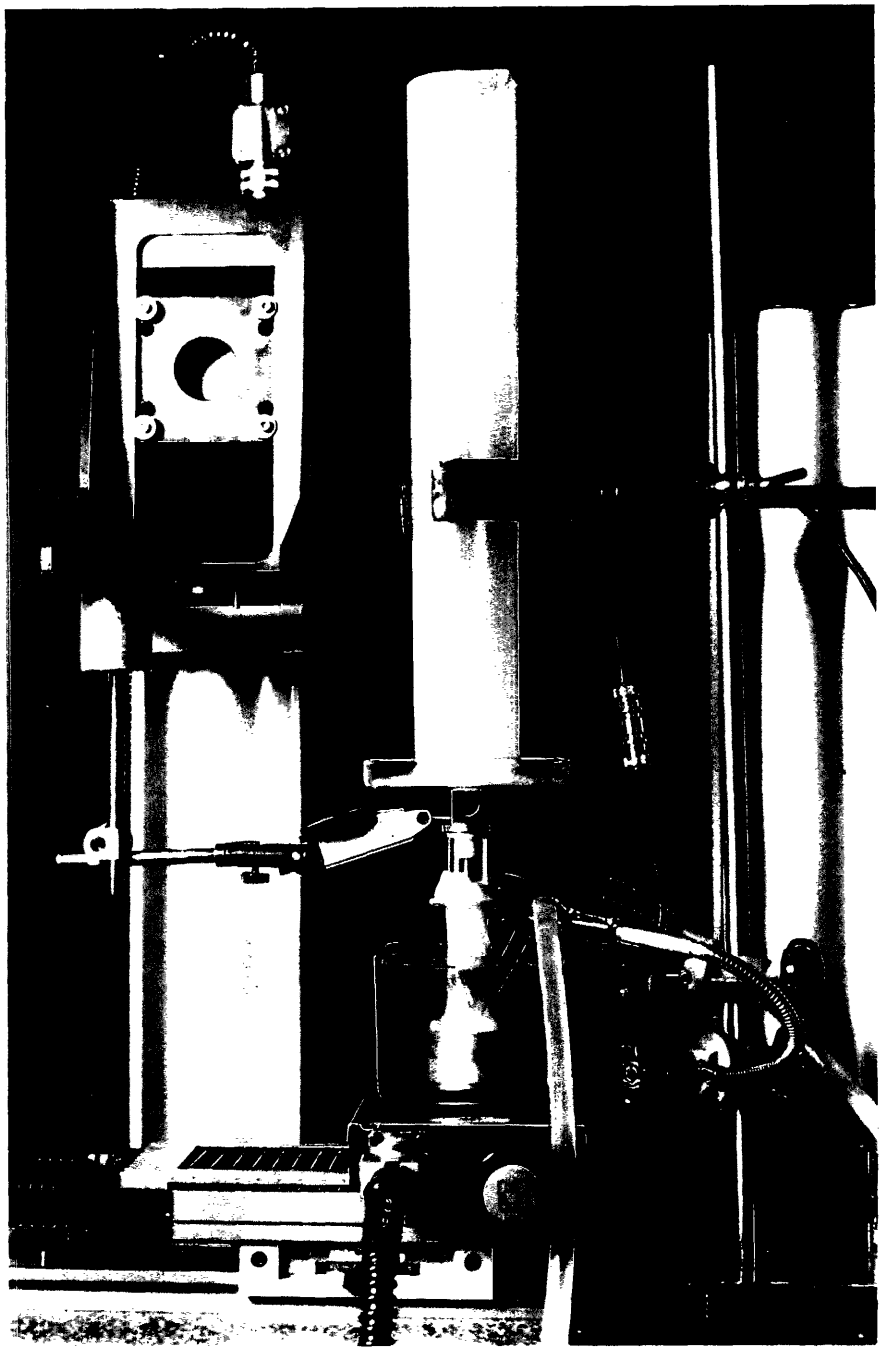

Figure 3.3 Confined Consolidation Chamber in Temperature Controlled Bath with a Gage on the Z-Stage Linear Actuator for mechanical Measurements.

At the surface:

$$u(0,t) = -\delta_o + \frac{8\delta_o}{\pi^2}\sum_{n=1}^{\infty}\frac{1}{(2n-1)^2}e^{-(2n-1)^2 t/\tau} \tag{3.8}$$

where

$$\tau = \frac{4h^2}{\pi^2 D} \tag{3.9}$$

is the fundamental time constant.

Lumped Parameter Model

Although a series solution exists for the equation of motion with appropriate conditions in the time domain for the linear model, as non-linear models are investigated, an analytical solution in the time domain will not always be available. Hence, we will start with an equivalent linear lumped parameter model used by Tepic, [94]. The elastic network in an incompressible fluid is modeled as a series of basic elements:

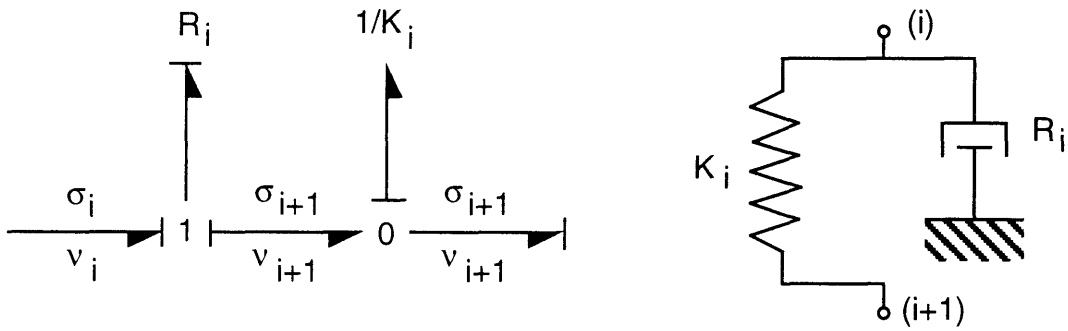

where: v_i is the velocity of the network moving through the stationary fluid and σ_i is the stress in the network; R_i is the viscous drag of the fluid on the network element; and K_i is the stiffness of the network element.

$$R_i = \frac{h}{kn} \quad \text{and} \quad K_i = \frac{Ln}{h} \tag{3.10}$$

For n basic elements in series, the response of the tissue can be described by n-sets of ordinary differential equations:

$$\begin{aligned}
\dot{x}_1 &= \frac{-K_1}{R_1}(x_1 - x_2) + \frac{\sigma_o}{R_1} \\
\dot{x}_2 &= \frac{-K_2}{R_2}(x_1 - 2x_2 + x_3) \\
\dot{x}_3 &= \frac{-K_3}{R_3}(x_2 - 2x_3 + x_4) \\
&\bullet \\
&\bullet \\
\dot{x}_{n-1} &= \frac{-K_{n-1}}{R_{n-1}}(x_{n-2} - 2x_{n-1} + x_n) \\
\dot{x}_n &= \frac{-K_n}{R_n}(x_{n-1} - 2x_n)
\end{aligned} \tag{3.11}$$

These ODEs were then numerically integrated with an adaptive step size controlled 4th order Runga-Kutta routine from Numerical Recipes in C, on a Silicon Graphics Indigo computer [78]. As the number of basic elements, i, approaches ∞, the surface displacement, x_1, approaches that described by Eqn. 3.8. In Figure 3.4, maximum percent difference, $|u(0,t) - x_1| / u(0,t)$, is less than 0.1% when n = 255 for h = 1500 μm, L = 0.145 MPa, σ_0 = 12490 Pa, δ_0 = 129.2 μm, and k = 1.28 x 10^{-16} m^4/N sec.

Finally, in order to determine which physical characteristics were most important for modeling the creep response of cartilage, a least squares criterion, non-linear fit of parameter values to experimental data was done using the Design Optimization Control Program (DOC) and the Design Optimization Tools Program (DOT) from VMA Engineering (Goleta, CA). DOT uses a modified feasible directions algorithm [99] to find the minimum for a given object function (in our case, least squares criterion), and stops when the Kuhn-Tucker conditions are met [8] or when the criterion function converges to a predetermined relative and/or absolute tolerance. DOC is simply a program to allow convenient interfacing between the analysis code and DOT.

3.3 RESULTS

3.3.1 SPEED OF SOUND

The speed of sound in the swollen plug was calculated to be 1544 m/sec, which is as expected, higher than the speed of sound in water (1495 m/sec) at 25°C, 1 atm. The ultrasound and mechanical displacements were measured for three plugs at loads of 200 g, 1000 g, 1400 g, and 1800 g corresponding to strains of 8.4%, 28%, 34.8%, and 40% respectively. The speed of sound was calculated and a linear least squares regression fit was used to find the speed of sound as a function of strain (Figure 3.5):

$$c(\varepsilon) = m\varepsilon + b = 51.30\ \varepsilon + 1543.8 \tag{3.12}$$

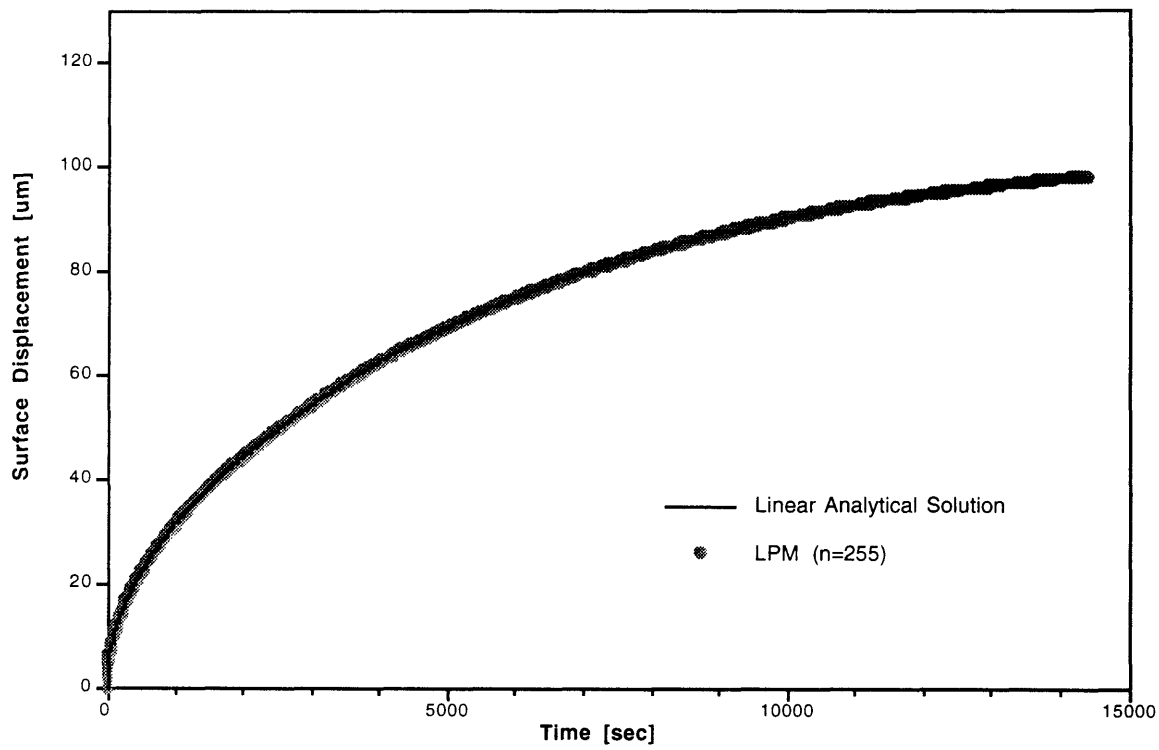

Figure 3.4 Comparison of Linear Analytical Model Solution vs. Linear Lumped Parameter Model Simulation for Creep Compression.

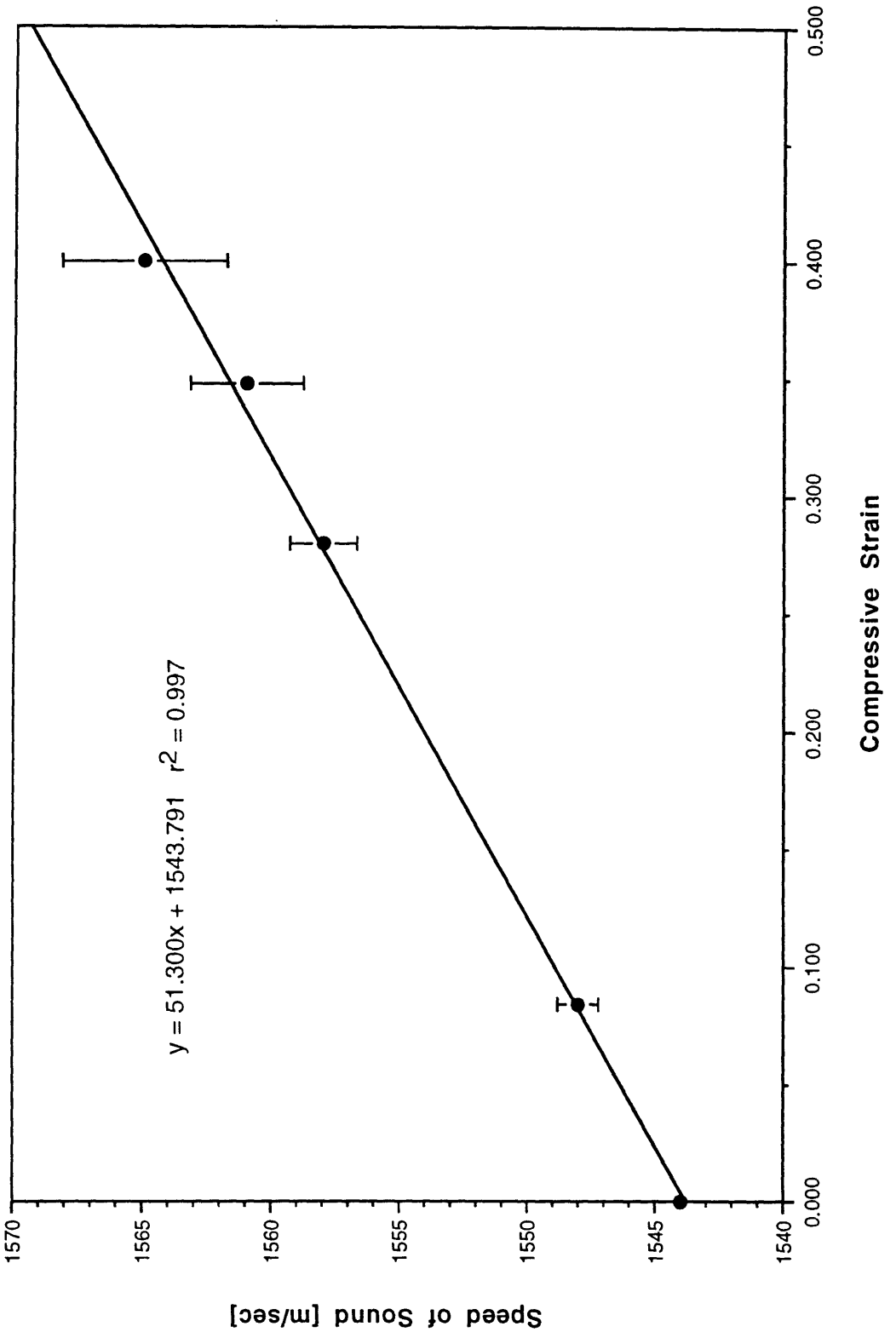

Figure 3.5 Speed of Sound in 3-month-old Bovine Articular Cartilage.

Massachusetts Institute of Technology

3.3.2 EQUILIBRIUM MODULUS

The actual displacements at equilibrium for each load were measured with respect to the displacement at equilibrium for the previous load (i.e. signatures were taken before the addition of a load increment). The unadjusted strains, ε_{us}, were calculated from the summation of relative ultrasound displacement measurements (ε are assumed linear). To adjust for the speed of sound changes with strain, Eqn 3.3 can be combined with the linear function fit to the speed of sound measurements (Eqn 3.12) to give:

$$\varepsilon = \frac{c_o \varepsilon_{us}}{m(1-\varepsilon_{us})+c_o} \tag{3.13}$$

where: $c(\varepsilon) = m\varepsilon+b$ is the linear fit to the speed of sound measurements and $b = c_O$.

When the averaged stress vs. compressive strain curve was plotted (Figure 3.6), the modulus appeared constant up to 22% strain after which the modulus increased with further compressive strain. Hence, a least squares regression fit was done in two parts: a linear fit for $0 \le \varepsilon_C \le 0.22$, and a second order polynomial fit for $\varepsilon_C \ge 0.22$, where ε_C is the compressive strain. This gave stress as a function of strain, $\sigma(\varepsilon)$:

$$\begin{aligned} \sigma_c &= 3567.4\varepsilon_c^2 - 669.25\varepsilon_c + 138.38 \text{ for } 0.22 \le \varepsilon_c \\ \sigma_c &= 733.48\varepsilon_c + 0.652 \text{ for } 0 \le \varepsilon_c \le 0.22 \end{aligned} \tag{3.14}$$

and an equilibrium modulus, L[MPa] (Figure 3.7):

$$\begin{aligned} L\left[MPa\right] &= 7.135\varepsilon_c - 0.6693 \text{ for } 0.22 \le \varepsilon_c \\ L\left[MPa\right] &= 0.7335 \text{ for } 0 \le \varepsilon_c \le 0.22 \end{aligned} \tag{3.15}$$

Only two plugs were measured, but the values are in agreement with previous investigations [67].

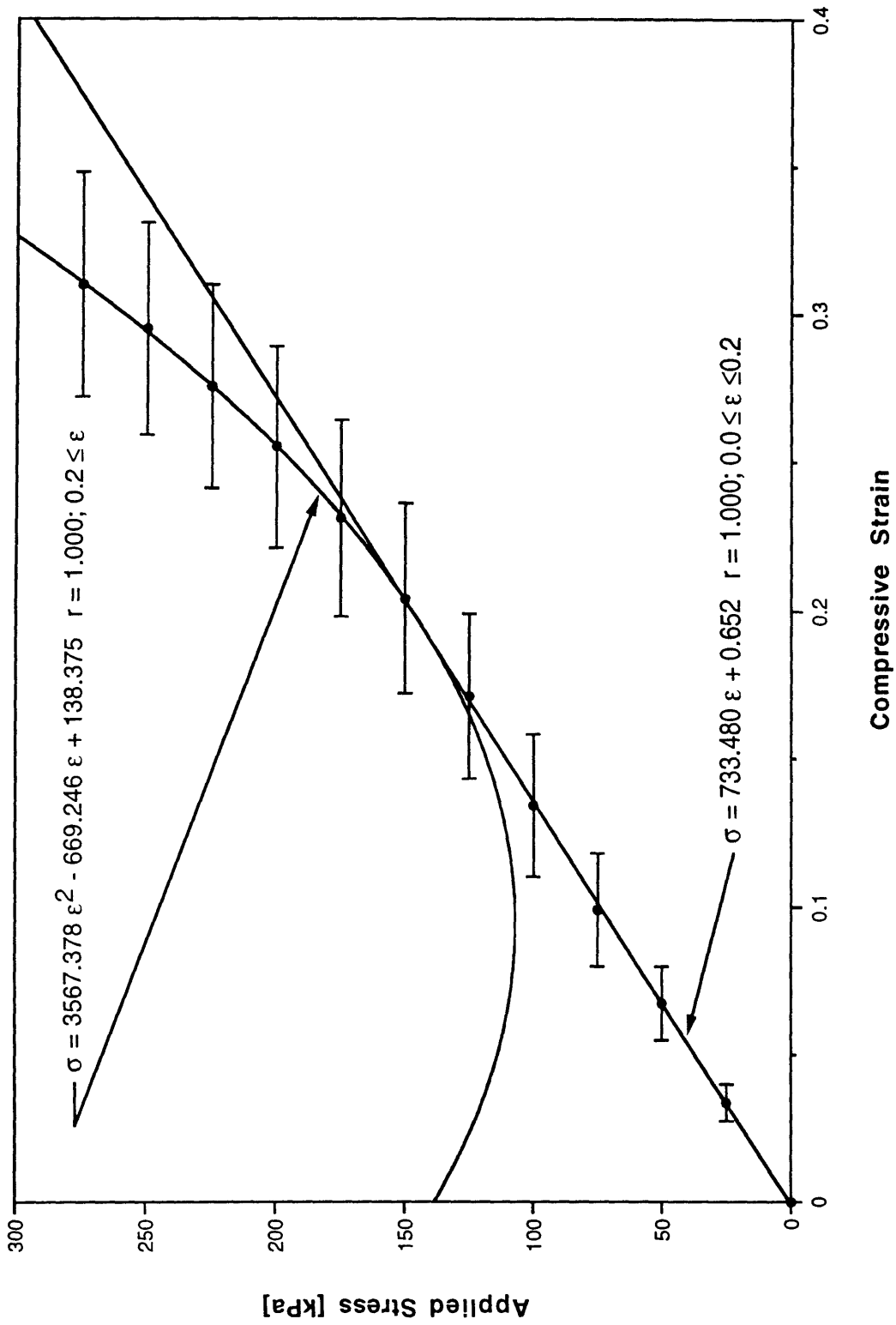

Figure 3.6 Equilibrium Stress/Strain Measurements of 3-month-old Bovine Articular Cartilage in Confined Consolidation.

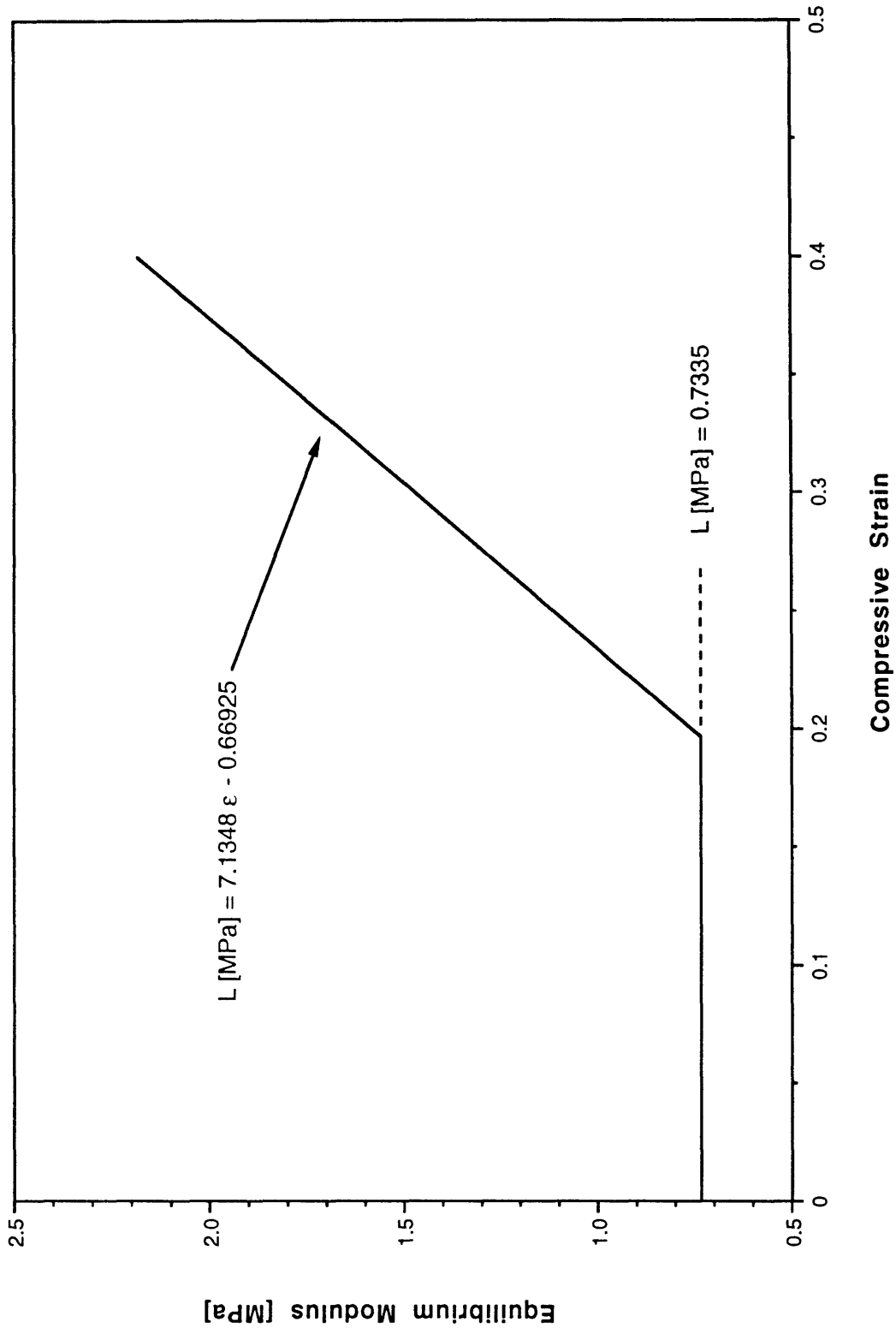

Figure 3.7 Equilibrium Modulus of 3-month-old Bovine Articular Cartilage in Confined Consolidation.

3.3.3 CONSOLIDATION

Five plugs were tested in creep and one of the five was tested twice consecutively to determine repeatability of the measurements. First the creep data was adjusted for the change in speed of sound with strain. However this was not done directly because the required compressive strain at preload, ε_{pre}, was unknown (only the change in strain for a change in applied stress was known). Initially, the compressive strain at preload, ε'_{pre} from the stiffness function (Eqn 3.14), and the speed of sound function (Eqn 3.12)were used to calculate the creep strains, ε (from Eqn 3.1):

$$\varepsilon = \frac{1 + b\left(\frac{\delta_{us}}{h_o c_o} + \frac{\varepsilon'_{pre} - 1}{c'_{pre}}\right)}{1 - m\left(\frac{\delta_{us}}{h_o c_o} + \frac{\varepsilon'_{pre} - 1}{c'_{pre}}\right)} \tag{3.16}$$

where δ_{us} is the displacement as measured by ultrasound, ε'_{pre} is the assumed preload strain, and c'_{pre} is the speed of sound at the assumed preload strain. Then, the known change in adjusted strain for a change in applied stress was used to calculate the preload strain as:

$$\varepsilon_{pre} = \left(\frac{\left(\varepsilon_{+\Delta load} - \varepsilon'_{pre}\right) + \left(\varepsilon'_{pre} - \varepsilon_{-\Delta load}\right)}{2\Delta load}\right)\frac{preload}{\Delta load} \tag{3.17}$$

This was used to back check our initially assumed preload strain of 19.9±1.2% (from stiffness function) and was found to differ by ≤ 0.1%.

A typical creep cycle is shown in Figure 3.8. Because displacement measurements were recorded every 2 sec over 3 hr of creep, only 50 unevenly distributed points were used to display the creep curves and 200 evenly distributed points were used to fit the model parameters. After the initial compression (preload + 568 g) and imbibing (- 568 g to preload), the net surface displacement is negative. However after a full creep cycle (further -568 g then +568 g back to preload), the net surface displacement is zero. This initial offset was evident for every plug, and is probably due most to static friction of the compressed plug on the confining walls of the consolidation apparatus. Because this offset of -12.6±3.8 μm corresponded to 10% of the actual loads (57.3 ± 9.3 g/ 568 g), when comparing the

compression to imbibing creep, the displacements and loads must be adjusted by the ratio of final displacements or normalized by the final displacements (e.g. the load for the preload-568 g imbibing creep is 568 g, however the load for the +568 g to preload compression creep is 568 g*δ_{comp} / $\delta_{imb.}$).

The normalized creep curves for compression and imbibing between 12 - 20 % compressive strain (i.e. preload-568 g and +568 g to preload) are show in Figures 3.9 to 3.13. Each plug shows a trend of slower or equal imbibing compared to compressive creep. However, when the data is averaged over all six trials (one plug cycled twice), this difference between compression and imbibing is not apparent (Figure 3.14). Also since the interplug difference (Figure 3.11) for two different measurements are so repeatable and show this consistent difference, the creep data for each plug was processed separately.

3.3.4 ANALYTICAL MODEL

The compression and imbibing experimental data shown in Figure 3.9 to 3.13 were fit to the linear gel diffusion model (analytical) described by Eqn 3.8. The raw, speed of sound adjusted, data was reduced to 200 evenly distributed points, and the best fit constant permeability and final displacement was found using least squares regression criteria with DOC/DOT. The series solution was summed for n-terms until the solution converged to within 0.1%. The results for each plug are shown in Table 3.1. The average final displacements and permeabilities are: 113.5 ± 7.7 μm and 0.342 ± 0.078 m^2/Pa sec for imbibing creep and 99.8 ± 5.9 μm and 0.408 ± 0.057 m^2/Pa sec for compression creep. The best fit and worse fits (as measured by RMS of the least squares criterion) are for plug H2 and plug G, and are shown in Figure 3.15 and 3.16. The linear model fits the creep curves fairly well, but they always underestimate the initial and late response.

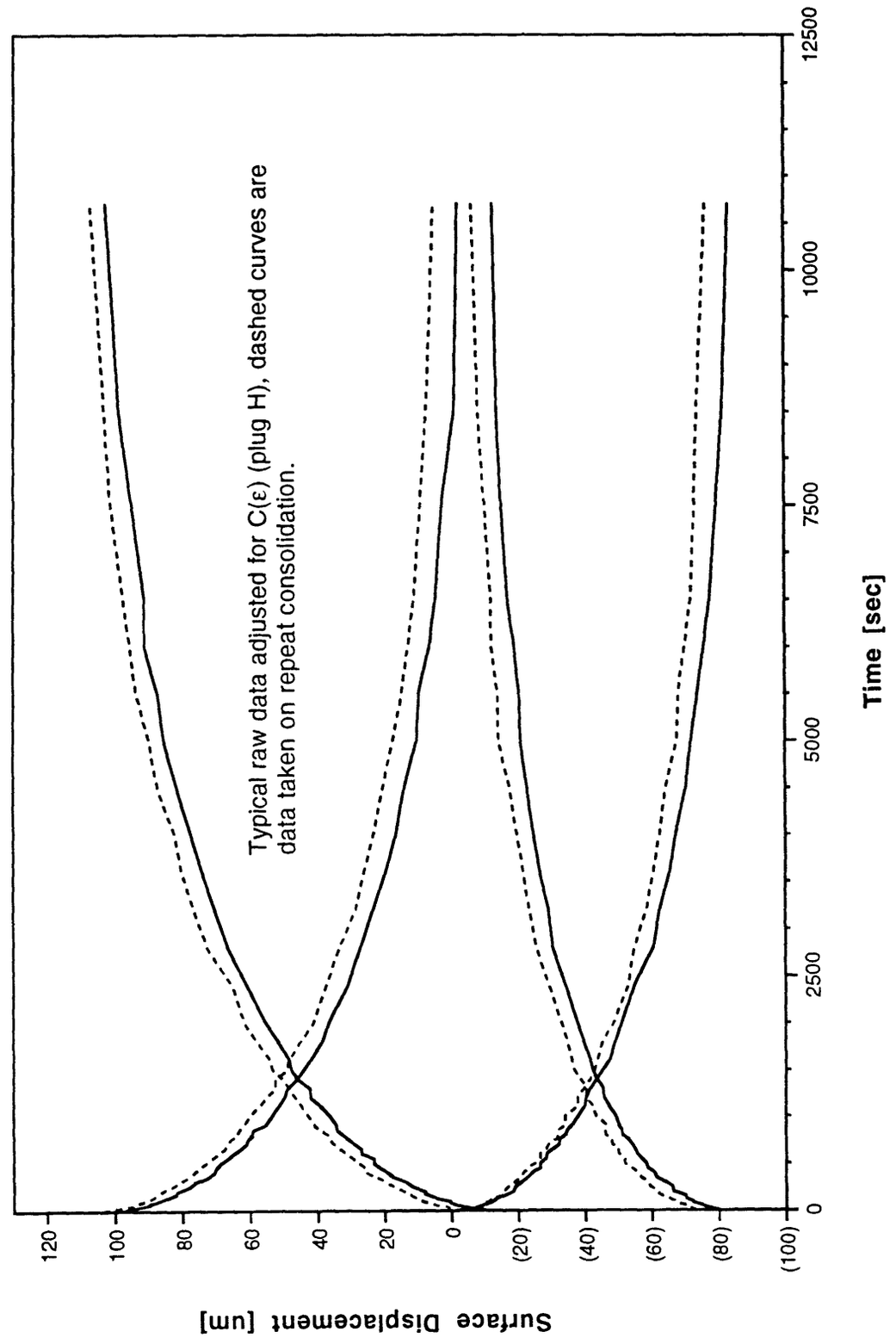

Figure 3.8 Typical Creep Curves for 3-month-old Bovine Articular Cartilage in Confined Consolidation.

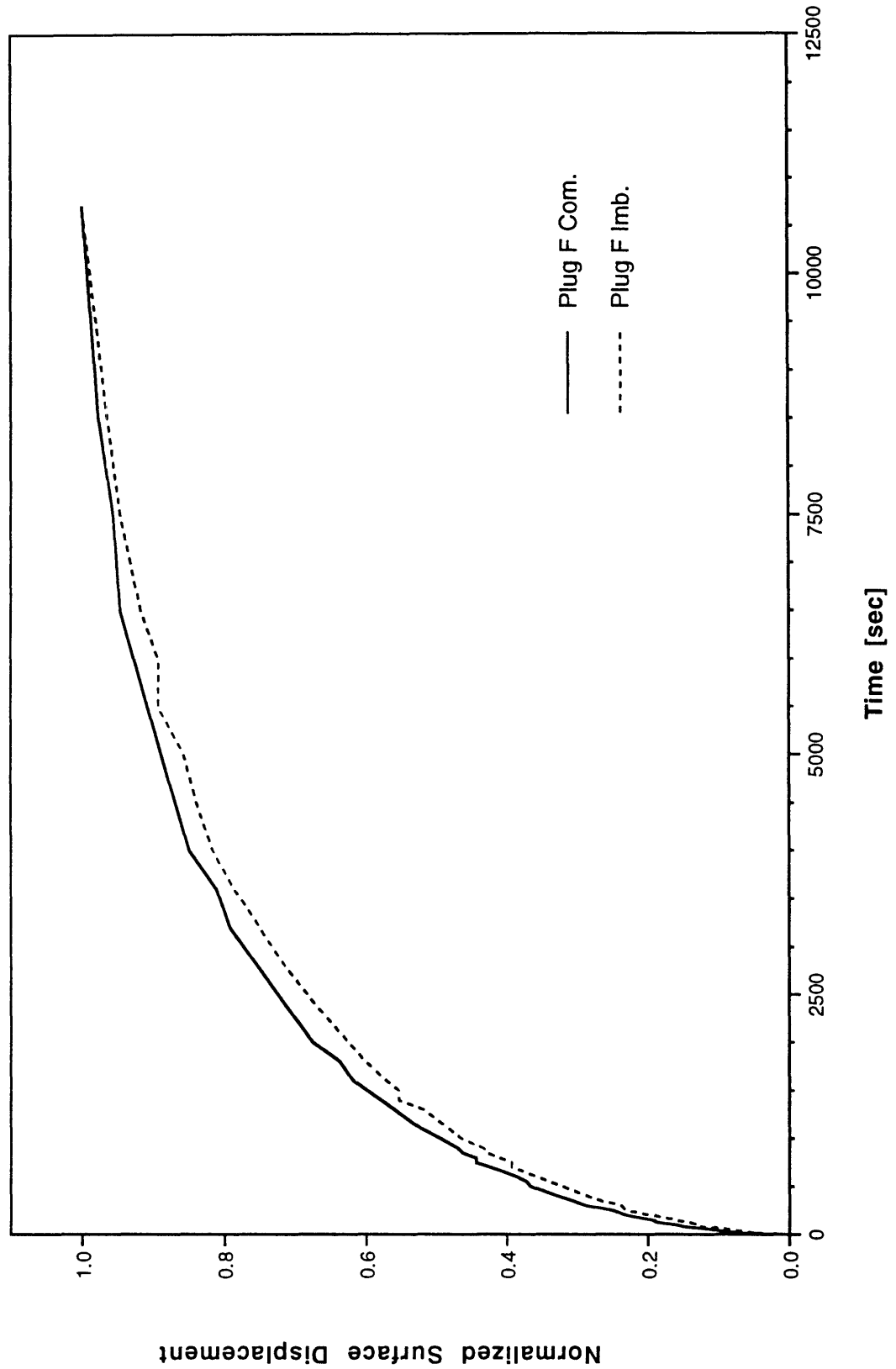

Figure 3.9 Normalized Compression and Imbibing Creep Curves for 3-month-old Bovine Articular Cartilage in Confined Consolidation, Plug F.

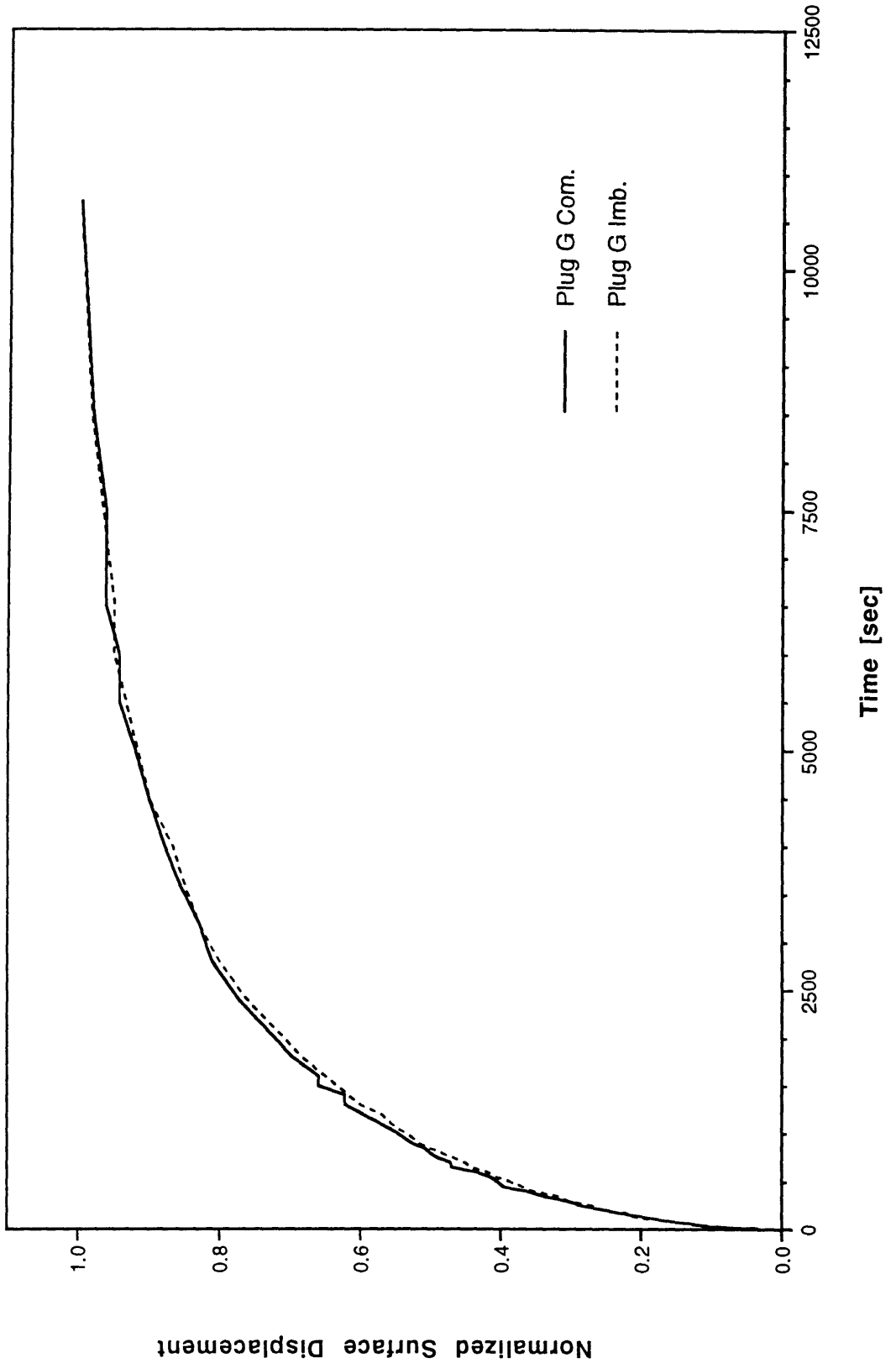

Figure 3.10 Normalized Compression and Imbibing Creep Curves for 3-month-old Bovine Articular Cartilage in Confined Consolidation, Plug G.

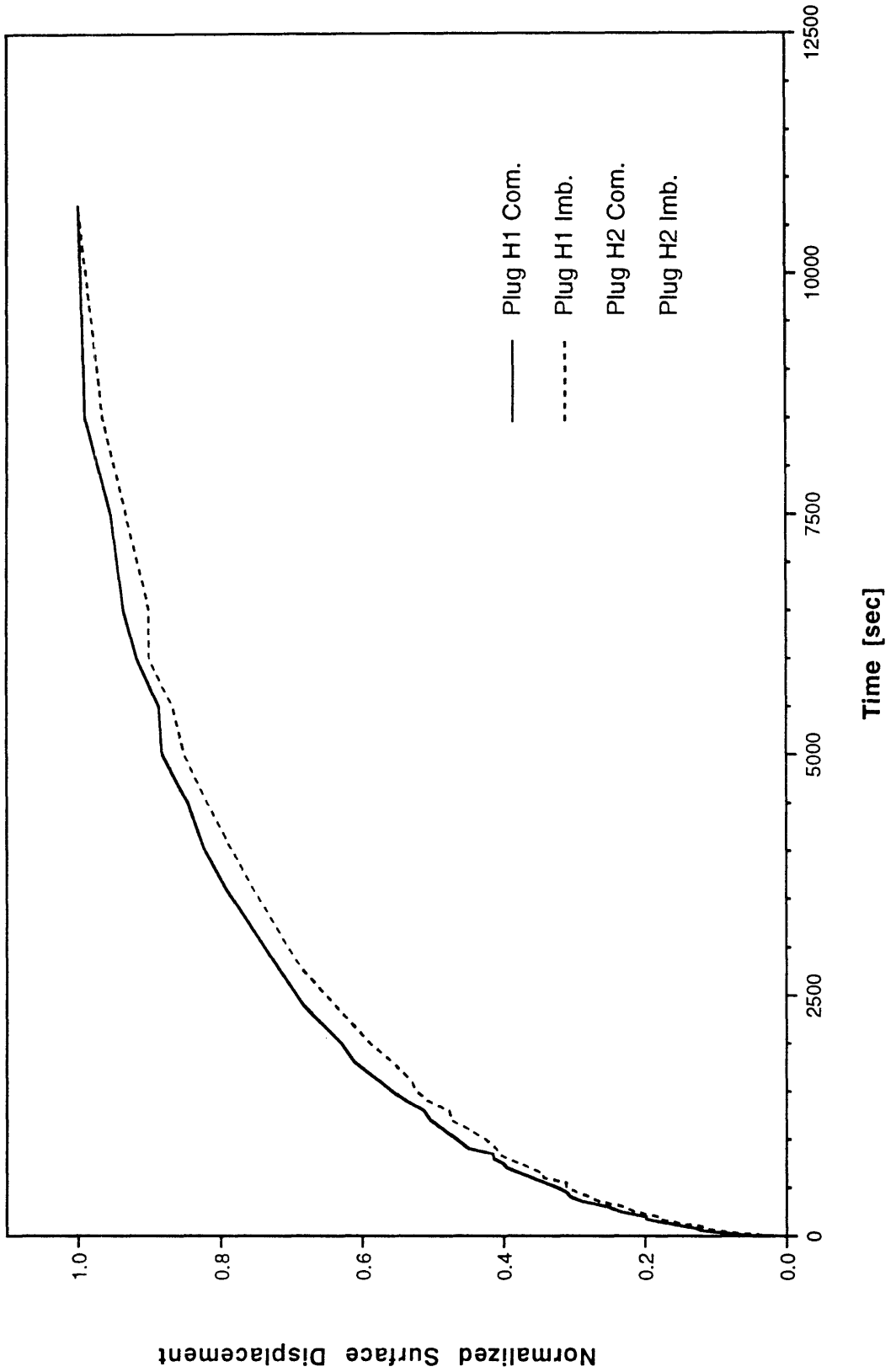

Figure 3.11 Normalized Compression and Imbibing Creep Curves for 3-month-old Bovine Articular Cartilage in Confined Consolidation, Plug H (two trials, H1 and H2).

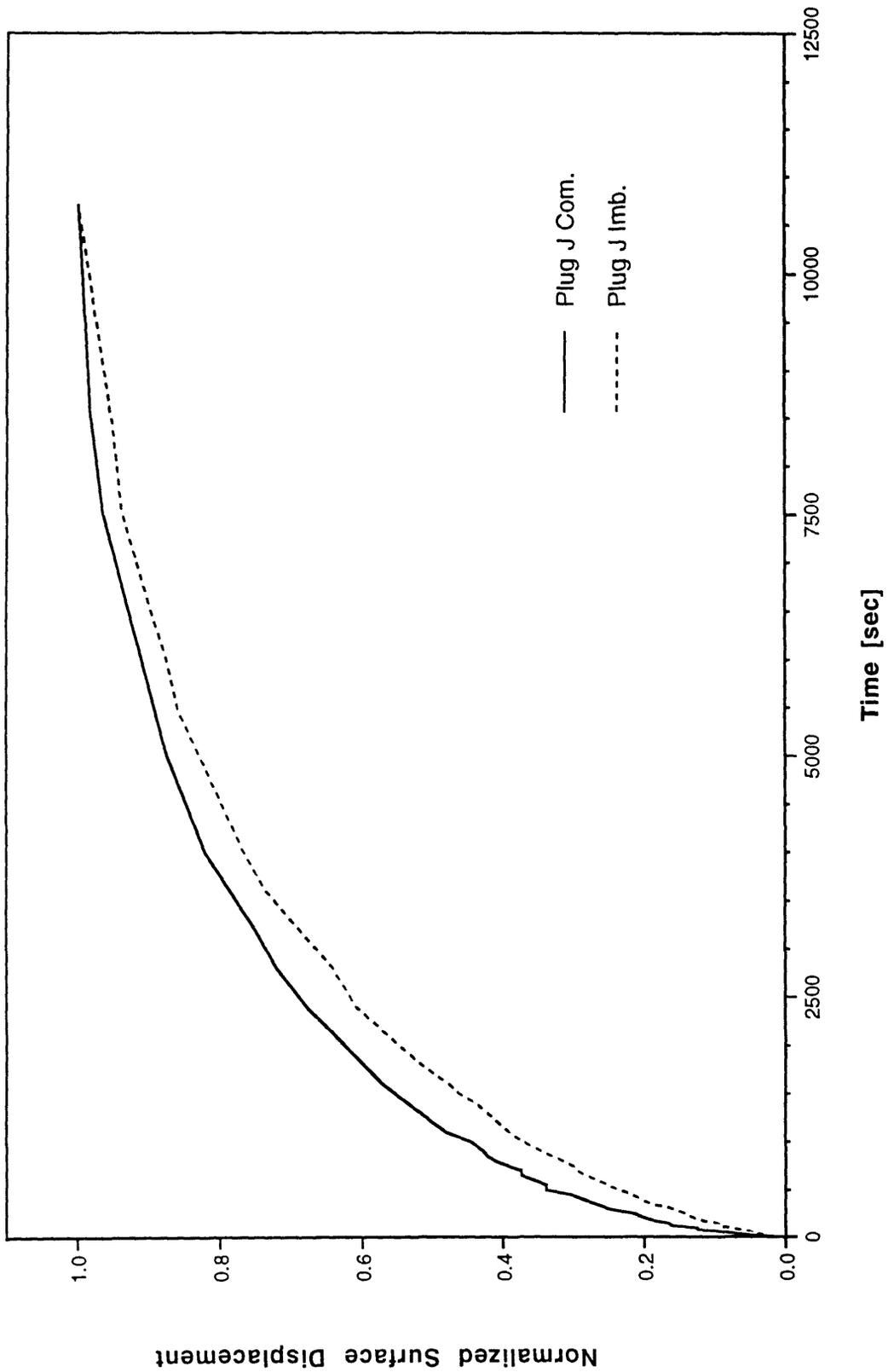

Figure 3.12 Normalized Compression and Imbibing Creep Curves for 3-month-old Bovine Articular Cartilage in Confined Consolidation, Plug J.

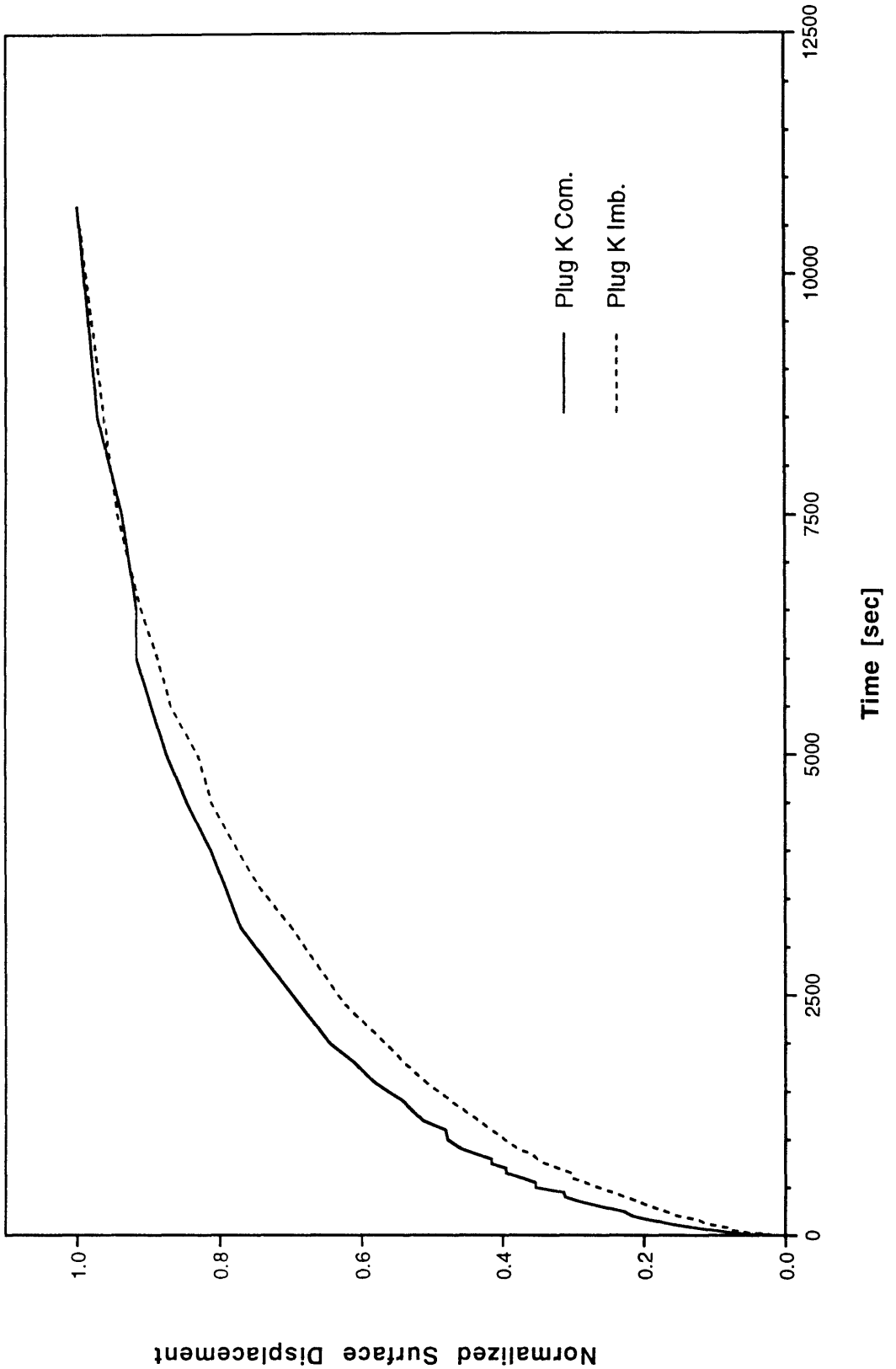

Figure 3.13 Normalized Compression and Imbibing Creep Curves for 3-month-old Bovine Articular Cartilage in Confined Consolidation, Plug K.

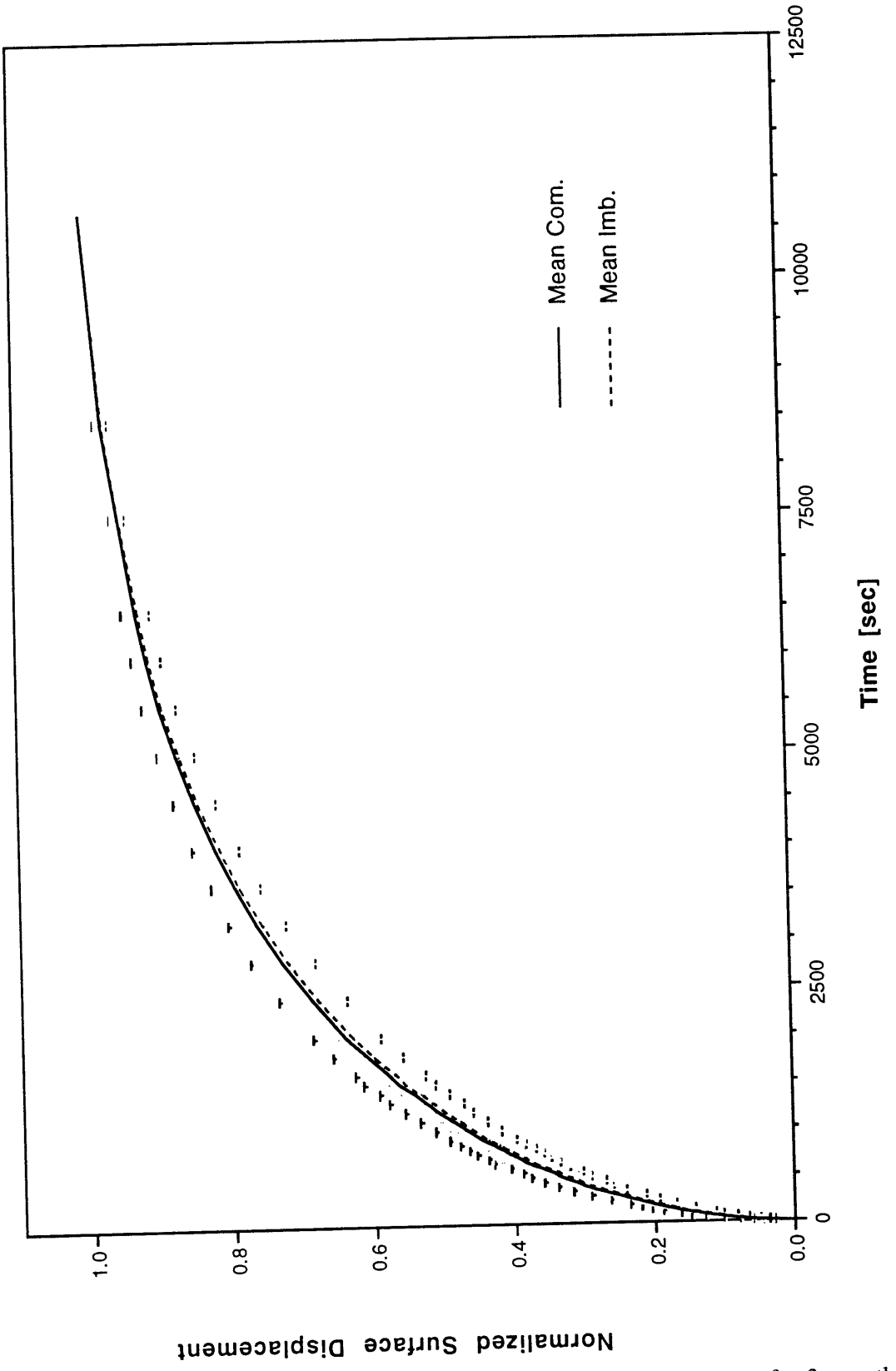

Figure 3.14 Averaged Normalized Compression and Imbibing Creep Curves for 3-month-old Bovine Articular Cartilage in Confined Consolidation.

Table 3.1 Permeabilities and Final Displacement from Least Squares Criterion Fit of the Linear Analytical Model to Experimental Creep Data.

PLUG	IMBIBING			COMPRESSION		
	Final Disp. δ_f [μm]	Permeability k x10^{15} [m^2/Pa sec]	Mean Error [μm]	Final. Disp. δ_f [μm]	Permeability k x10^{15} [m^2/Pa sec]	Mean Error [μm]
F	104.8	0.368	1.0	96.6	0.399	1.0
G	112.1	0.498	1.2	98.1	0.531	1.2
H1	117.1	0.324	1.0	106.0	0.371	1.0
H2	116.2	0.319	0.9	102.7	0.385	1.0
J	126.6	0.288	1.3	106.0	0.400	0.9
K	103.9	0.254	0.9	89.3	0.359	1.0

3.3.5 SURFACE RESISTANCE

The possibility that the surface resistance, due to the interaction between the cartilage plug and the porous piston, could account for the difference between compression and imbibing creep permeabilities was investigated. However, for the resistance to account for this difference, the surface resistance must decrease in compression and increase in imbibing. This is rather unlikely, because if there is any difference in surface resistance, the resistance during compression should be greater than that during imbibing due to the drag of the cartilage solid matrix of cartilage into the permeable piston pores during compression and the reverse during imbibing.

Nevertheless the magnitude of this surface resistance was estimated, by adding the resistance to the linear lumped parameter model (Section 3.2.2) and finding the best fit value of the resistance to an experimental imbibing creep data. The surface resistance was added as a damper to ground, with damping coefficient R_S, on the basic unit at the surface. This model was fit to the experimental imbibing creep curve from plug H2 (trial 2) using least squares criterion with DOC/DOT and starting values for the final disp. and permeability from the fit

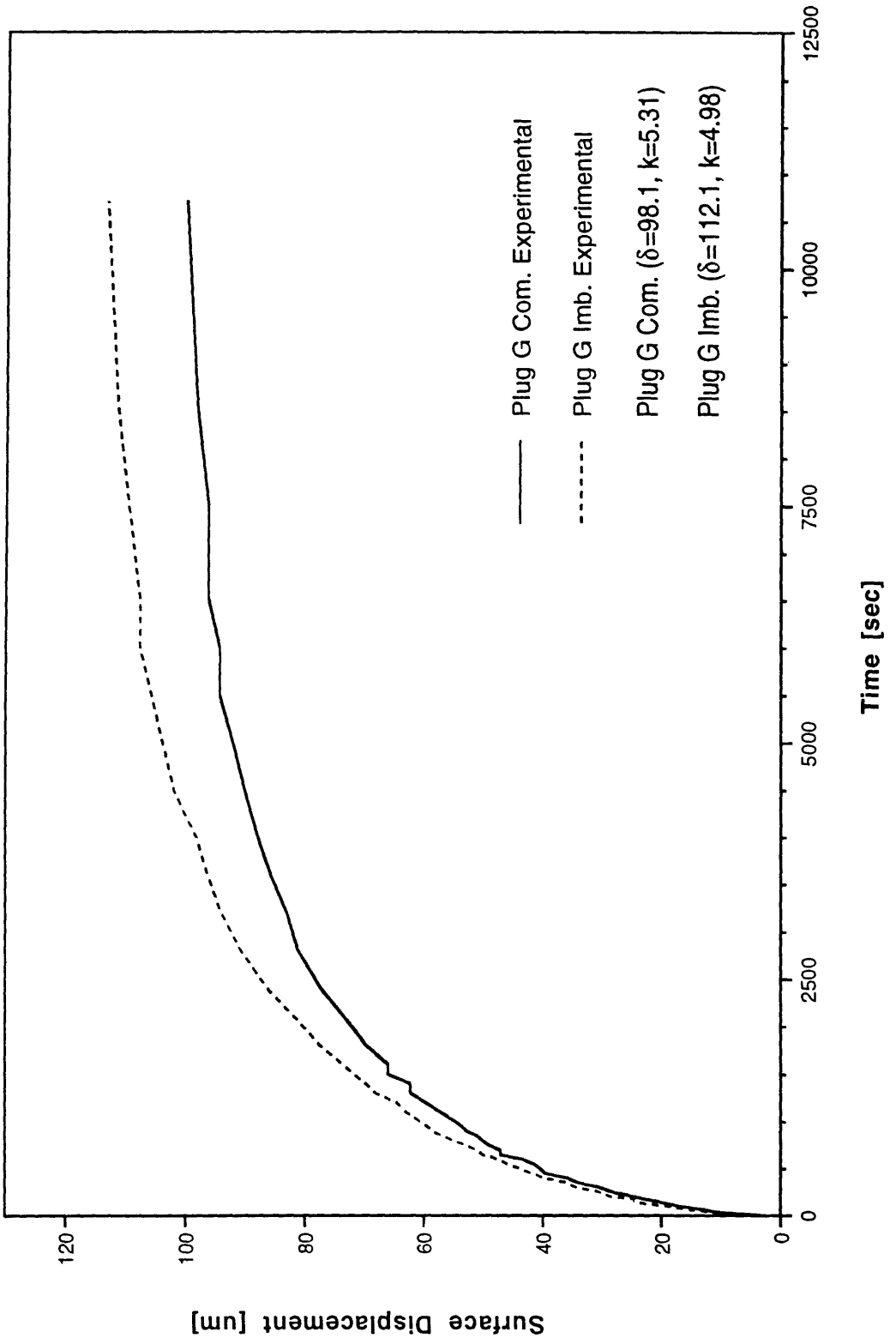

Figure 3.15 Best Fit Linear Model and Experimental, Compression and Imbibing Creep Curves for Plug G.

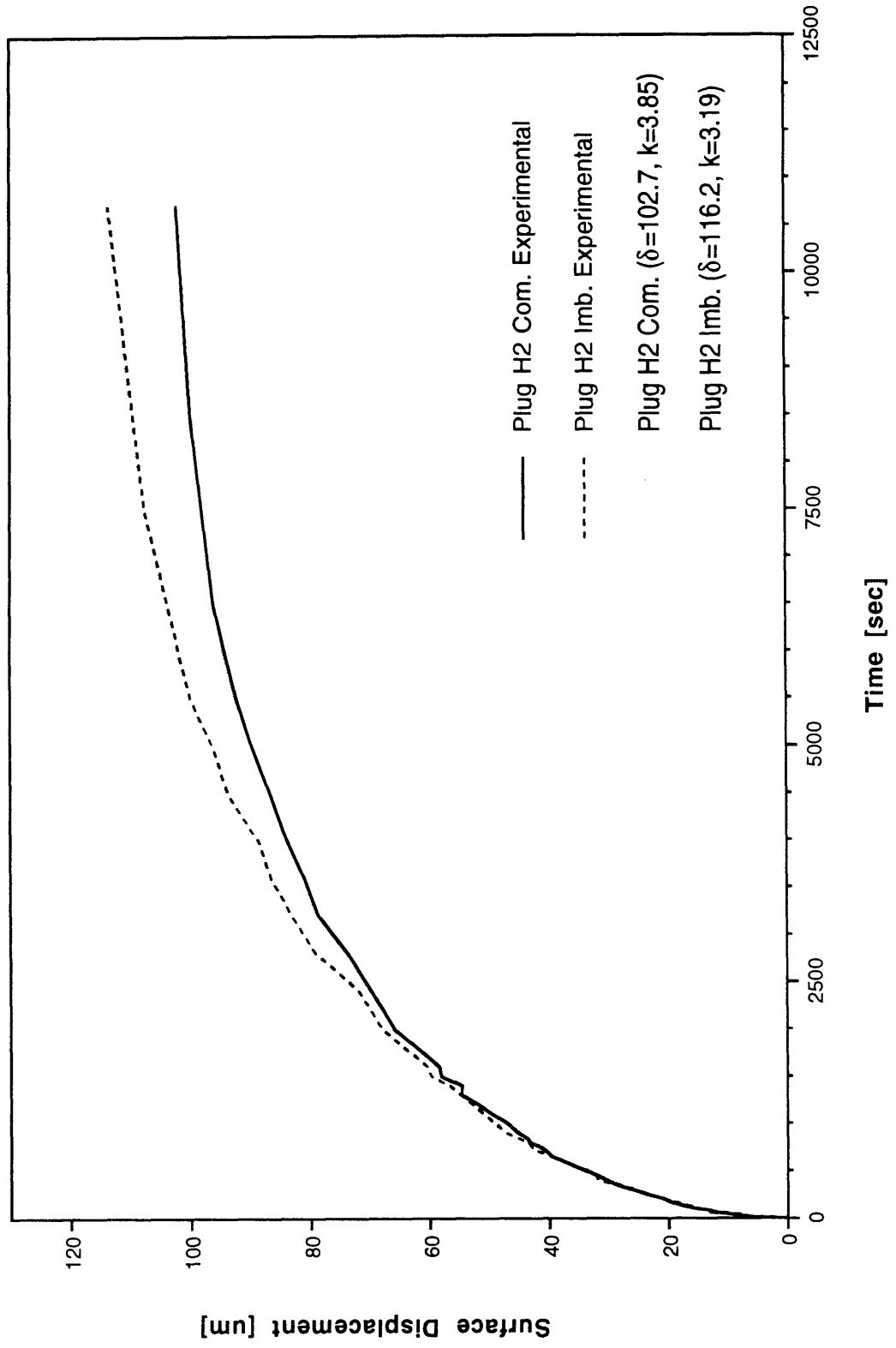

Figure 3.16 Best Fit Linear Model and Experimental, Compression and Imbibing Creep Curves for Plug H2 (2nd trial).

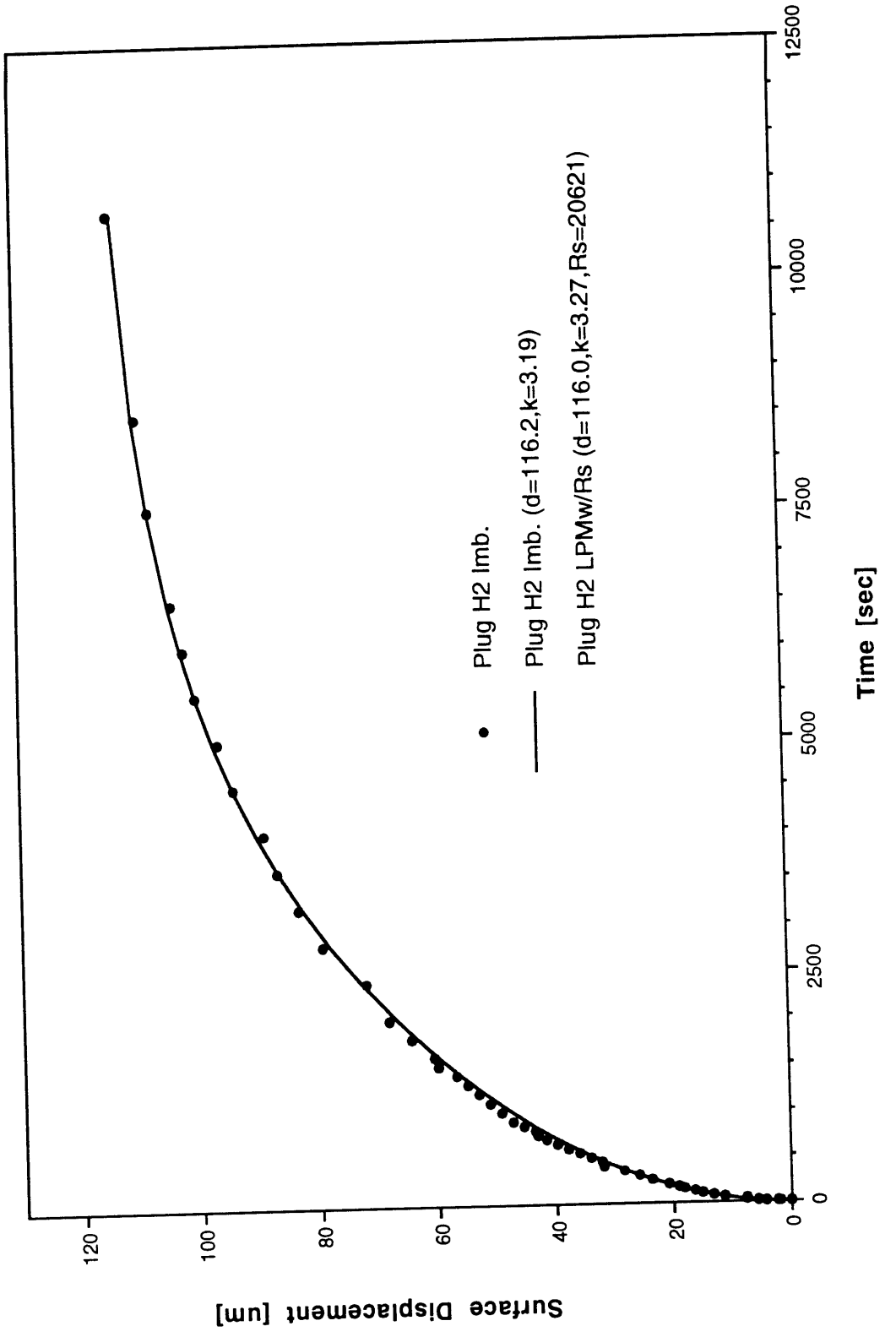

Figure 3.17 Comparison of Best Fit Linear LPM with Surface Resistance, Linear Analytical Model and Experimental, Imbibing Creep Curves for Plug H2 (2nd trial).

to the linear analytical model (Table 3.1). The best fit value for surface resistance was found to be 20.6×10^9 Pa sec/m. This corresponds to a layer of cartilage with a thickness of 0.4% of the cartilage plug. As is shown in Figure 3.17, this amount is insignificant and will be neglected for the remainder of this analysis.

3.4 DISCUSSION

3.4.1 STRAIN DEPENDENT PERMEABILITY

Many investigators have measured the permeability of cartilage by various methods. McCutchen applied an 1 atm pressure difference across cylindrical plugs of cartilage and found that the permeability normal to the surface was 5.8×10^{-16} m^2/Pa sec [58]. Maroudas *et al* examined the permeability of human femoral condylar cartilage and found that the permeability decreased with depth from the articular surface [53]. She later found that this decrease corresponds with the observed increase in fixed charge density with depth [51]. Mansour and Mow [47] and later Mow and Lai [41, 68] also measured the permeability of cartilage by a pressure driven flow, but at various pre-compressed strains. They found that the permeability decreases with increasing compressive strain and ranged between 2×10^{-16} and 2×10^{-15} m^2/Pa sec. This is consistent with Maroudas' observations of permeability dependence on fixed charge density, since with compression, the fixed charge density increases while the permeability decreases. Since it has been established that the permeability of cartilage is strain dependent, the bulk property measured across an entire cartilage plug in the above studies is more appropriately referred to as apparent permeability. The actual permeability is a local property which varies across the tissue with the strain state because the pressure difference across the soft tissue gives rise to drag forces of the fluid on the solid matrix, creating a non-uniform compressive strain distribution across the tissue.

Nevertheless, the apparent permeability is useful to characterize the creeping response of cartilage under load. Aside from pressure driven flow, others have used the mechanical response of cartilage to calculate its apparent permeability. Frank and Grodzinsky [23] applied the laws for linear electrokinetic transduction in ionized media with the principles of the linear (constant permeability) biphasic theory of Mow [67]. They calculated an apparent permeability of 3×10^{-15} m^2/Pa sec for adult bovine femoropatellar articular cartilage under cyclical loading. Mow *et al* also applied the linear biphasic theory to indentation creep experiments to calculate the apparent permeability of young bovine articular cartilage. They

found that the apparent permeability of femoropatellar cartilage (1.42 x 10^{-15} m^2/Pa sec) to be several times higher than of femoral condylar cartilage (4.4 x 10^{-16} m^2/Pa sec). In addition, Athanasiou later used the same indentation experimental technique and biphasic model to show significant interspecies and site difference in apparent permeability of articular cartilage. Thus, our apparent permeabilities (k_{comp} = 4.08 ± 0.78 x 10^{-16} m^2/Pa sec and k_{imb} = 3.42 ± 0.57 x 10^{-16} m^2/Pa sec), calculated from the linear analytic model fit to the compression and imbibing creep data on bovine femoral condylar articular cartilage, are consistent with previous studies.

As stated above, it has been shown that the actual permeability is a function of the compressive strain. Also the fact that our linear model, when fit to the creep data, requires two different permeabilities for compression and imbibing, suggests that one constant permeability is insufficient to describe the poroelastic response of cartilage to various load conditions. Mow *et al* have incorporated a non-linear strain dependent permeability function, based on their pressure driven apparent permeability measurements, under various pre-compressed states, to develop a non-linear continuum model which can simulate the creep and stress-relaxation behavior of cartilage under confined consolidation [67]. However this model has only been shown to simulate compression conditions, and it is unknown whether a strain dependent permeability function could account for the imbibing and compression differences seen with the creep responses measured in our study.

Various strain dependent permeability functions were incorporated into the linear LPM to investigate this possibility. Initially the permeability was described as a linear function between a low permeability (k_l = 3.18 x 10^{-16} m^2/Pa sec) at the end of compression (ε_c = 0.20 compressive strain) and a high permeability (k_h = 5.80 x 10^{-16} m^2/Pa sec) at the end of imbibing (ε_i = 0.12 compressive strain), where:

$$k(\varepsilon) = \frac{(\varepsilon_c - \varepsilon)}{(\varepsilon_c - \varepsilon_i)}(k_h - k_l) + k_l$$

$$\text{and } R_i(\varepsilon) = \frac{h}{nk(\varepsilon)} \text{ where } \varepsilon = \frac{x_i - x_{i+1}}{h/n} \text{ in LPM (Eqn 3.10)} \qquad (3.18)$$

as shown in Figure 3.18. Although Mow *et al* used an exponential function [67], this linear function is consistent with the apparent permeability measurements of Mow and Lai for the strain range in the experiments above [68]. The high and low permeability limits were chosen as those which would bracket the compression and imbibing creep data (for plug F) under a constant permeability assumption (Figure 3.19), and are consistent with the permeabilities

calculated by Mow for bovine femoral condylar cartilage [65].. Finally, it was found from the response of this non-linear strain dependent permeability LPM (Figure 3.20), that the linear permeability function cannot account for the imbibing and compression creep response differences experimentally observed. In fact, the difference in response predicted between these two conditions is reversed.

In addition to this linear permeability function, two additional exponential permeability functions were incorporated into the linear LPM (Figure 3.18):

$$\text{Exp \#1:}\quad k(\varepsilon) = (k_h - k_l)\left(e^{-6.0\frac{(\varepsilon-\varepsilon_i)}{(\varepsilon_c-\varepsilon_i)}} - 1\right) + k_h$$

$$\text{Exp \#2:}\quad k(\varepsilon) = (k_h - k_l)\left(1 - e^{6.0\frac{(\varepsilon-\varepsilon_c)}{(\varepsilon_c-\varepsilon_i)}}\right) + k_l \qquad (3.19)$$

$$\text{and } R_i(\varepsilon) = \frac{h}{nk(\varepsilon)} \text{ where } \varepsilon = \frac{x_i - x_{i+1}}{h/n} \text{ in LPM (Eqn 3.10)}$$

The creep responses predicted by these non-linear strain dependent permeability LPMs are shown in Figure 3.21. As the exponential permeability functions near that of constant permeability, at either k_h or k_l, the predicted creep responses move toward that predicted by the constant permeability function. In addition, the differences between imbibing and compression creep response become smaller, but they remain reversed relative to that experimentally observed .

Furthermore, the non-linear strain dependent permeability LPM was optimized with DOC/DOT to find the best fit possible final displacement, δ_f, permeability at end of imbibing, k_h, and permeability at end of compression, k_l, for each set of compression and imbibing creep measurements per plug. The results are tabulated in Table 3.2 and a typical model creep simulation is shown in Figure 3.22. As expected, the optimized model is that of a near constant permeability, because with any compression accompanying decrease in permeability, the imbibing creep becomes faster than the compression creep opposite to the experimental data. Thus, it is apparent that no reasonable consistent strain dependent permeability function alone could account for both the imbibing and compression creep responses observed experimentally.

Table 3.2 Permeabilities and Final Displacement from Least Squares Criterion Fit of the Non-Linear Strain Dependent Permeability Lumped Parameter Model to Experimental Creep Data.

Plug	Final Disp. δ_f [μm]	Permeability at End of Imbibing k x10^{15} [m^2/Pa sec]	Permeability at End of Comp. k x10^{15} [m^2/Pa sec]	Mean Error [μm]
F	104.3	0.385	0.381	1.7
G	111.6	0.515	0.514	1.5
H1	116.9	0.348	0.346	1.9
H2	114.9	0.354	0.352	1.8
J	126.4	0.345	0.343	4.6
K	102.9	0.307	0.304	3.6

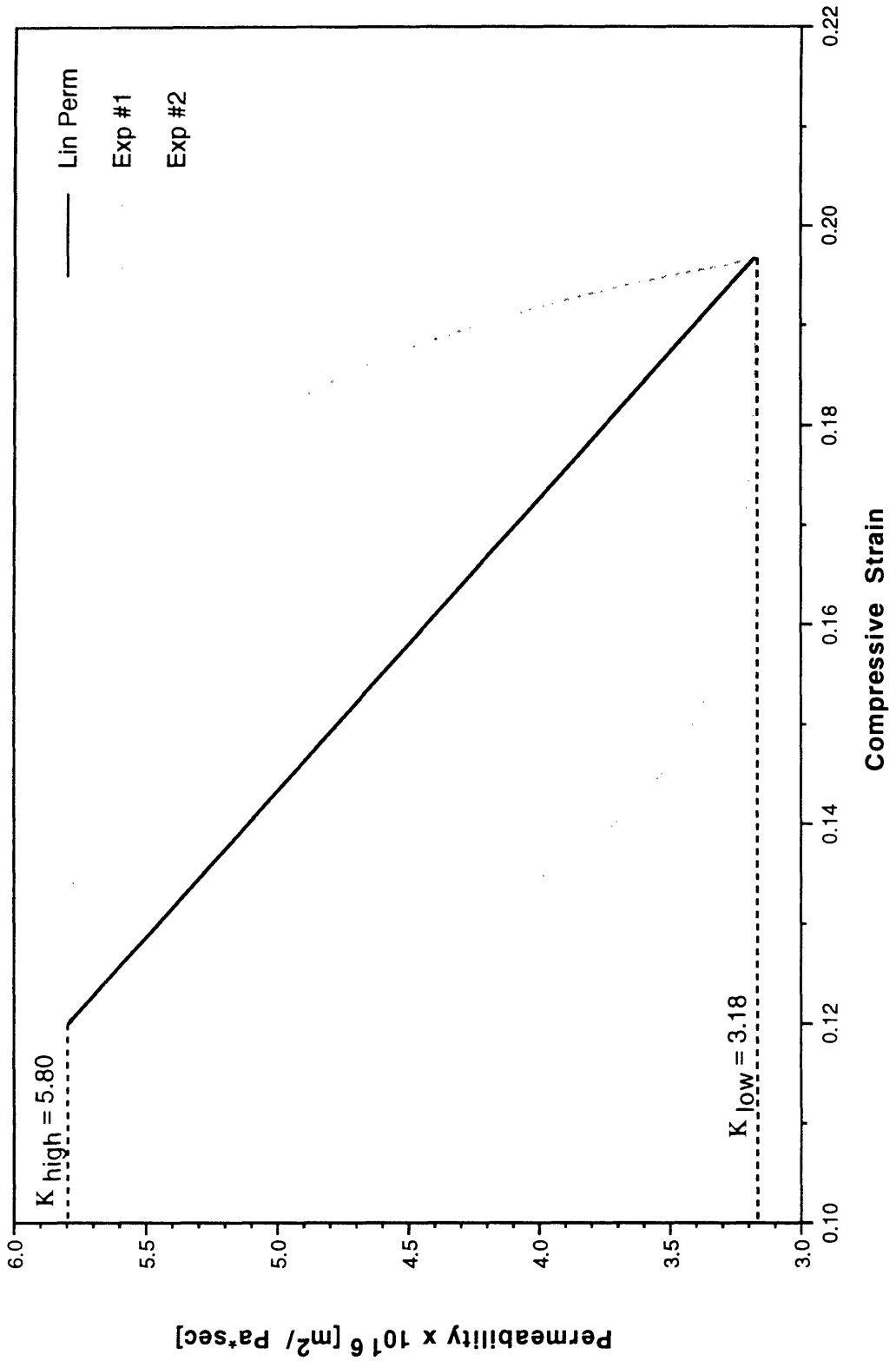

Figure 3.18 Strain Dependent Permeability Functions.

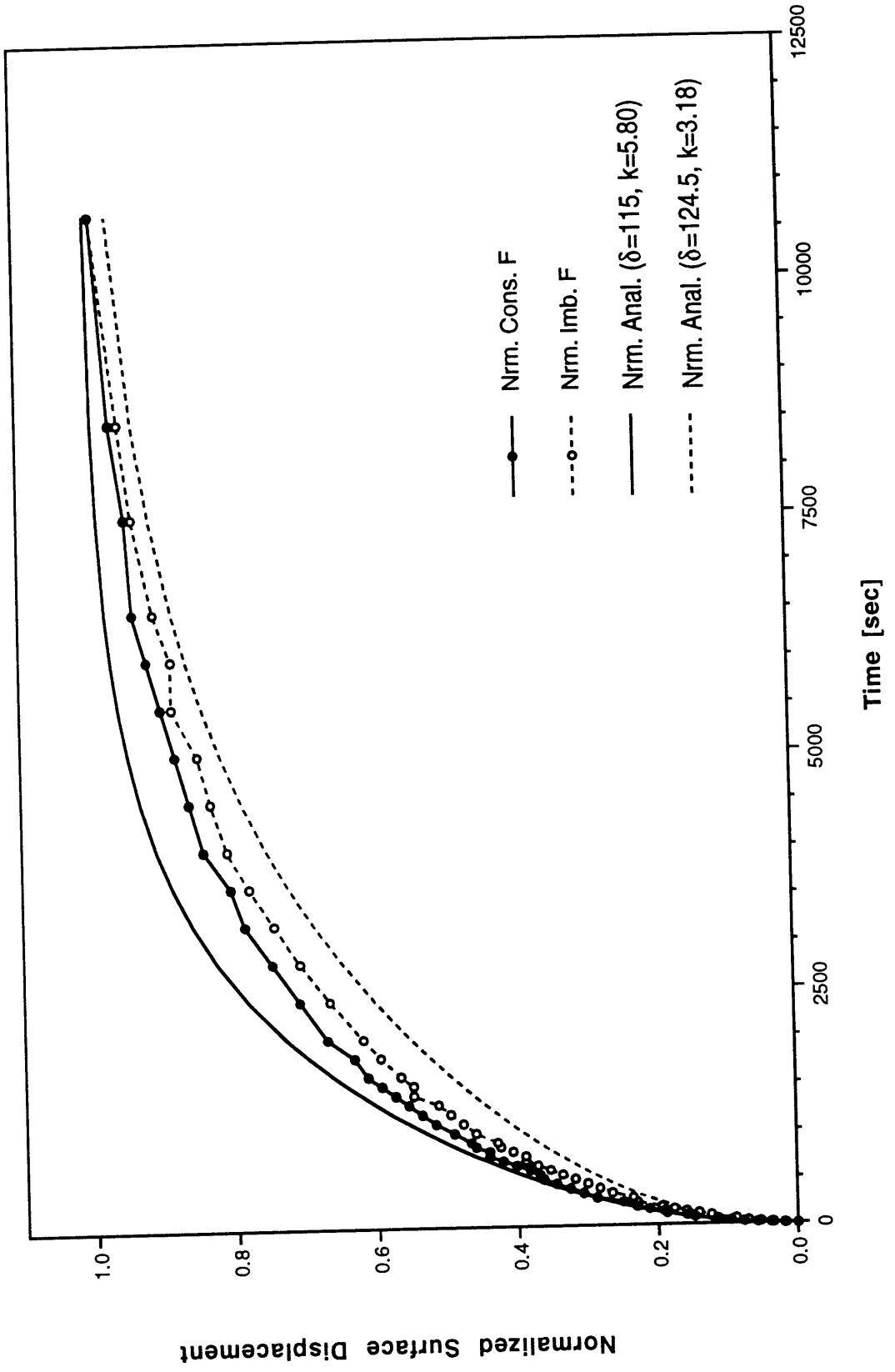

Figure 3.19 Linear LPM Creep Response for Bracketing Constant Permeabilities.

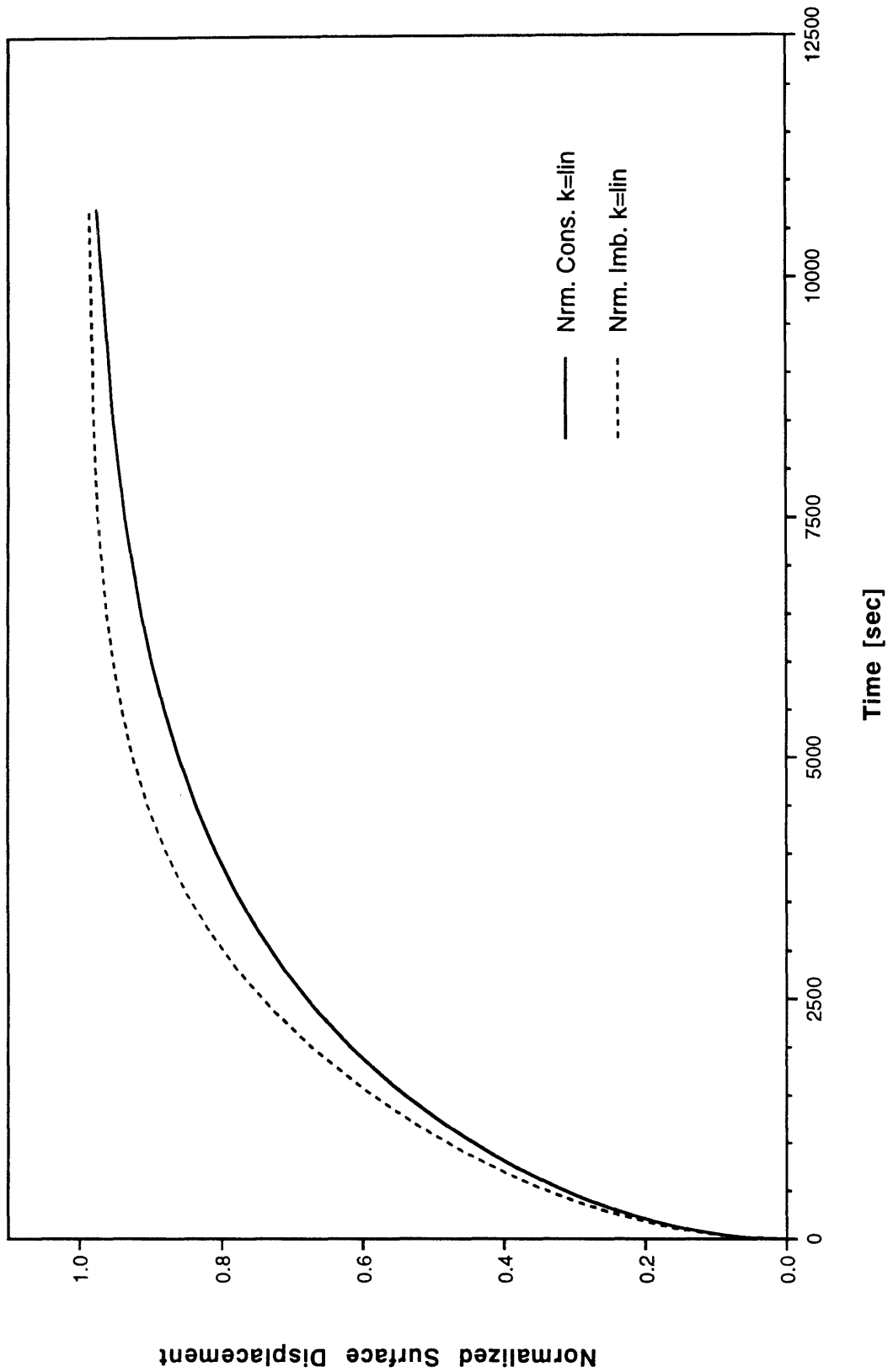

Figure 3.20 Creep Response of Non-Linear LPM with Linear Strain Dependent Permeability Function.

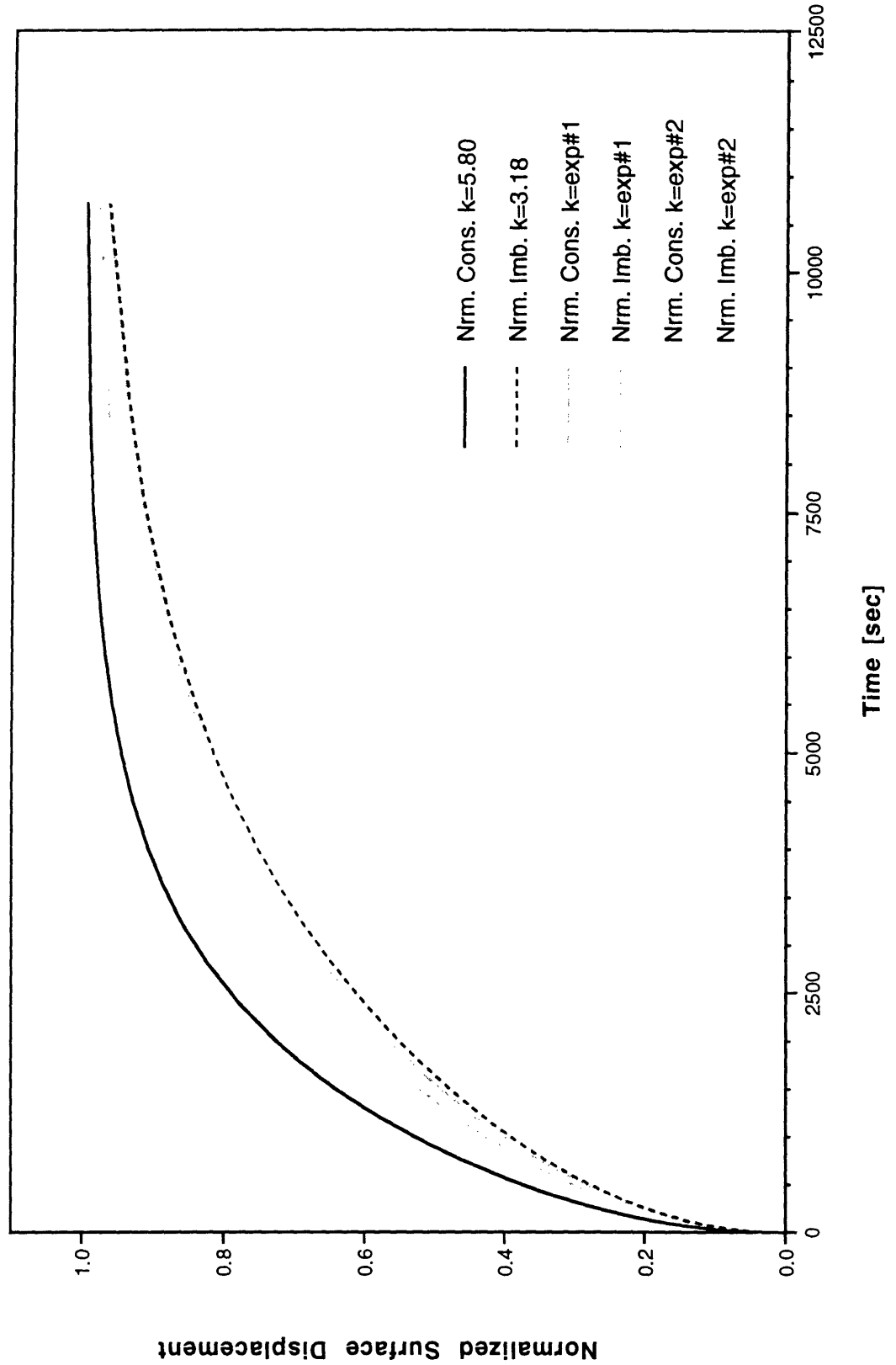

Figure 3.21 Creep Response of Non-Linear LPM with Two Exponential Strain Dependent Permeability Functions.

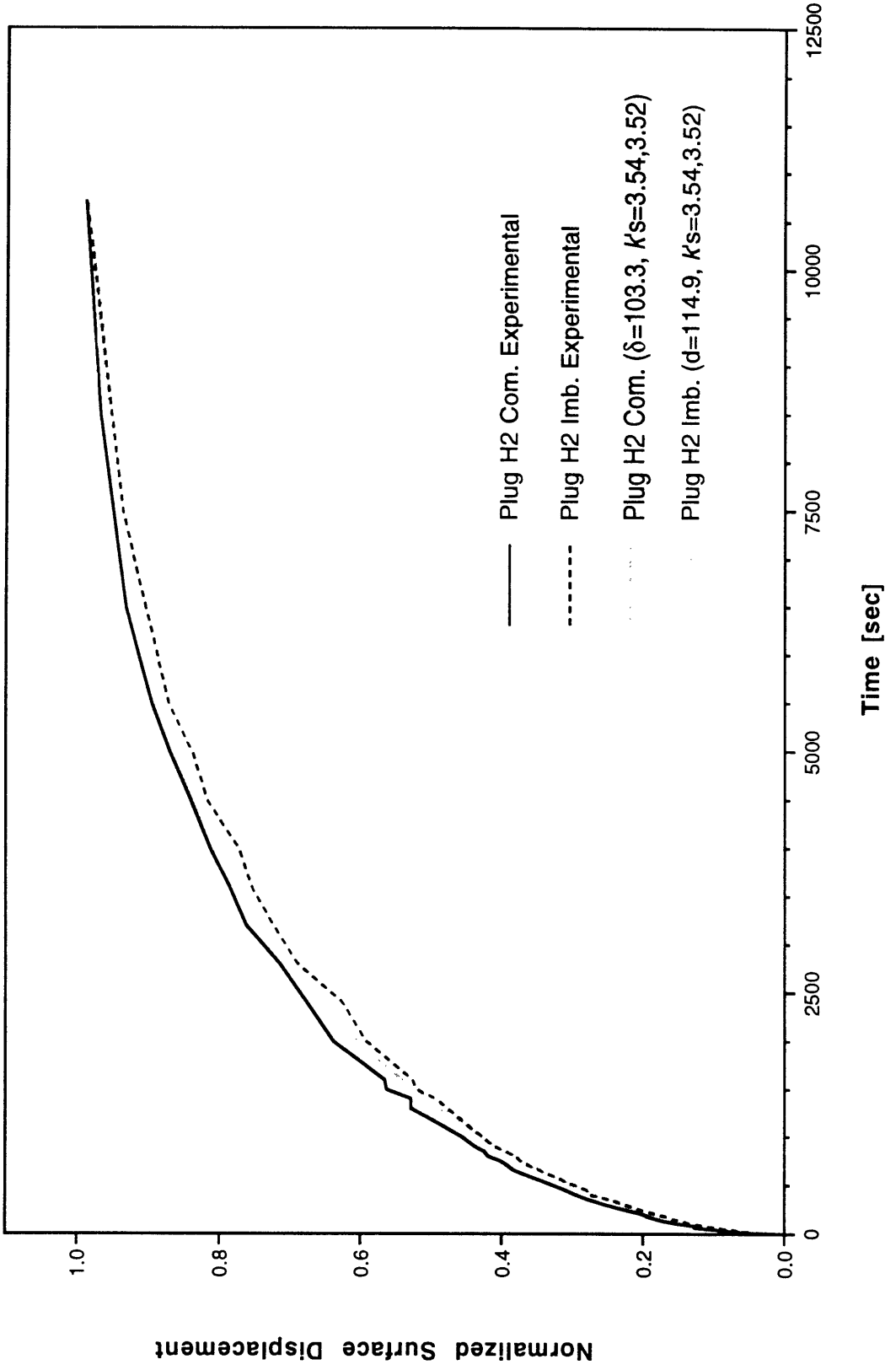

Figure 3.22 Optimized Strain Dependent Permeability Model and Experimental Creep Curves for Plug H2.

3.4.3 STRAIN DEPENDENT PERMEABILITY AND EQUILIBRIUM MODULUS

In an effort to find physical characteristics important for a consistent model which could predict both compression and imbibing creep responses, the assumption of constant equilibrium modulus (at low compressive strain) was re-examined (Figure 3.6). The original fit to the experimental stiffness data with a constant modulus for small compressive strains and then a strain dependent modulus for larger compressive strains was based upon previous similar treatments by other investigators. However, there was no experimental data which necessitated the assumption of constant stiffness at low compressive strains, and other functions are possible to model the entire strain range e.g. a third order polynomial function as shown in Figure 3.23.

A strain dependent non-linear stiffness was incorporated into the LPM in conjunction with the linear strain dependent permeability function described by Eqn 3.18. Because 1) the experimental measurements of stiffness were conducted with only two plugs and show a high variance, and 2) the interplug variance in the confined consolidation responses are large and the plugs for stiffness and creep measurements were harvested from different animals, a general hyperbolic stiffness function (described by two parameters) was incorporated into the LPM rather than the fixed third order polynomial function fit to the experimental stiffness measurements:

$$L(\varepsilon_c) = L_o \frac{\varepsilon_f}{\varepsilon_f - \varepsilon_c} \tag{3.20}$$

where; $L(\varepsilon_C)$ is the compressive strain dependent equilibrium modulus, L_O is the stiffness at zero strain, ε_f is the maximum compressive strain. A typical stress-strain curve for such a hyperbolic stiffness function is shown in Figure 3.24. Although $L \rightarrow \infty$ as $\varepsilon_C \rightarrow \varepsilon_f$, in physiological states, $\varepsilon_C << \varepsilon_f$, and within the strain range of interest, this function does describe the stiffness characteristics measured.

The strain dependent modulus function was applied to the model as:

$$K_i(\varepsilon) = \frac{nL(\varepsilon)}{h} \text{ where } \varepsilon = \frac{x_i - x_{i+1}}{h/n} \text{ in LPM (Eqn 3.10) and } L(\varepsilon) \text{ (Eqn 3.20)} \tag{3.21}$$

and the high and low permeability limits were taken to be those fit from the linear analytic model in Table 3.1. DOC/DOT was used to find the best fit final displacement, δ_f, stiffness at

zero strain, L_O, and maximum compressive strain, ε_f, for each set of compression and imbibing creep measurements per plug. The results are tabulated in Table 3.3 and a typical optimized parameter value model simulation of creep is shown in Figure 3.25, and the resulting stiffness function is shown in Figure 3.26.

Table 3.3 Permeabilities and Final Displacement from Least Squares Criterion Fit of the Non-Linear Strain Dependent Stiffness and Permeability Lumped Parameter Model to Experimental Creep Data.

Plug	Final Disp. δ_f [μm]	Stiffness at Zero Strain, L_O [MPa]	Maximum Comp. Strain, ε_f	Mean Error [μm]
F	104.5	0.400	0.521	1.2
G	111.9	0.734	0.800	1.6
H1	117.8	1.20	0.524	1.3
H2	115.6	1.05	0.500	1.6
J	105.5	0.29	0.400	1.5
K	105.5	0.29	0.527	1.5

With both strain dependent permeability and equilibrium modulus, a consistent fit to both creep responses with one set of parameter values is achieved. The model simulates a faster compression creep than imbibing creep with a permeability that decreases with increasing compressive strain and an equilibrium modulus that increases with increasing compressive strain. Also the fit of this model is as good or better than only the strain dependent permeability model (as measured by the mean error between model and experimental data). Although the optimized stiffness function has a wide variance for the modulus at zero strain, L_O, this may be a result of the hyperbolic stiffness function chosen for optimization. The actual stiffness function may be more complex (e.g. a third order polynomial), resulting in a narrower variance in the parameter values, but it would have been difficult to fit more parameter values with the number of plugs experimentally tested. Since the interplug difference in the experimental measurements are themselves large, the variance in the parameter values are not unexpected. Although, this hyperbolic stiffness function may not be the best, it is sufficient to demonstrate the necessity of a non-linear strain dependent equilibrium modulus for a consistent model of cartilage mechanical response.

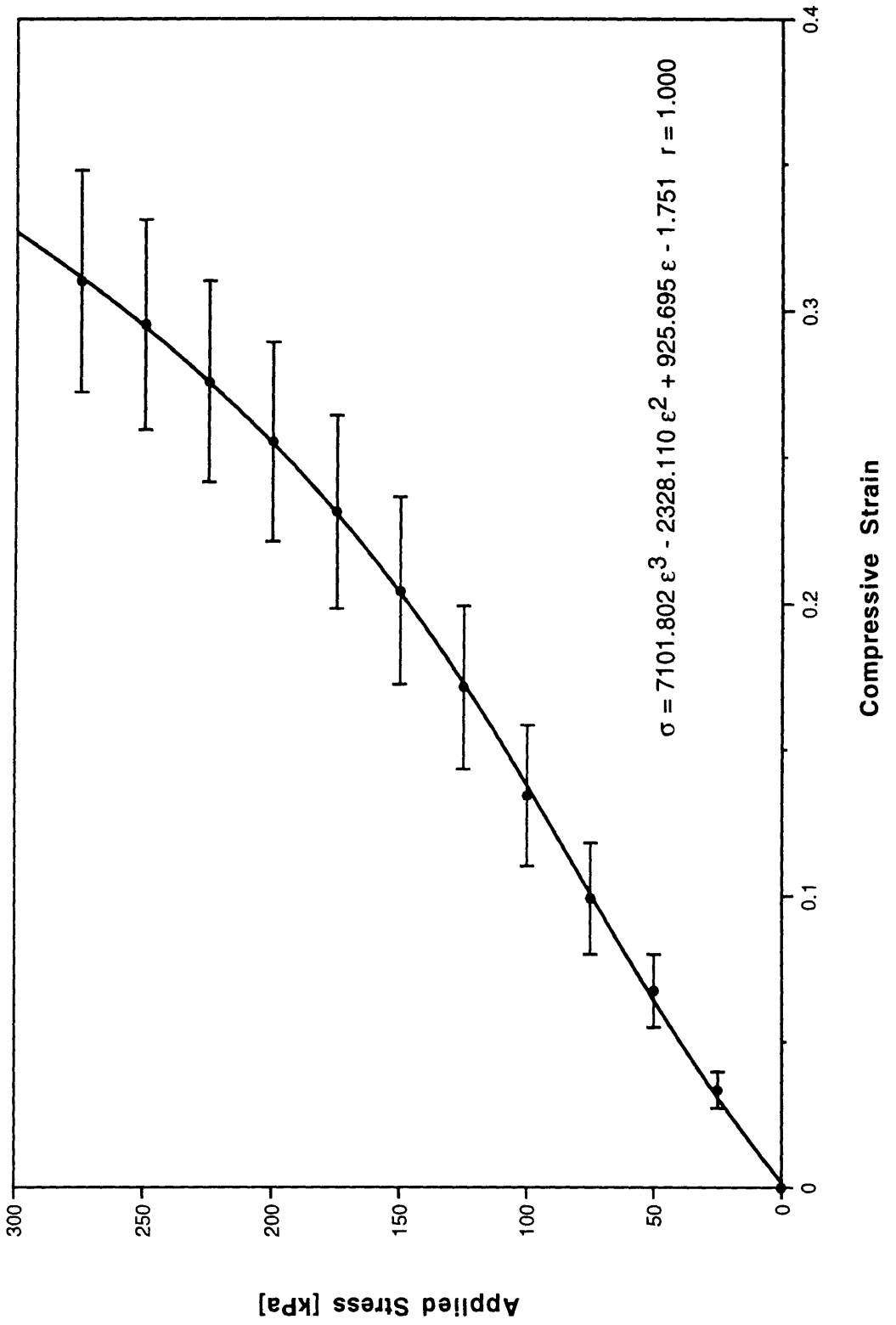

Figure 3.23 Re-examined Stiffness of 3-month-old Bovine Articular Cartilage in Confined Consolidation.

Massachusetts Institute of Technology

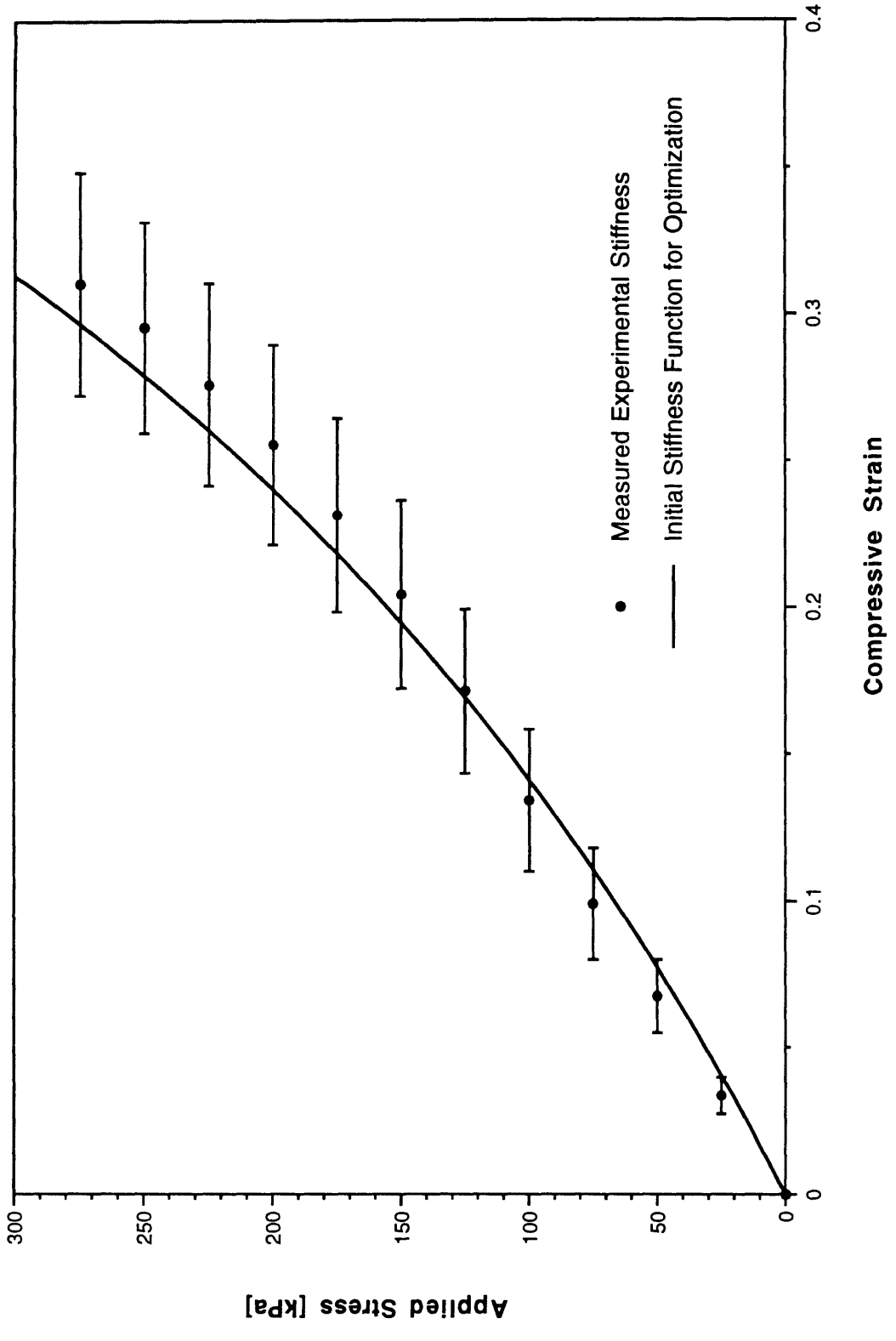

Figure 3.24 Typical Hyperbolic Stiffness Function for 3-month-old Bovine Articular Cartilage in Confined Consolidation.

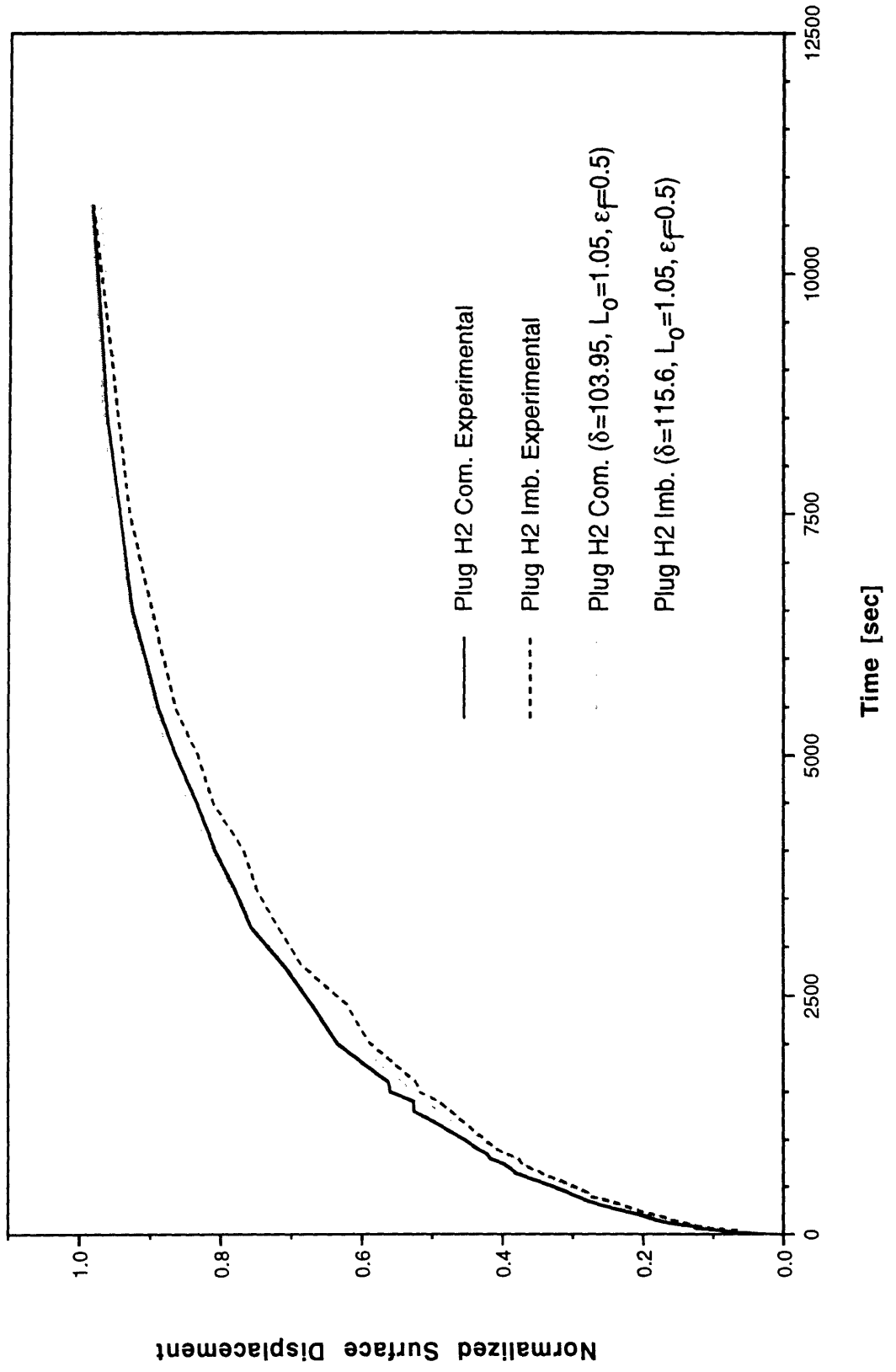

Figure 3.25 Optimized Strain Dependent Stiffness and Permeability Model and Experimental Creep Curves for Plug H2.

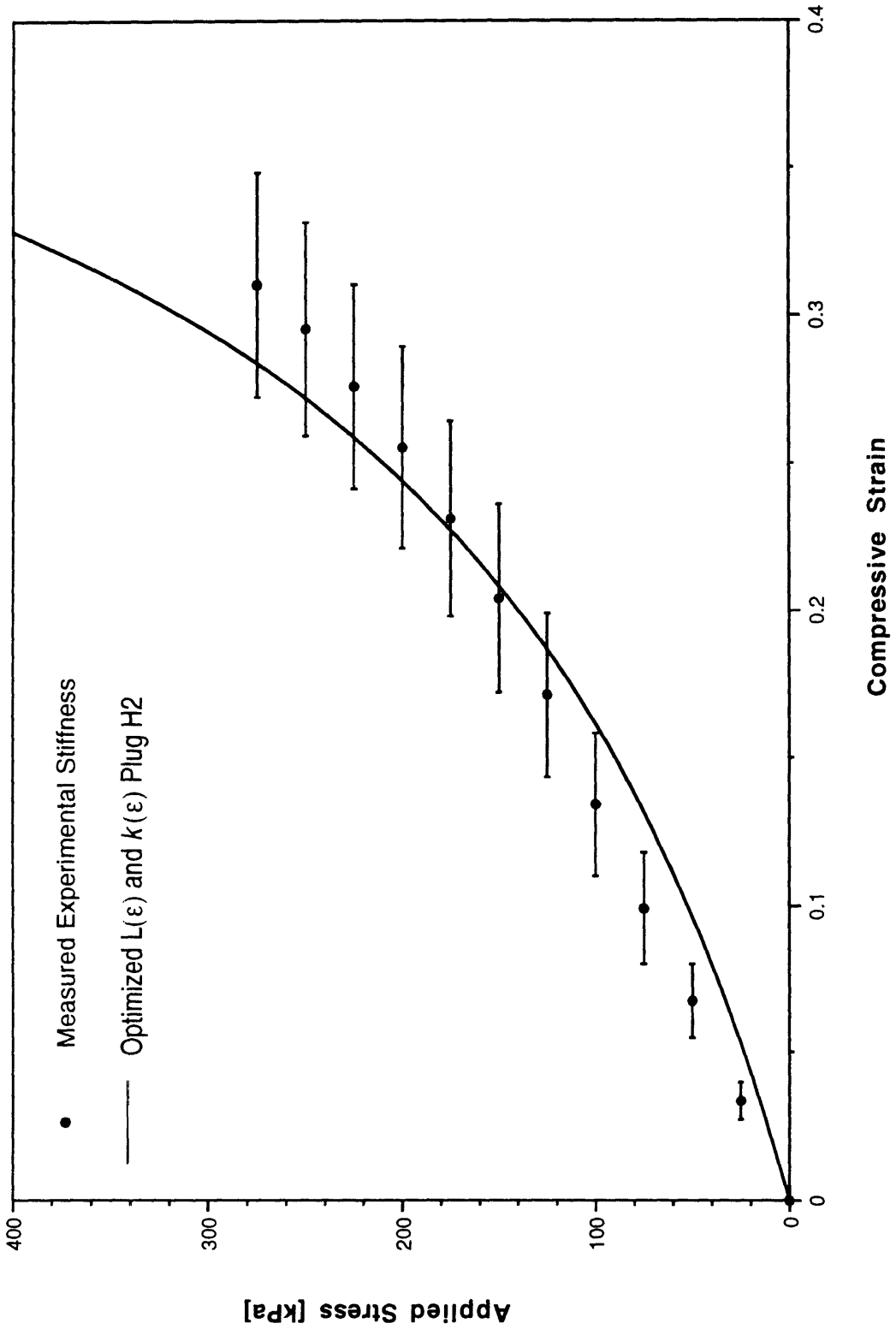

Figure 3.26 Optimized Hyperbolic Stiffness Function for Plug H2 and Experimental Stiffness Measurements of 3-month-old Bovine Articular Cartilage in Confined Consolidation.

3.5 CONCLUSION

Unique high resolution experimental creep consolidation of cartilage in both compression and imbibing modes were compared to various physical models of cartilage. The significant physical characteristics of cartilage were determined by comparison of models to both the compression and imbibing creep responses. The general response of cartilage was found to be well modeled by the simple linear gel diffusion theory model (analytic or LPM). It is easily implemented and can be used to calculate a constant apparent permeability from creep experimental data consistent with those predicted by other means. However, the constant permeabilities calculated from the linear model demonstrate the non-linear permeability of cartilage. Since two different constant permeabilities are required to model both the compression and imbibing creep behavior, and there are no known differences in physical interaction of the ECM components for these two creep situations, one constant permeability is insufficient to describe the poroelastic response of cartilage.

Since it has been shown by other investigators that the actual local permeability is a function of the strain state, strain dependent permeability was incorporated into the lumped parameter model. Various strain dependent permeability functions, consistent with those used by other investigators, were simulated and found to correctly model the compression or imbibing creep behavior, but not both. Regardless of the permeability function, strain dependent permeability alone (decreasing permeability with increasing compressive strain) could not account for the imbibing and compression creep behavior differences observed experimentally. Furthermore, models with strain dependent permeability alone predicted creep response differences opposite to that experimentally observed.

Finally, the assumption of a constant equilibrium modulus at low compressive strain levels was re-examined. No experimental evidence was found in the stiffness measurements which necessitated a linear regime and other non-linear stiffness functions were shown to describe the entire range of compressive strains. A linear strain dependent permeability function and a hyperbolic strain dependent equilibrium modulus was incorporated into the linear lumped parameter model and the parameter values for the stiffness function was optimized to match the experimental creep data for both imbibing and compression. It was found that this model correctly simulates the poroelastic creep response of cartilage and also those differences between compression and imbibing creep experimentally observed.

There was a wide variance of the modulus at zero strain, L_O, in the optimized stiffness function, and this was thought to be a result of the simple hyperbolic stiffness function chosen for optimization. The actual stiffness function may be more complex, and the assumption of a simple hyperbolic function probably resulted in this wide variance. Furthermore, since the interplug difference in the experimental measurements are themselves large, the variance in the parameter values were not unexpected. Nevertheless, this hyperbolic stiffness function is sufficient to demonstrate the necessity of a non-linear strain dependent equilibrium modulus for a consistent model of cartilage mechanical response. For a more complete model with strain dependent modulus and permeability, more stiffness and creep response measurements are required on the same plugs.

The velocity dependent permeability, for which these consolidation studies were conducted, were not observable in the experimentally measured creep responses. Since the optimized lumped parameter model with k (ε) & L (ε) compared to the experimental data has a mean error of only 1.45 ± 0.16 μm and the resolution of the experimental measurements are only 2.0 μm, it was not possible to determine with this set of experimental data if there was any decrease in permeability with increased interstitial fluid velocity. For this determination, some other method is required. Although no evidence for channel formation was observed, this does not signify their impossibility and channels may still form under physiological conditions.

CHAPTER
FOUR

LOOSE COLLAGEN FIBRIL ISOLATION

4.1 DRAG INDUCED ORIENTATION

The movement of a long axisymmetric body through a viscous fluid has been described and analyzed by Taylor [92]. Whereas it had been known that the resistance of a very long prolate spheroid moving in a viscous fluid is twice as great when moving in the direction normal to the long axis as it is when moving along this axis, Taylor generalized this result for all long axisymmetric bodies provided the center of gravity is in such a position that the body can remain horizontal while falling. With this condition satisfied, the body will not change its initial orientation and will move along a straight path which forms an acute angle of 19.5°or less with respect to the direction of the body force (for detailed discussion see Happel and Brenner [25]).

Interaction between linear polymers and hyaluronate macromolecules has been the subject of a study by Laurent *et al* [43]. They have shown that diffusion of linear polymers in hyaluronate solutions is retarded, but to a lesser degree than expected from their equivalent hydrodynamic radius (i.e. the presence of hyaluronate retards diffusion of linear polymers less than it does of globular polymersof equal MW). In view of diffusion treatment by Ogston *et al* [75], the difference is attributed to end-on movement of linear polymers through the hyaluronate network.

Our study has been motivated by this basic realization that stiff, short fibers can be oriented by movement relative to a finer, three-dimensional, isotropic network. Such networks typically exist in gels. While a true gel is a colloidal system in which the network junctions are of infinite duration, and thus give the gel a non-zero equilibrium shear modulus, the orientation mechanism proposed herein is satisfied by a wider class of gel-like substances exemplified by dispersions of large proteoglycan molecules, or entangled three-dimensional networks of polymer chains (e.g. hyaluronate solutions). The network junctions may be of finite duration, i.e. network relaxation time constant should be greater than the characteristic time constant of the body force on the fiber. The fiber length must be at least a few times the average network opening, and the body force on the fiber must be high enough to allow for the piercing of the network by the fiber. In addition, the bending stiffness of the fiber must be sufficient to limit its deformation when loaded by the driving force against the network.

Movement of a short wire segment through a soft gel can be used for a simple demonstration of the orientation mechanism. A 1% gelatin solution is prepared by dissolving gelatin in water at about 70°C and poured into a large test tube (about 600 ml). Another tube of equal size is filled with glycerin. A small piece of stainless steel wire (0.6 mm diameter, about 12 mm long) is placed in each tube and the tops are sealed without entrapping air (best done with a rubber membrane to allow for volume changes of the gel due to temperature variations). At the temperature of 25°C the gelatin will gel to appropriate stiffness in about two days. The tubes are then repeatedly inverted and descent of the wires is observed. The speed is approximately the same in both cases, but the wire orientation differs. In glycerin the wire retains its starting orientation (horizontal if starting off the flat tube end) - in gelatin it quickly assumes a vertical orientation.

Figure 4.1 illustrates the forces acting on, and the resulting movement of, a fiber through an elastic/viscous medium. The elastic network of the medium is depicted by its nodes. Force F is the resultant body force on the fiber, inclined from the normal to the fiber by an angle α - components of F normal and parallel to the fiber are denoted as F_n and F_t respectively. Force F_n is balanced by elastic stresses in the network. If F_t exceeds the piercing force F_p, the fiber will move, driven by the force F_t-F_p. As the fiber advances into a less strained area of the network the balance of forces will be disturbed. Movement of the fiber out of the strained network at the rear, and threading into a less strained network at the front, produces a net moment, tilting the fiber, as indicated by its next few positions in Figure 4.1. The components F_n and F_t will change as well: F_n decreasing, F_t increasing. The fiber will turn and accelerate until the piercing force F_p and the viscous drag induced in the dispersing fluid

balance the force F_t (ultimately F). The fiber will then continue moving at a constant speed, oriented parallel to its trajectory (and force F).

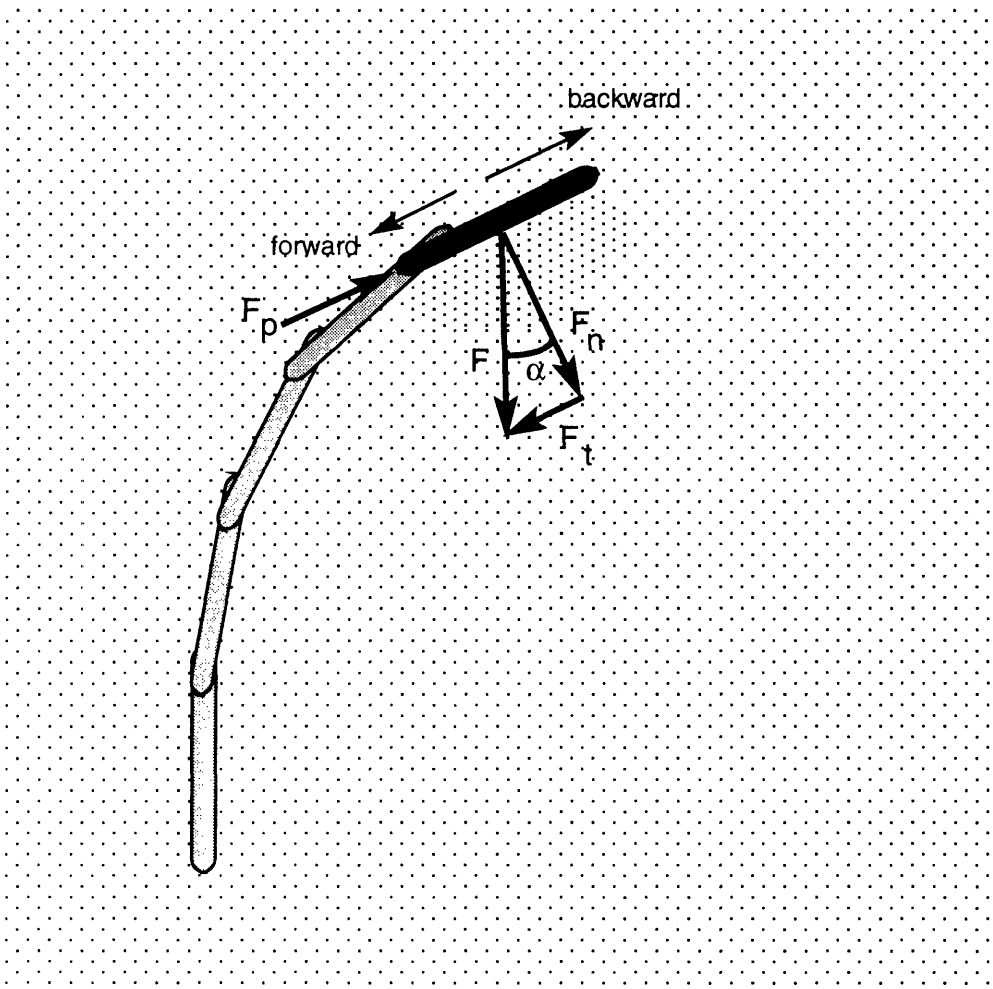

Figure 4.1 Progression of a fiber driven by forces through a poroelastic medium.

The process described is believed relevant to orientation of extracellular matrices, in particular, collagen networks. Collagen fibrils are assembled in the near surround of the cells that synthesize collagen. The fibrils are then incorporated into the collagen network. To generate and maintain the network orientation in the face of disturbances, the fibrils must orient before integration into the network. The fibrils are dispersed within a gel-like medium - in these matrices, proteoglycans are ubiquitous and form an entangled, molecular scale network. The force to move the fibrils may be generated by the viscous drag of the fluid moving through the molecular (proteoglycan) network which is immobilized by the extant

collagen network. This fluid flow would be driven by activities of the tissue on the macro scale. Thus a fine, three-dimensional, PG network and the conditions of fibril movement through it may give rise to orientation of the coarse collagen network in the process of assembly.

4.2 ISOLATION OF LOOSE COLLAGEN FIBRILS

4.2.1 INTRODUCTION

Many of the investigations concerning morphology of growing collagen fibrils have been conducted using *in vitro* fibrillogenesis models. Despite similarities to fibrils formed *in vitro*, *in vivo* fibrillogenesis is recognized as considerably more complex. *In vitro* fibrillogenesis is conducted with solutions of collagen molecules extracted from tissues, and hence in the absence of macromolecular components present in the ECM (i.e. other minor collagen types, PGs, glycoproteins, etc.). Also solutions of collagen molecules are usually polydisperse systems containing a variety of aggregate units, whereas evidence suggests that collagen molecules may be secreted as a high concentration of Segment Long Spacing-like (SLS) aggregate units [10]. Thus, aggregation, concentration, and environment may all differ between *in vitro* and *in vivo* conditions.

Rather than infer that *in vitro* results characterize loose growing collagen fibrils, isolation of loose fibrils assembled in the ECM before incorporation into the extant collagen network was attempted. The drag induced orientation hypothesis proposes that these loose collagen fibrils are dragged relative to the PG network, thus becoming oriented. If the tissue could be irrigated with an isotonic buffer over a prolonged period of time, then these loose collagen fibrils could be collected in the irrigation fluid. To further increase the yield of these fibrils, PGs of neonatal or near neonatal fetal articular cartilage, with a high turnover rate of collagen, were partially digested using the protocol developed by Chun *et al* [14] , and irrigation was conducted at slightly higher than physiological flow rates (Section 5.4.1).

4.2.2. MATERIALS AND METHOD

Cartilage Tissue Preparation

Bilateral intact hind limbs of full-term bovine fetuses were sealed, frozen (uncontrolled), and stored at -20°C, within hours of maternal sacrifice at the Zürich slaughterhouse. After thawing ~12 hr at RT and ~12 hr at 4° C, Ø10.2 mm cartilage plugs (with subchondral bone)

were cored from the intertrochlear femoral surface under irrigation with sterile 0.9% PBS (with 100 I.U./ml penicillin and streptomycin, 0.2 mM PMSF, 20 mM EDTA, 5 mM benzamidine-HCl, and 5 mM NEM at ph 7.2, 4°C, standard). The plugs were kept in sterile 0.9% PBS at 4°C after coring, during sectioning and prior to PG digestion (3 hr). The plugs were then confined in a plexiglass holder (Figure 2.14), and sectioned to 2 mm uniform thick plugs as described in Section 2.3.1.

Proteoglycan Digestion

After rinsing with sterile 1% NaCl, the plugs were shaken dry and placed in 50 ml polycarbonate Sorvall centrifuge tubes (4 plugs per tube). Each tube was filled with 20 ml of sterile chondroitinase solution (0.125 I.U./ml of chondroitinase ABC in 0.05 M Tris HCl, 0.06 M Na-acetate, with 0.2 mM PMSF, 20 mM EDTA, 5 mM benzamidine-HCl, and 5 mM NEM at ph 8.0) and covered with parafilm. The tubes were shaken in a Kotterman water bath for 24 hr at 37°C and then again rinsed in sterile 1% NaCl before the next digestion The chondroitinase digestion media was stored at 4°C for later processing.

The plugs were then similarly digested with a sterile hyaluronidase solution (4 plugs per 20 ml of 5 I.U./ml streptomyces hyaluronidase in 0.05 M Na-acetate, 0.15 M NaCl, with 0.2 mM PMSF, 20 mM EDTA, 5 mM benzamidine-HCl, and 5 mM NEM at ph 6.0, in a 50 ml Sorvall tube). After digestion for 24 hr at 37°C, the plugs were rinsed in sterile 1% NaCl and stored in standard PBS at 4°C. The hyaluronidase digestion media was also stored at 4°C for later processing. In addition to plugs serially digested with both chondroitinase and hyaluronidase, some plugs were digested with only one enzymatic treatment, and controls were conducted with plugs treated in buffers corresponding to each digestion media.

Irrigation

Irrigated plugs were packed in a Merck Biochromatography Superformance, 50-10 High Pressure Liquid Chromatography (HPLC) System supported by a weaved polypropylene fiber disk with an underlying Ø10 x 0.3 mm stainless steel sieve with Ø0.2 mm holes spaced 0.55 mm apart (Figure 4.2). Sterile standard 0.9% PBS at 4°C was pumped through the column (maintained with water jacket at 4°C) by a Merck LiChroGraph L-6000 HPLC pump, under flow control. Flow was started at 1 µl/min, increased 1 µl/min every hour to 3 µl/min, and then increased 1 µl/min every half hour to 10 µl/min. 40 ml of irrigation fluid was collected in a 50 ml polycarbonate Sorvall centrifuge tube, covered with parafilm, in 20 ml increments.

The irrigation fluid and digestion media were all centrifuged for 30 min @ 20,000 rpm and 5° C in a Sorvall RC5C centrifuge. The supernatant was then carefully poured off and the pellets resuspended in 10 µl, 0.2 M $NaHCO_3$ by vibration. Plugs digested with only one enzyme were not irrigated due to poor sealing within the chromatography column.

Transmission Electron Microscopy

Ø 3.0 mm 400 mesh copper grids were covered with a colodian film and spray coated with 5 nm of carbon. Immediately prior to use, the coated grids were plasma etched to reproduce initial hydrophilicity necessary for proper absorption. Then, 5 µl of the resuspended samples were loaded onto the carbon coated side of the grids, and allowed to absorb for 2 min prior to blotting dry with a piece of filter paper. The grids were then dipped in distilled water and blotted dry, three times consecutively. Finally, they were negatively stained with uranyl acetate for 2 min, blotted dry, and examined with a Hitachi 600 TEM, at 100 kV.

4.2.3 RESULTS

Few mature collagen fibrils, ≈ Ø40 nm of unknown length (larger than one field), with at least one tapered end were observed in the chondroitinase digestion media (Figure 4.3). No fibrils were observed with two tapered ends. The D-banding of the collagen fibril was readily observable, but in general the fields were often obscured by ubiquitous, large particles. Occasionally, a banded fiber was observed with drastically varying diameter (Figure 4.4). These fibrils had a diameter at one end which was almost 1/4 of that at the other end (Figures 4.5 and 4.6). The chondroitinase digestion control media also contained these mature collagen fibrils, but all of them had blunt ends (Figure 4.7). Often, the blunt ends are slightly flared with a frayed-like appearance (Figure 4.8). The chondroitinase digestion control media contained almost no large particles other than the mature collagen fibrils.

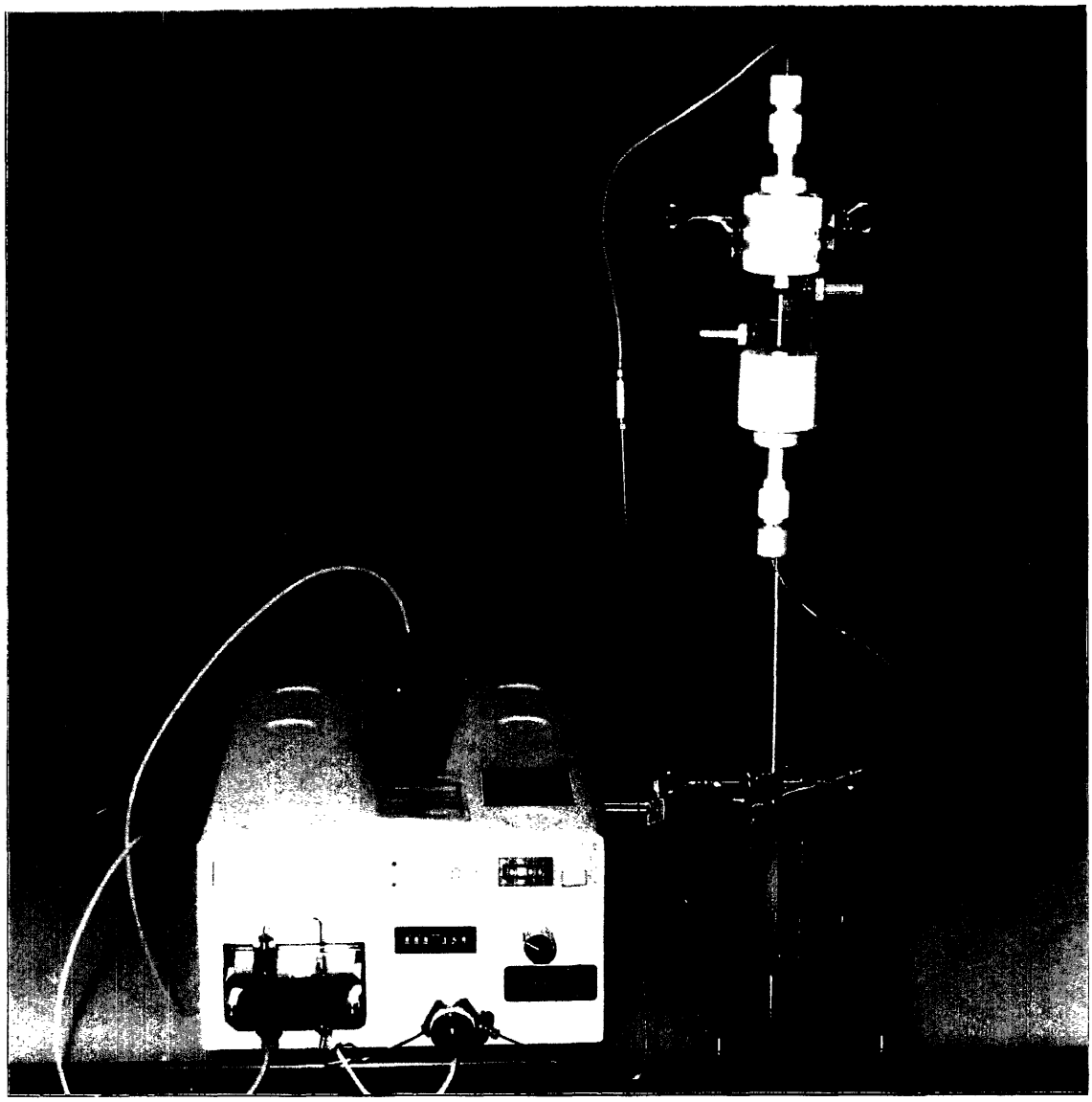

Figure 4.2 Articular Cartilage Plug Irrigation Apparatus.

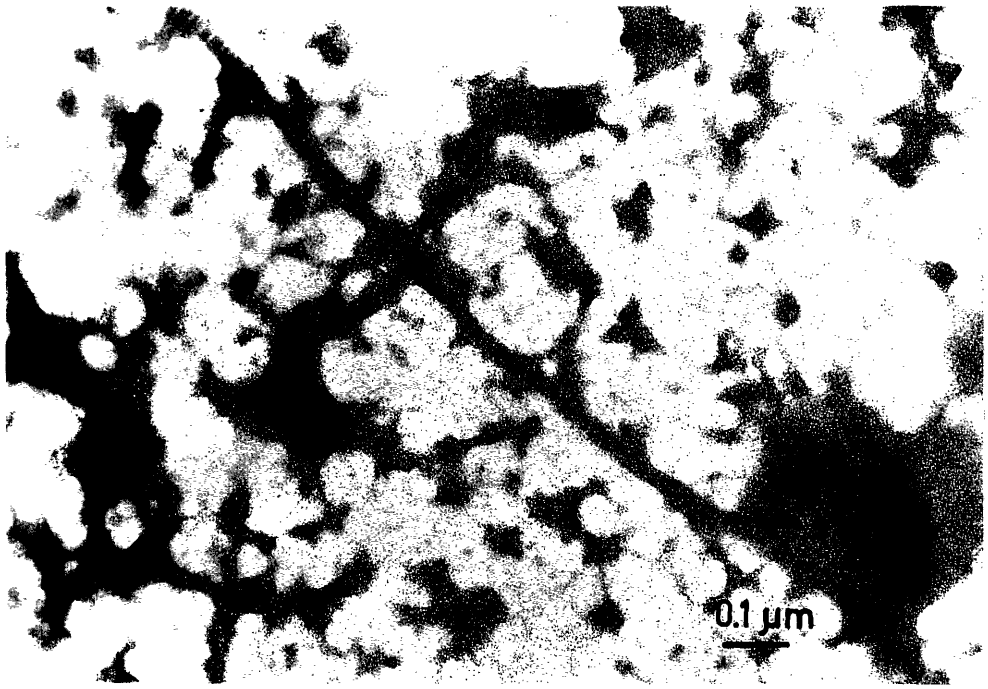

Figure 4.3 Electron micrograph of typical mature collagen fibril observed in the chondroitinase digestion media. Bar = 0.1 µm x 86,000.

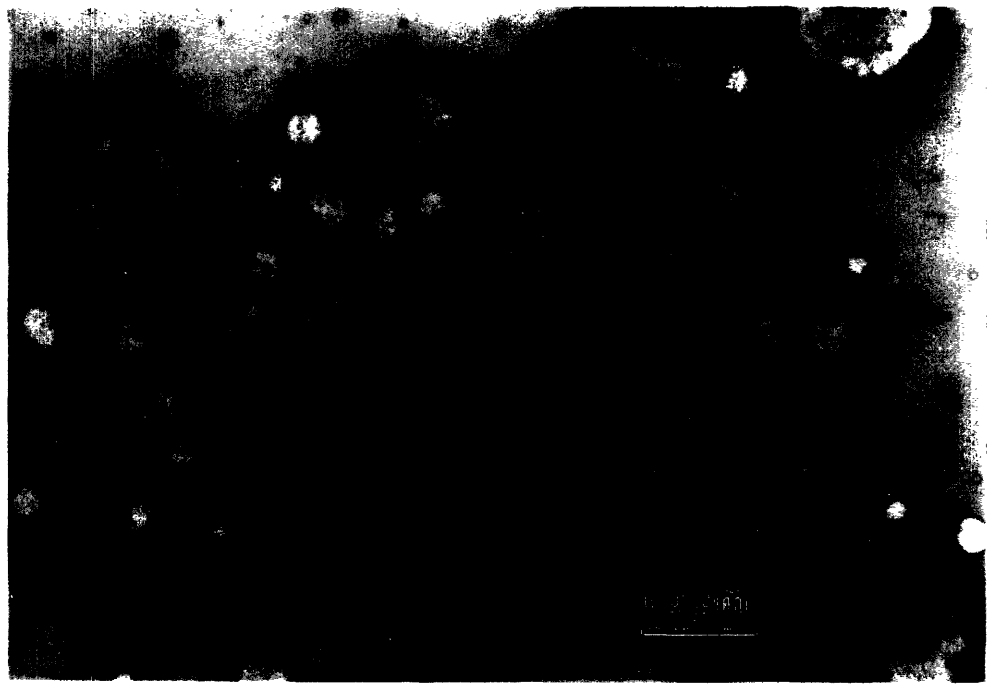

Figure 4.4 Electron micrograph of mature collagen fibril with drastically varying diameter observed in the chondroitinase digestion media. Bar = 1.0 µm x 15,000.

Figure 4.5 Electron micrograph of the small diameter end of the collagen fibril in Figure 4.4. Bar = 0.2 µm x 53,000.

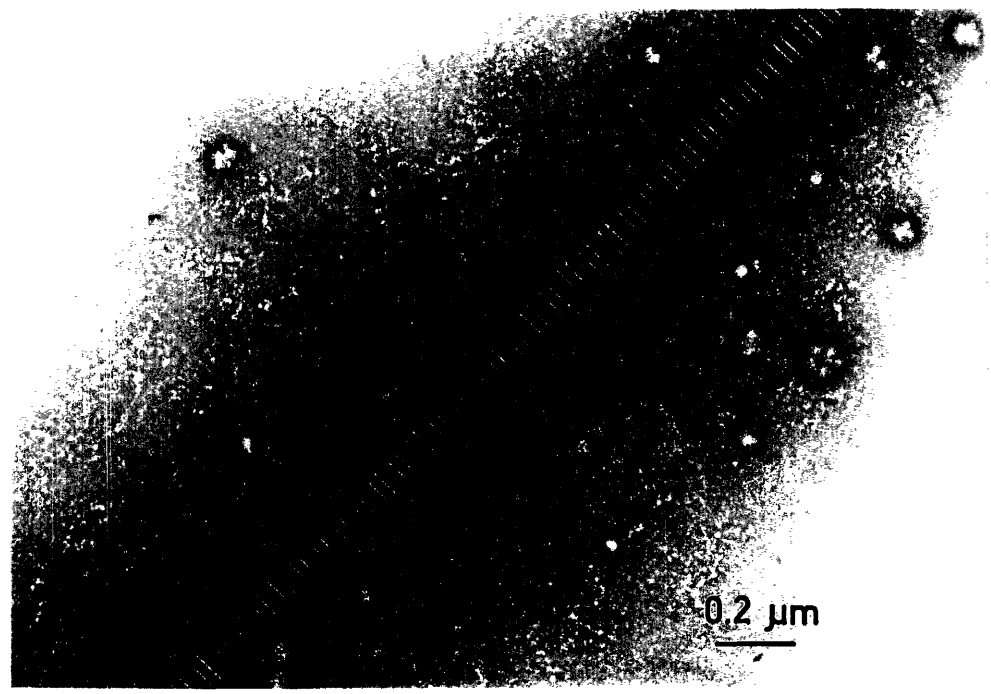

Figure 4.6 Electron micrograph of the large diameter end of the collagen fibril in Figure 4.4. Bar = 0.2 µm x 53,000.

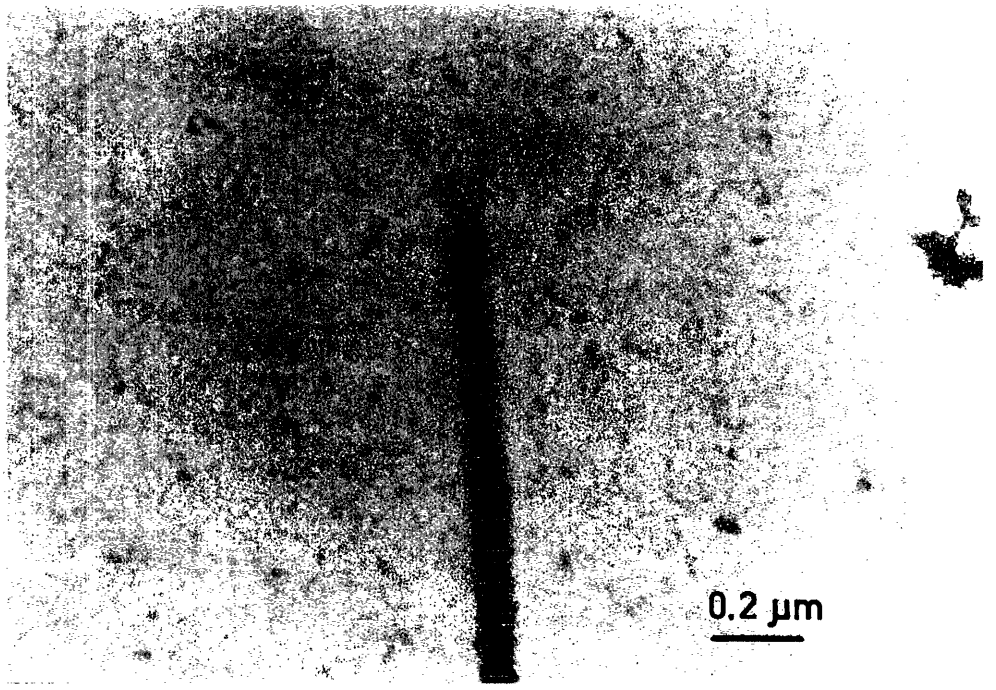

Figure 4.7 Electron micrograph of typical mature collagen fibril with blunt end observed in the chondroitinase digestion control media. Bar = 0.2 µm x 61,000.

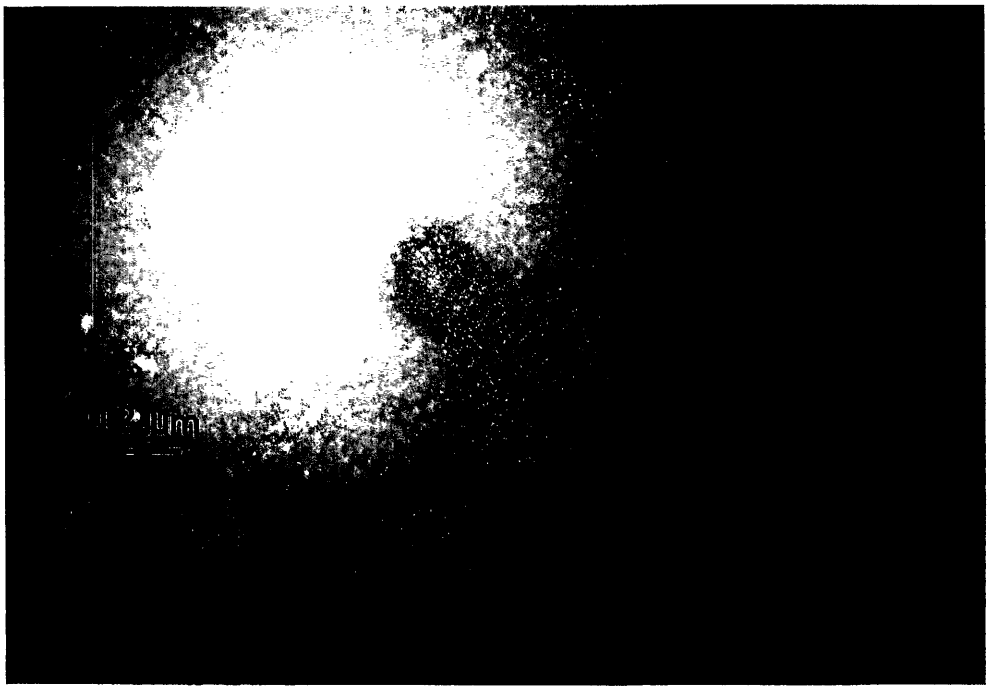

Figure 4.8 Electron micrograph of the slightly flared and almost frayed-like end of the collagen fibril in Figure 4.7. Bar = 0.2 µm x 61,000.

The hyaluronidase digestion media contained even fewer collagen fibrils than in the chondroitinase digestion media, but those observed were all ≈ Ø40 nm and almost all had at least one tapered end (Figure 4.9). Again, no fibrils were observed with two tapered ends. The tapered ends were more readily seen because of the absence of large obscuring particles (seen in the chondroitinase digestion media). Upon higher magnification, it is evident that the taper is smooth with respect to the fibril diameter (Figure 4.10). In addition to these tapered ends, few smaller aggregates of short banded fibrils were observed (Figure 4.11). No regular objects were evident in the hyaluronidase digestion control media.

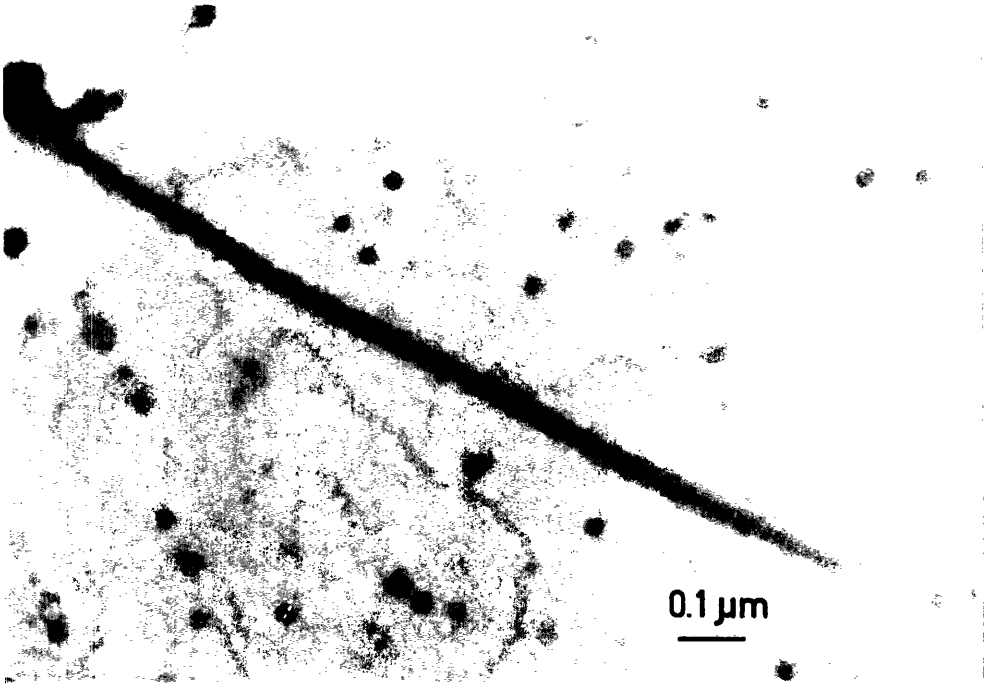

Figure 4.9 Electron micrograph of typical mature collagen fibril with tapered end observed in the hyaluronidase digestion media. Bar = 0.1 µm x 86,000.

In the first 20 ml of the collected irrigation fluid, mature banded fibrils of various diameter extended across many fields (Figure 4.12). These fibrils ranged in diameter from ≈ 20 to 60 nm, and when observable had both blunt or tapered ends (only one end observable). In addition to these banded fibrils, many unbanded filaments, Ø10.4 ± 0.5 nm x 1.06 ± 0.03 µm, were observed in every field (Figure 4.13). The second 20 ml of collected irrigation fluid contained no fibrous particles.

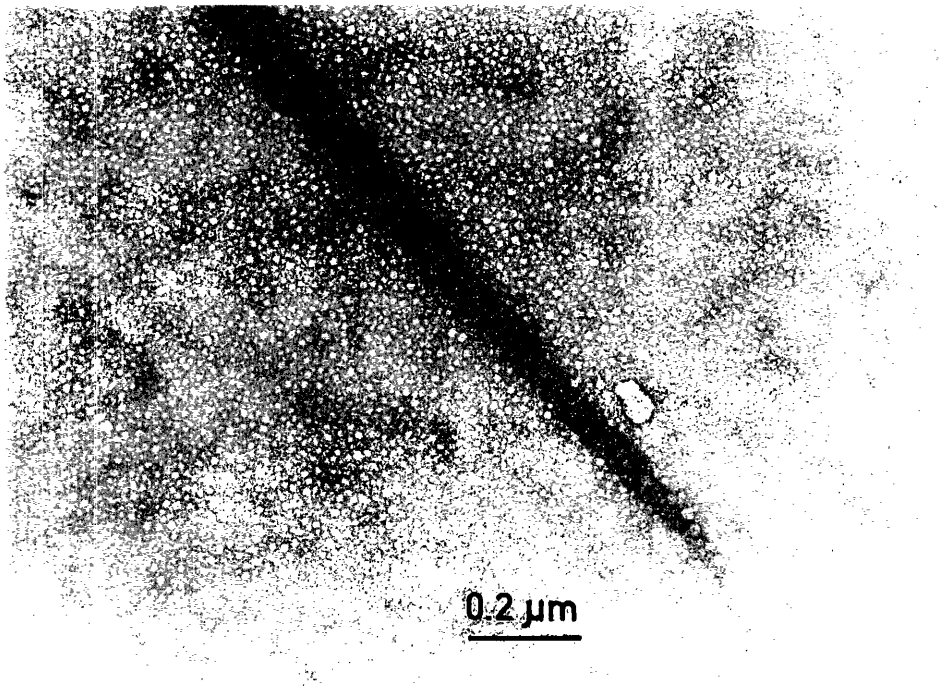

Figure 4.10 Electron micrograph of the "smooth" tapered end of the collagen fibril in Figure 4.9. Bar = 0.2 µm x 76,000.

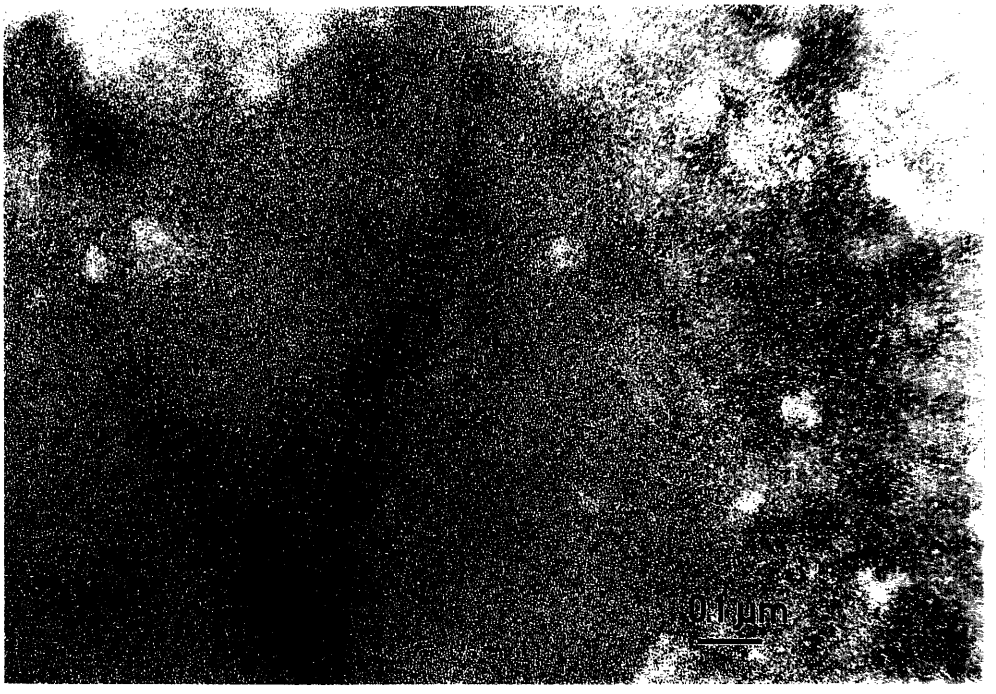

Figure 4.11 Electron micrograph of typical short banded fibril aggregates observed in the hyaluronidase digestion media. Bar = 0.1 µm x 86,000.

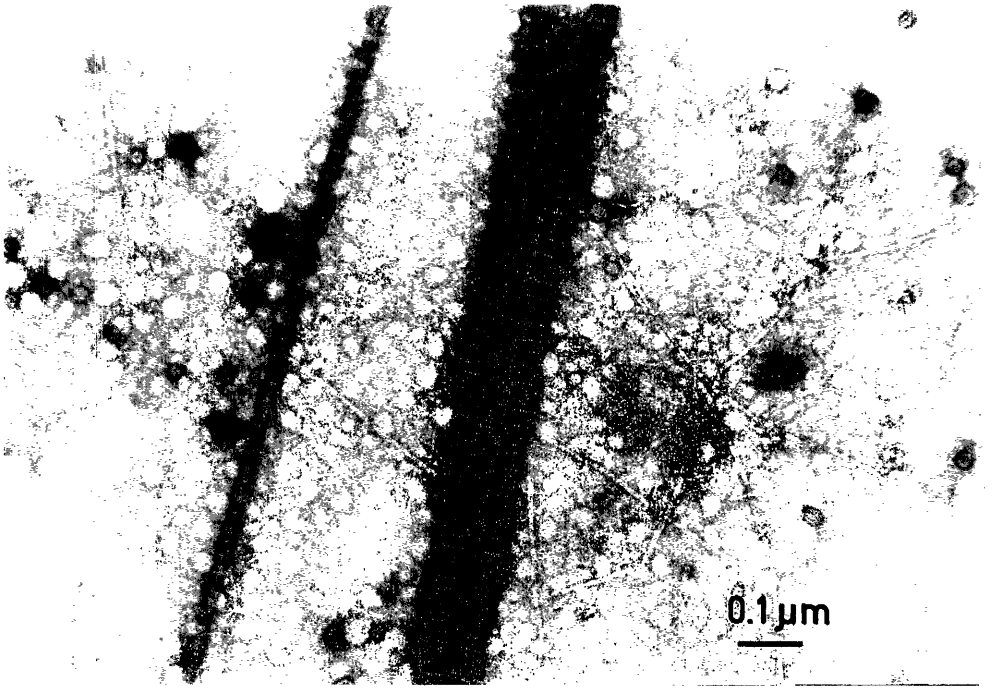

Figure 4.12 Electron micrograph of typical mature collagen fibril observed in the first 20 ml of collected irrigation fluid. Bar = 0.1 µm x 86,000.

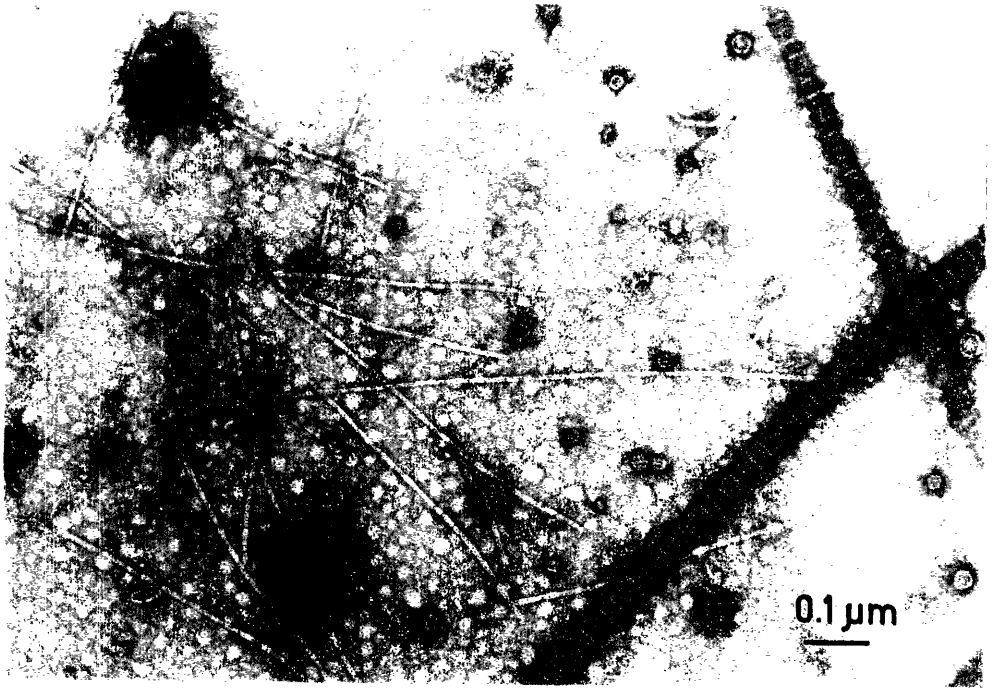

Figure 4.13 Electron micrograph of typical unbanded filaments observed in the first 20 ml of collected irrigation fluid. Bar = 0.1 µm x 86,000.

4.3 CONCLUSIONS OF COLLAGEN FIBRIL ISOLATION

The PG digestion technique utilized was a modification of the sequential enzymatic digestion procedure for the complete extraction of PG components from intact articular cartilage explants developed by Chun *et al* [14]. They have showed that this technique strips the PGs from the solid matrix of the ECM under mild conditions without damage to the collagen network. Since the collagen network is left intact by the enzymatic digestion, the mature fibrils which are observed in the digestion media are probably fibrils which have been sheared in the process of plug sectioning or coring, and have fallen out of the plug due to the vigorous shaking during the digestion process. This is also consistent with the findings of Mendler *et al* [60] who showed by rotary shadowing that blunt fibril ends result from shearing of the fibril leaving frayed molecules, and the work of Kadler *et al* [40] which indicated that tapered ends are a manifestation of growing fibrils. During initial digestion with chondroitinase most of these sheared fibrils may become loosened from the plug and present themselves in the media, but since the media is also filled with GAGs, they may be obscured in the micrograph (Figure 4.3). Then later, as the tissue is further digested with hyaluronidase, entire tissue fragments (Figure 4.11), along with the fibrils whose tapered ends were embedded deeper in the plug (Figure 4.9 and 4.10), may become loosened from the plug. Fibrils which crossed the cut surface twice would have two blunt ends and be more readily seen in the chondroitinase digestion control media; hence the presence of only blunt ended fibrils in the chondroitinase digestion control media, fewer fibrils with some tapered ends in the hyaluronidase digestion media, and no fibrils in the hyaluronidase digestion control media. Furthermore the presence of these tapered ends on mature banded fibrils of Ø40 nm and the presence of fibrils with drastically varying diameter (Figure 4.4 - 4.6), indicate that these mature fibrils are in the process of growing (both lengthwise and in diameter), and that these fibrils may have at least one loose end in the ECM.

The filaments isolated in the irrigation fluid are of more interest to this investigation than the mature fibrils seen in the digestion media. The Ø10.4 ± 0.5 nm x 1.06 ± 0.03 μm size indicates that they are a multimolecular assembly larger than SLS-units observed *in vitro* [10] and smaller than fibril segments reconstructed by Birk *et al* from sequential TEM slices in the embryonic tendon [7].These filaments are also similar in size and nature to those isolated from chick embryo sterna [9]. These filaments may be the loose building blocks of larger collagen fibrils, and they may have become oriented before attachment to growing fibrils. Although the tapered ends and varying diameter fibrils, seen above, are smoother than the 10 nm increments produced by planer assembly of these filaments, the TEM micrographs are

projections and these increments would not be observable under circumferential filament packing.

Finally a discussion of the problems associated with this experiment is necessary. The experiment was conducted seven times with several plugs irrigated during each session. The initial session produced irrigations of two plugs while the other plugs compacted under the fluid pressure. The following sessions were plagued with either leakage around the plug or compaction of the plug. The problem appears to be that when the PGs are digested from the plug, the compressive modulus decreases and the plugs are more prone to collapse. Furthermore, some changes in dimensions can occur during PG digestion. The initial plugs were cored with a unique dental corer which was subsequently damaged and other later corers never produced appropriate plugs for irrigation. Also the tissue from the first two experiments were harvested from near neonatal animals, whereas tissue from later trials were harvested from animals two to four weeks younger. Since the measured equilibrium modulus differed by as much as 10x between these animals and three month-old bovine samples, it could be assumed that there were also some differences in permeability between the tissue used in the first two trials and subsequently used tissue. Thus for all of these reasons, the isolation of fibrils was not repeated to identify collagen type by immunolabelling with monoclonal antibodies. Even so, it is hard to imagine that any macromolecular substance with this filament structure, other than collagen, could exist in fetal cartilage.

CHAPTER
FIVE

DRAG INDUCED ORIENTATION MODEL

5.1 INTRODUCTION

As introduced in Chapter 4, the drag induced orientation mechanism has been observed for a body force acting on short stiff fibers in gels (i.e. gravity acting on a metal fiber in 1% gelatin and other gels). This observation led to the hypothesis that loose collagen fibrils, formed within the entangled molecular network of PGs in cartilage ECM, may become oriented via this mechanism before incorporation into the extant collagen network. It was also consistent with the molecular scale observations of Laurent *et al* for centrifugal forces acting on short pieces of sodium deoxyribonucleate (530,000 MW) in a gel-like highly concentrated hyaluronate polymeric solution [43]. However, for this mechanism to function in cartilage, various conditions pertaining to the geometry and mechanical properties of the loose collagen fibrils and the PG network must be satisfied. Since it was beyond the scope of this thesis to determine all of these parameters and to determine the physical relationships required for the function of this mechanism in cartilage, only the isolation and characterization of the loose collagen fibrils (Chapter 4) and the development of a physical model to study the required physical relationships were conducted.

In this chapter, various physical models are presented in order of complexity. Because, the phenomenon was not well undertood, the most simplistic model was first attempted with full

knowledge of its limitations. Then, additional capabilities were incorporated into this model to allow for a more complete description of the entire complex phenomenon observed. The resulting model was validated by its ability to match the analytical solution for a slender body sedimenting in a viscous fluid, and by experimental data of a fiber sedimenting in a 1% gelatin gel. Finally, various PG network parameter values calculated from the literature and collagen fibril parameters measured in this thesis, were used with the model to predict the potential of this mechanism to orient collagen fibrils in cartilage *in vivo*.

5.2 QUASI-STATIC MODELS

5.2.1 FINITE ELEMENT MODEL

As explained in the presentation of the drag induced orientation mechanism (Section 4.1), the orienting moment is produced by the disturbance of the elastic restoring force of the network perpendicular to the fiber. Hence a quasi-static model was developed to describe a fiber moving in an elastic space. This model neglects the dissipative resistance or time dependent motion both perpendicular and parallel to the fiber axis, and focuses on the elastic interactions between the fiber and network perpendicularly. The model assumes that there is no relaxation and retardation of the network (elastic space) and that the fiber is massless and rigid. The model also assumes that the radius of the fiber is not much larger than the average pore size of the network. Hence, the elastic resistance of the network parallel to the fiber is negligible, and therefore less than the component of body force on the fiber in that direction, $F_{\parallel}$, moving the fiber parallel to its axis. For each amount of movement parallel to the fiber axis, a corresponding motion can be calculated for the amount of turning and the displacement perpendicular to the fiber axis.

The quasi-static model was first implemented using the finite element (FE) method to model the elastic network as a continuum. The model was developed and simulated with ADINA v5.0 on an SGI Indigo computer. The network or elastic space is modeled with isotropic incompressible shell elements - a mesh of 20 x 20, initially square, eight-noded parabolic elements, rigidly fixed along its outer boundary. The fiber is modeled with 8 linear beam elements overlaid and connected to the corresponding nodes of eight shell elements, where the rigidity of the beam is much greater than the stiffness of the network. The resulting "2-dimensional" fiber/gel mesh is composed of 1281 nodes (Figure 5.1). The movement of the fiber is modeled as quasi-static. Initially a component of the body force, $F_n = F \cos \theta$, is applied $\perp$ to the fiber, pushing the fiber downward (Figure 5.2). After calculation of the

reactive forces on the fiber (from the network), some nodes are repositioned in the mesh prior to loading (i.e. prior equilibrium mesh) to allow for fiber motion parallel to the its axis. In the next step, the fiber is moved along its axis, and the still applicable reactive forces (at the old contact nodes between fiber and network) and F_n, adjusted for new fiber position (always at the fiber centroid), are applied. In this manner, the new equilibrium position and orientation is calculated (Figure 5.3). This process is iterated and the drag induced orientation of the fiber parallel to its trajectory is simulated (Figure 5.4). This method works well, but was not efficient, because the process of FE model modification between each iteration could not be automated with the FE code. Using this model for studying physical relationships (e.g. effect of fiber length to network modulus) would have been cumbersome and time consuming; thus other modelling methods were explored.

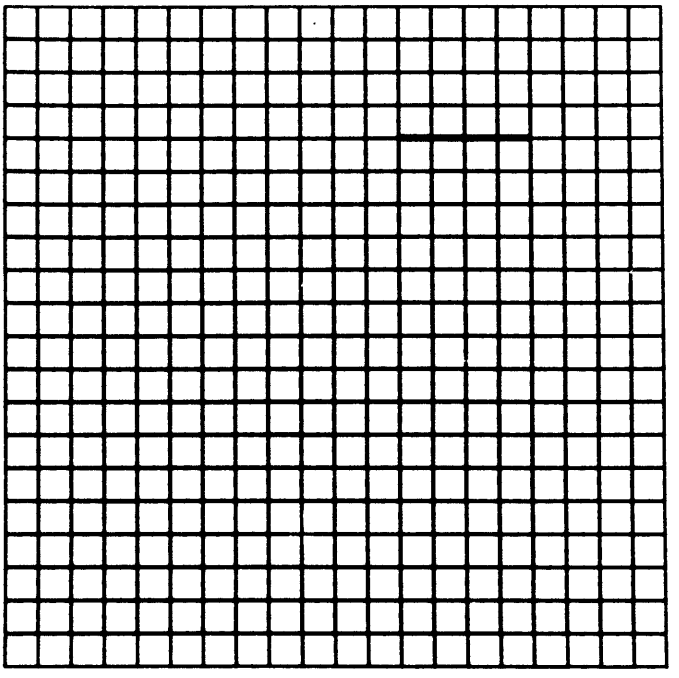

Figure 5.1 Unloaded "2-dimensional" FEM mesh composed of a network (20x20 grid of eight-noded parabolic shell elements) and an inlaid fiber (8 two-noded linear beam elements).

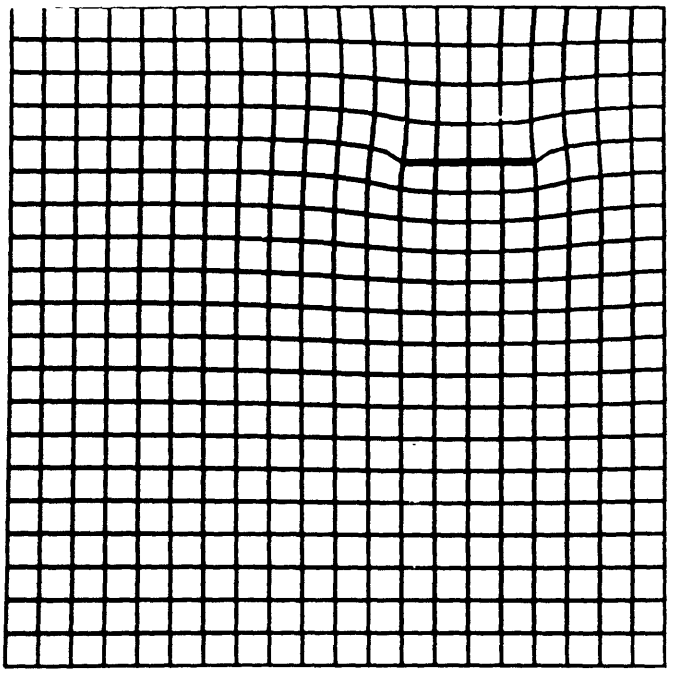

Figure 5.2 Deformed FEM mesh after initial load: $F = F_n$ applied to a horizontal fiber.

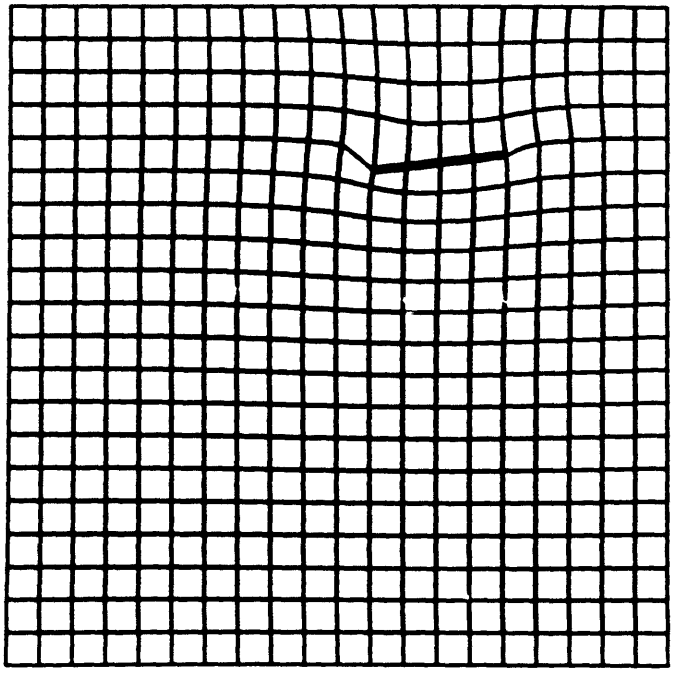

Figure 5.3 Deformed FEM mesh after one iteration: F_n and reaction loads from the initial deformation applied after movement of the fiber by an eighth of its overall length.

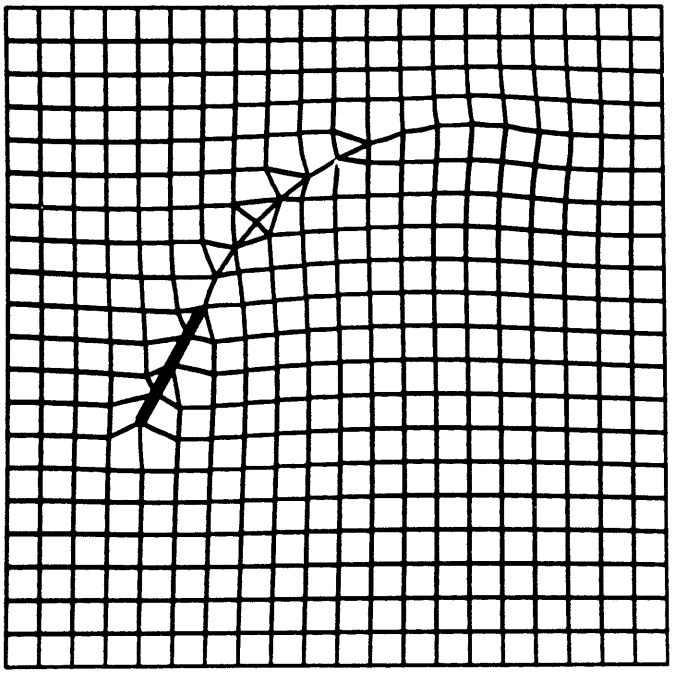

Figure 5.4 Deformed FEM mesh after 13 iterations. The long axis of the fiber is inclined at 62° from the vertical and 12 additional nodes have been created to allow for movement of the fiber in previous steps.

5.2.2 DISCREET MODEL

In this model, the network was represented as n elastic elements each with stress, σ_i, supporting the fiber with a lumped or body force, F, at the fiber centroid (Figure 5.5a). This model is also quasi-static and has the same assumptions as the previous FE model. In addition, the stress state of the network not directly underneath the fiber (but near the ends) is neglected similar to the treatment of beams on an elastic foundation. Similar to the FE model, the fiber is moved forward by length/n. As the fiber moves, the energy stored in the spring no longer loaded by the fiber is lost and the tip of the fiber moves into an unstrained network in the front (Figure 5.5b). This imbalance of supporting force, $\Sigma\sigma_i$, and applied force, $F_n = F \cos \theta$, creates a moment, M, which causes the fiber to turn and translate perpendicularly in order to re-establish equilibrium (Figure 5.6a and 5.6b). As the fiber proceeds to move by length/n along its axis, it continues to turn until it is parallel with the direction of the lumped or body force. This model was simulated on an SGI Indigo computer and found to converge to $\leq 0.1\%$ tolerance at $n \cong 100$ (simulation code in Appendix A). It was also found that this quasi-static motion can be described by one dimenionless parameter, δ / l, where δ is the

displacement perpendicular to the fiber axis under the lumped force, F, and l is the length of the fiber. As expected, Figure 5.7 shows that as the network becomes stiffer the ratio δ / l is reduced and the fiber path changes, making the turning rate slower with repect to translation of the fiber.

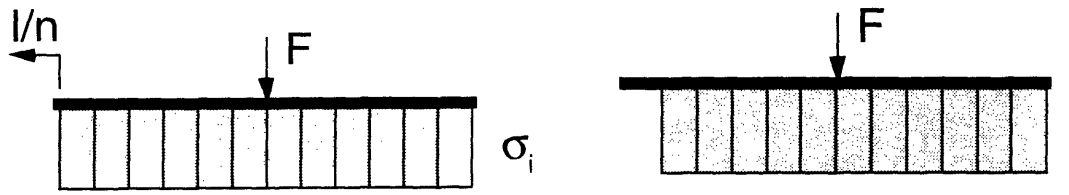

(a) Initial Equilibrium (b) After || Movement l / n

Figure 5.5 Discreet Quasi-Static Model of Drag Induced Orientation

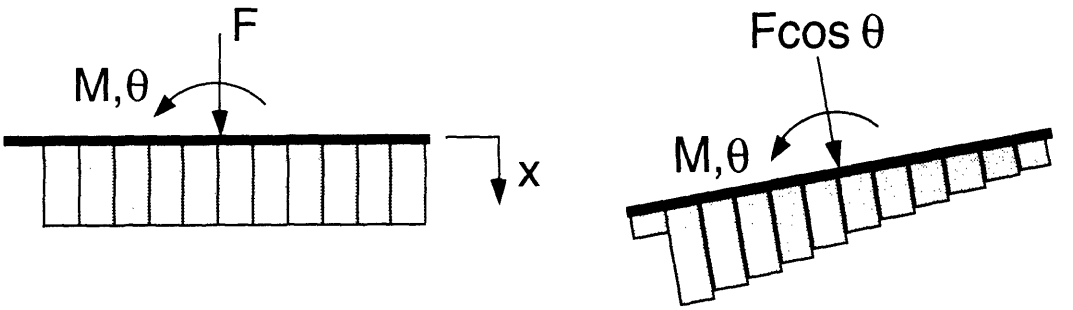

(a) Imbalance of Moment and Force (b) Re-establishment of Equilibrium

Figure 5.6 Discreet Quasi-Static Model of Drag Induced Orientation.

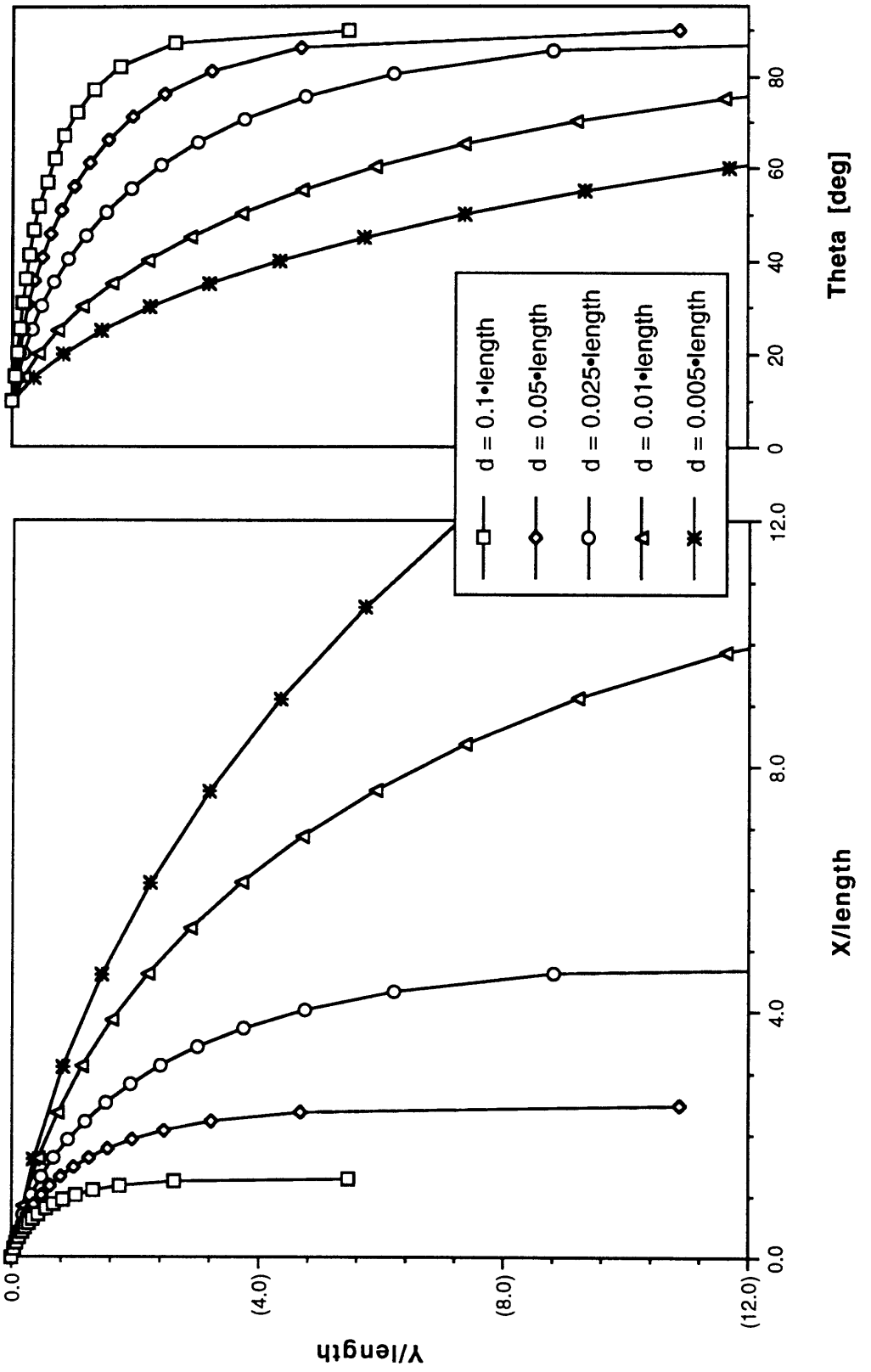

Figure 5.7 Discreet Quasi-Static Model Predicted Path of a Rigid Massless Fiber Sedimenting in an Elastic Media (δ / l).

5.3 DISCREET TIME DEPENDENT MODEL

5.3.1 MODEL

The quasi-static discreet model was further developed into a full discreet time dependent model. The fiber was still considered to be rigid and massless. The dissipative resistance or time dependent motion both perpendicular and parallel to the fiber axis was added (Figure 5.8). This lumped dissipative resistance is the combination of the viscous resistance of 1) the fluid on the fiber, 2) the fiber on the network, and 3) the network on the fluid (retardation of the network), where some or all of the above are applicable. The relaxation of the network was neglected, because for the step-loads used in the analysis, there is always an elastically deformed part of the network supporting the fiber, which moves much like a pressure wave with the fiber. However, this relaxation would have to be taken into account for cyclic loading conditions, and is discussed below (Section 5.4.3). The damping coefficients were input into the model as the resistance in the parallel direction (w.r.t. fiber axis), $b_{\parallel}$, and the ratio of this resistance to that in the perpendicular direction, $b_{\perp} / b_{\parallel}$. The model was simulated on an SGI Indigo computer using an Euler integration routine where dt is the time for displacement of the fiber l / n along its axis, $dt = l\, b_{\parallel} / n\, F\sin(\theta)$ (simulation code in Appendix B). For n = 100, the predicted paths for all analyses conducted was found to converge to within 0.1%.

5.3.2 VISCOUS FLUID

To validate the model, the motion of a slender body sedimenting in a viscous fluid was simulated. The network was made infinitely stiff, $\delta / l = 1 \times 10^{-30}$, and the ratio of resistance perpendicular to the resistance parallel was set to 2.0 [25]. The other parameters, force, length, and resistance parallel to the fiber axis, were set arbitrarily. For a fiber oriented at 54.7° to the vertical, the model predicts that the fiber will not turn and that the angle of the path is 19.5° to the vertical (Figure 5.9). This is in agreement with the analytical solution for low Reynolds number flows [25], and confirms that if no elastic energy is stored by the network ($\delta = 0$) then no turning occurs.

5.3.3 GELATIN GEL

The model was also validated using the sedimentation of a Ø0.6 x 12.6 mm stainless steel fiber in a 1% gelatin gel (as described in Section 4.1). The sedimentation was recorded on 16

mm film at 24 frames/sec with a background grid (5 mm/div), and later individual frames were printed on photographic paper. The position and orientation of the fiber was digitized from these prints taken every 1 sec (sampling rate 1 Hz) using the grid as a reference. A typical print is shown in Figure 5.10 and the path is shown in Figure 5.11. In the model, the gravitational body force, ($F = mg = 2.8 \times 10^{-4}$ N), fiber length (12.6 mm), and resistance in the parallel direction calculated from the terminal velocity ($b_{\parallel} = F / v_f = 5.7 \times 10^{-5}$ N s / mm) are fixed and the best fit values for parameters, δ / l and $b_{\perp} / b_{\parallel}$ are found using least squares criterion (corresponding values of horizontal displacement, X, and orientation, θ, w.r.t. vertical displacement, Y) with DOC (see Section 3.2.2). The resulting model predicted path with $\delta / l = 0.19$ and $b_{\perp} / b_{\parallel} = 5.76$ corresponds to the gelatin experiment with an average error of 0.24 (in mm for X and in degrees for θ), Figure 5.12. The damping coefficients in this model when applied to the case of the metal fiber in gelatin do not correspond to any one physical characteristic of the gel. Since the fiber is probably ripping through the gel, the damping coefficients are most likely a combination of viscous damping from the interstitial water and the plastic deformation of the network. However, the fact that the ratio $b_{\perp} / b_{\parallel}$ is greater than 2.0 does indicate that that the model accounts for something other than simple viscous drag of the interstitial water. Nevertheless, this model has the basic physical relationships necessary to simulate the sedimentation of a metal fiber in a dilute gelatin gel.

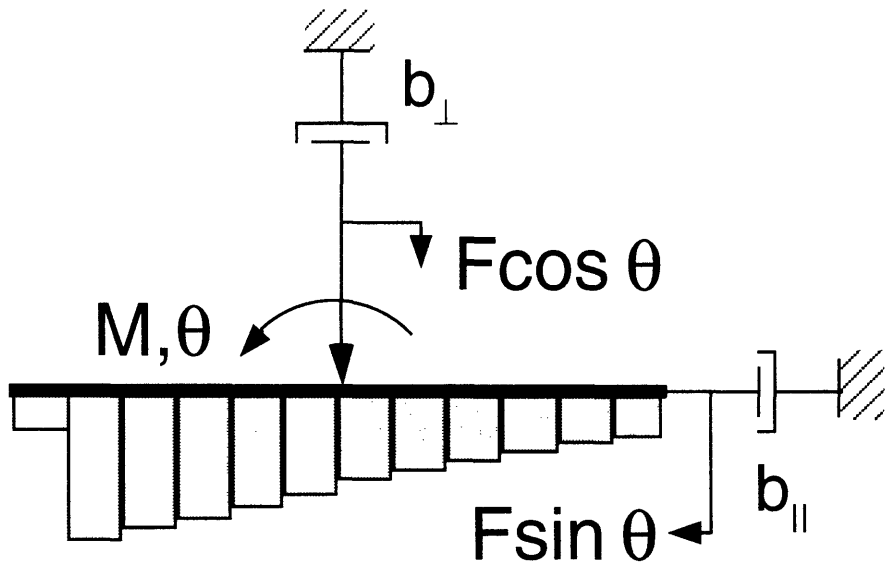

Figure 5.8 Discreet Time Dependent Model of Drag Induced Orientation.

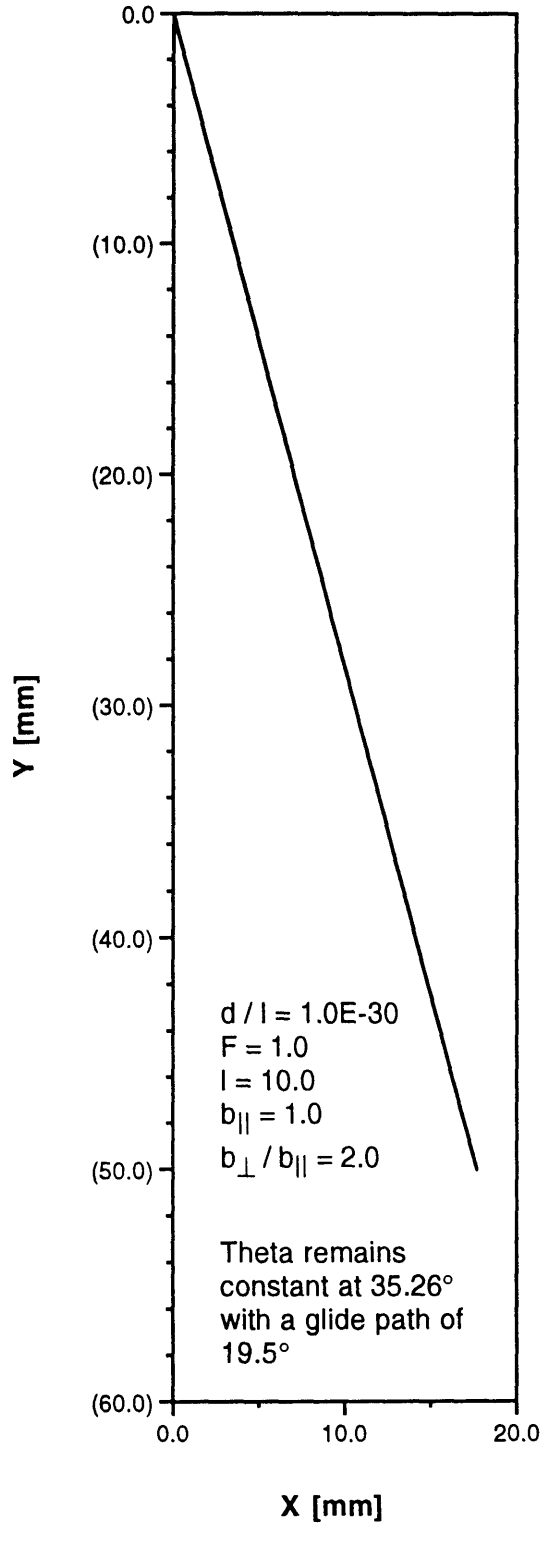

Figure 5.9 Discreet Time Dependent Model Predicted Path of a Rigid Fiber Sedimenting in a Viscous Fluid.

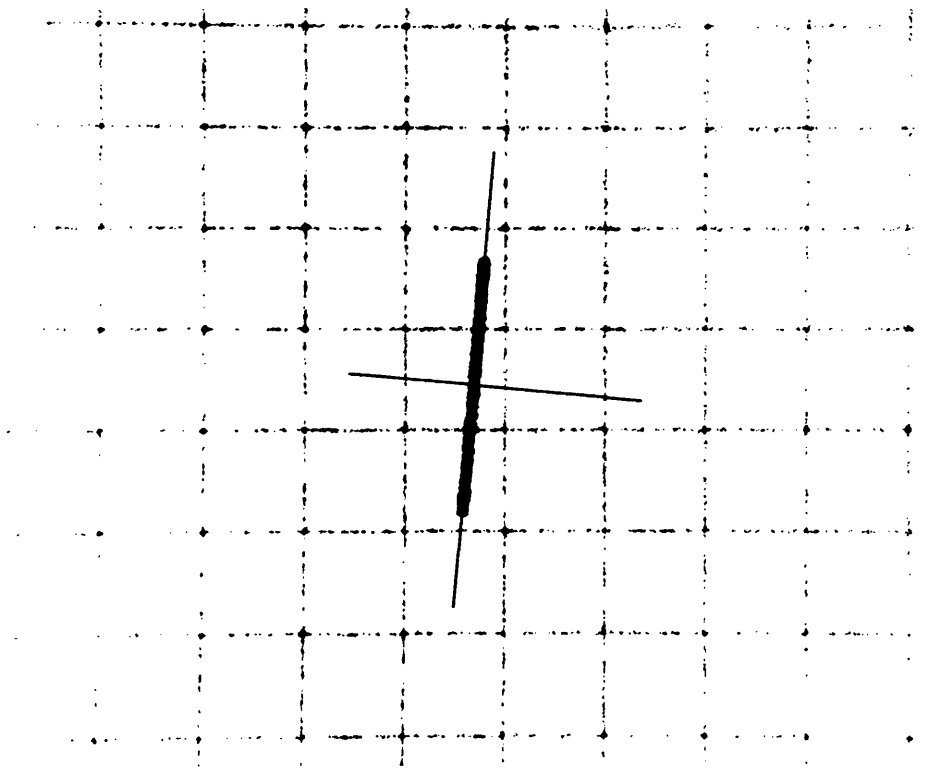

Figure 5.10 A Typical Frame from the 16mm Movie Film used to Record thePath of a Ø0.6 x 12.6 mm Stainless Steel Fiber Sedimenting in a 1% Gelatin Gel.

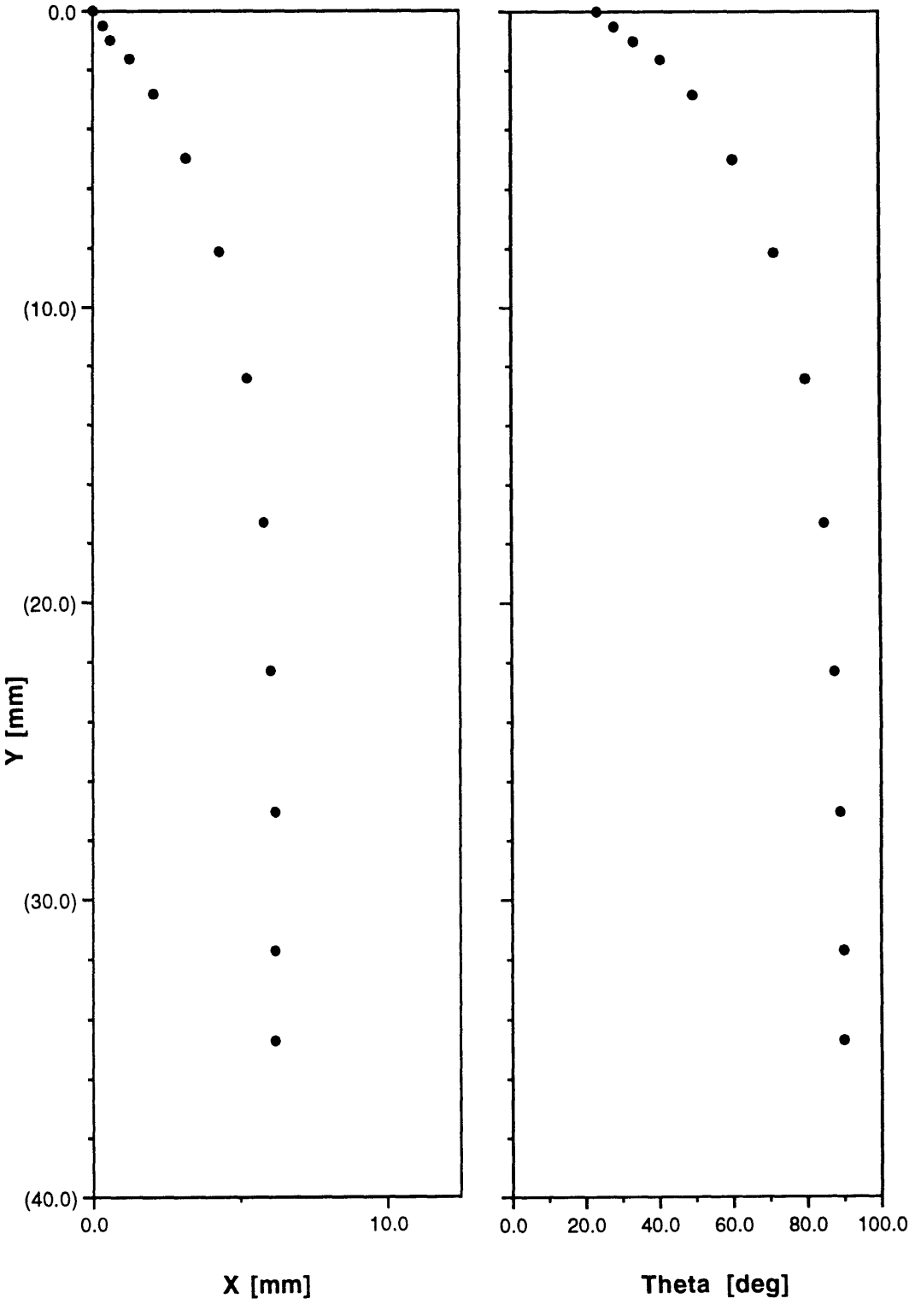

Figure 5.11 Path of a Ø0.6 x 12.6 mm Stainless Steel Fiber Sedimenting in a 1% Gelatin Gel.

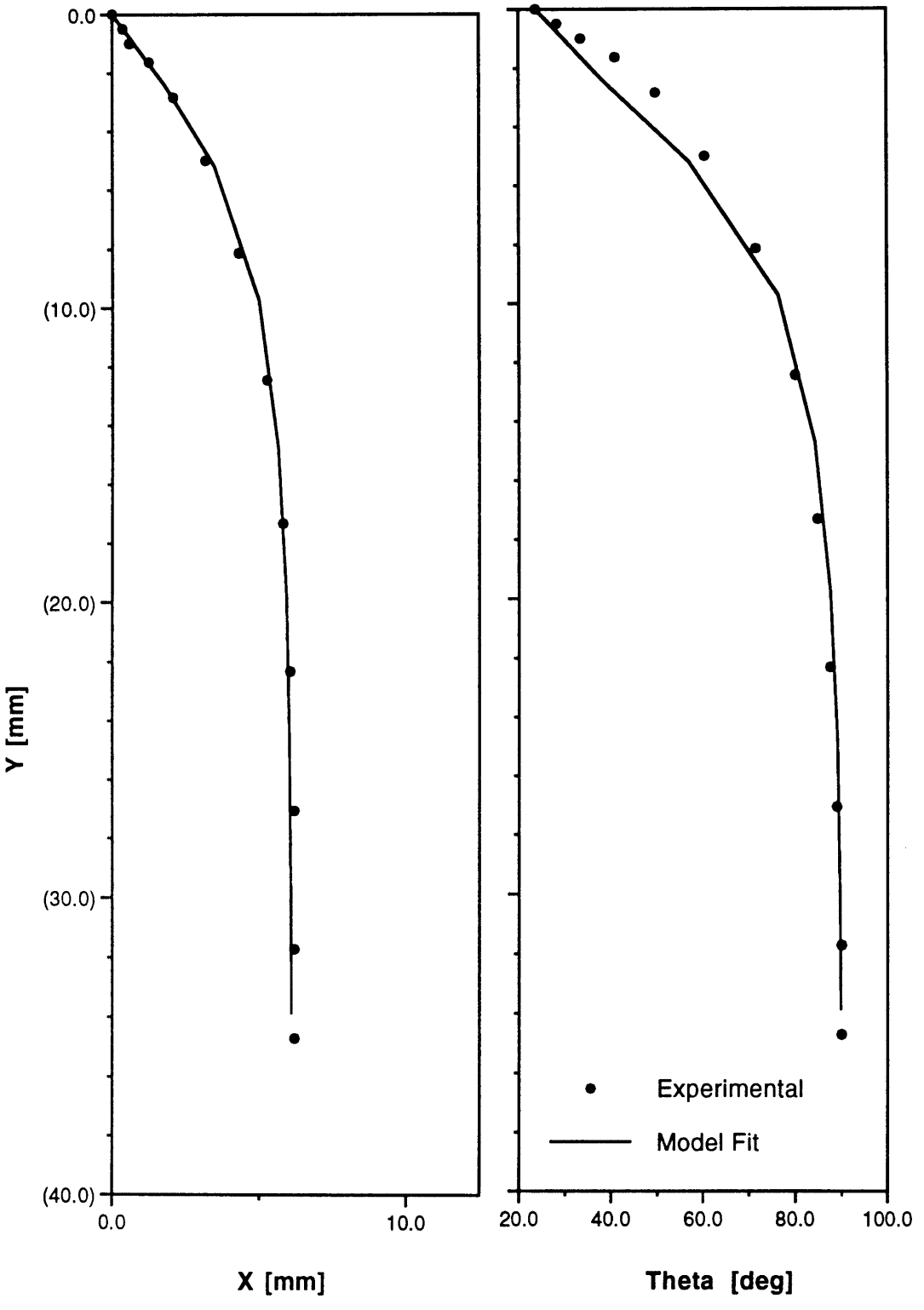

Figure 5.12 Discreet Time Dependent Model Predicted Path of a Ø0.6 x 12.6 mm Stainless Steel Fiber Sedimenting in a 1% Gelatin Gel.

5.4 COLLAGEN IN CARTILAGE ECM

Finally, the developed discreet time dependent model was used to show that loose collagen fibrils could be oriented via the drag induced mechanism in the cartilage ECM. Since not all the parameter values for collagen in cartilage ECM required for the model are known, many of them had to be estimated from known parameter values in the literature. When the method of estimation was in doubt, a range of parameter values was used.

5.4.1 LOOSE COLLAGEN FIBRIL AND DRAG FORCE

The amount of drag force that the fluid flow can exert on the loose collagen fibril was estimated from the motion of long slender bodies in an external creeping flow. As the joint is loaded, cartilage deforms and a flow of the interstitial fluid is produced. Because the fluid is incompressible, the velocity of the fluid with respect to the solid matrix is approximately the rate of deformation of the joint surface. This deformation was measured by Armstrong et al using in vitro loaded human cadaveric hip joints [1]. They loaded the joints *in vitro* with 5 times body weight in the coronal plane of the femoral shaft and at 22.5° medially. The consolidation of the cartilage was measured by roentgenography at discreet points on the articular surface and then averaged to give a load normalized creep function, *f(t)*:

$$f(t) = \frac{h(t) - h_o}{h_o P} \tag{5.1}$$

where: h(t) is the cartilage depth, h_O is the cartilage depth under no load, and P is the pressure. Assuming negligible flow tangentially:

$$|v| = \dot{h} = P h_o \dot{f} \tag{5.2}$$

where v is the fluid flow velocity. From *in vivo* measurements, the maximum pressure recorded during gait in the human hip joint was 5.5 MPa [32]. Asuuming sinusoidal pressure patterns, the average pressure would be 2.75 MPa. Tepic measured the geometry of the human hip joint with ultrasound and found the depth of cartilage to be between 1.0 and 2.5 mm, but thicker in major load bearing areas [93]. Thus for a pressure of 2.75 MPa and a swollen thickness of 2.0 mm, the fluid velocity calculated from the first 11 sec of the creep curve is on the order of 1 μm/sec.

As described in Section 4.2.3, loose collagen fibrils of size Ø10.4 ± 0.5 nm x 1.06 ± 0.03 μm were isolated from the ECM of full-term bovine fetal femoropatellar articular cartilage. Thus the Reynolds number, Re, calculated with the fibril dimensions, is small and principles of creeping flow can be applied (the inertial effects of the flow are neglected):

$$\mathrm{Re} = \frac{\rho v l}{\mu} < 1\mathrm{x}10^{-6} \tag{5.3}$$

where: ρ and μ are the density and viscosity of water, l is the chracteristic length of the fiber (length or radius), and v is the velocity of the fluid. Unfortunately, unlike the drag on a sphere in a uniform flow field, the drag on an infinitely long cylinder cannot be treated using creeping motion equations (Stoke's paradox). Although many have solved for the approximate solution to this problem, Cox most recently obtained the drag force on a circular cylinder of finte length as an asymptotic expansion in terms of the ratio of cross-sectional radius, r, to body lenth, l:

$$\begin{aligned} F_{\parallel} &= \frac{2\pi\mu l v \sin\theta}{\ln(l/r) - 1.5 + \ln 2} \\ F_{\perp} &= \frac{4\pi\mu l v \cos\theta}{\ln(l/r) - 0.5 + \ln 2} \end{aligned} \tag{5.4}$$

where: $F_{\parallel}$ and $F_{\perp}$ are the force parallel and perpendicular to the fiber axis [16]. Using his fomulas, the drag force on the loose collagen fibrils is estimated to be $F_{\perp} = 2.29 \times 10^{-15}$ N, for l = 1.0 μm, r = 5 nm, μ = 1 centipoise, v = 1 μm/sec, and θ = 0°..

The rigid fiber assumption used to formulate the model can also be verified with the calculated drag force and fiber geometry. For a simply end supported cylindrical beam loaded with a lumped force at the center, the maximum deflection, δ_{max}, is:

$$\delta_{\max} = \frac{F l^3}{12 E \pi r^4} \tag{5.5}$$

where, F is the lumped force, E is the modulus of the fiber, l is the length of the fiber, and r is the radius of the fiber. For the geometry of the loose fiber, the drag force, $F_{\perp}$, and a modulus of 1.4 GPa measured for type I collagen fibers in the rat tail tendon [4], the upper limit for the deflection of the loose collagen fibrils is 0.069 nm or 0.69% of the fiber radius. Thus, our assumption of a rigid fiber is justified.

To verify the assumption of the massless fiber, the upper limit of the mass was calculated from the molecular weight of collagen molecules. For a molecular weight of 90kd for type II collagen molecules, the mass of the loose collagen fibril, m, is approx. 22.1 x 10^{-21} kg, assuming 100% collagen per fibril. The accelerations, a, predicted by the model for all simulations were less than 2 x 10^{-10}m/sec^2. Thus, the ratio of inertial forces experienced by the fiber to the drag force, ma/$F_\perp$, is on the order of 10^{-15}, and the assumption of a massless fiber is justified.

5.4.2 PROTEOGLYCAN NETWORK

The stiffness of the PG network embedded within the extant collagen network was calculated from viscoelastic measurements of PG solutions and FE analysis. As the loose collagen fibril is dragged by the fluid flow, it is forced to move relative to the fine molecular network of PGs. Hence the stiffness of the network is that of the entangled PG molecule solution embedded or fixed by the extant collagen network. The modulus for this PG network is different than that of the cartilage because the modulus of cartilage is a result of Donnan osmotic equilibrium with bulk compression and exudative flow of interstitial fluid whereas very little interstitial fluid is displaced and no bulk compression of the PG network occurs during the movement of the fibril.

The modulus of the PG network (not of the cartilage ECM) was determined from viscoelastic measurements conducted by Mow *et al* on PG solutions of near physiological concentration and percent aggregation [69]. They measured the dynamic complex shear modulus, |G*|, and the phase shift, ϕ, between stress and strain for various concentration of PG solutions containing purified PG aggregates isolated from bovine nasal cartilage. From these two parameters the modulus of the PG solution, E, was calculated:

$$
\begin{aligned}
E &= \frac{2(1+\nu)|G^*|}{\sqrt{1+\tan^2\phi}} \\
\text{where } |G^*| &= \sqrt{G'^2 + G''^2} \\
\tan\phi &= \frac{G''}{G'} \\
E &= 2(1+\nu)G'
\end{aligned}
\qquad (5.6)
$$

and ν is the Poisson's ratio, G' is the real part of the complex shear modulus, and G" is the imaginary part. For the PG aggregate solution of 50 mg/ml at 1Hz the tan ϕ is 2.2 and the

complex shear modulus is 2.2Pa. Thus, the modulus of the PG aggregate solution, assuming a Poisson's ratio of 0.5 [91], is 5.6 Pa.

Next an FE model of the PG entangled network imbedded in the extant collagen network was created. From the TEM photos of the unloaded cartilage ECM (Section 2.2.3), the average spacing of the collagen fibrils in the extant network was approximately 1 μm. Consequently, a mesh was created from 500 parabolic brick elements arranged into a 1.0 x 1.0 x 0.5 μm square half cube with material properties corresponding to the PG aggregate solutions calculated from viscoelastic measurements. The nodes on the plane of symmetry were restrained to that plane and the nodes along the external edges were translationally fixed to model the immobilization by the extant collagen network. The rigid loose collagen fibril was modelled by constraining colinear nodes along a 1 μm length element interface in the plane of symmetry to move rigidly. The center node along this interface was loaded with the drag force (Figure 5.13). This linear static FE model was developed and solved on an SGI Indigo computer using IDEAS (from SDRC Inc.). A typical deformed mesh (max strain = 5% deformation) on the cut plane corresponding to the plane of symmetry is shown in Figure 5.14. From the model, a stiffness ($k = F_d/\delta$) of 2.5 x 10^{-6} N/m was calculated for the PG aggregate entangled network embedded within the extant collagen network.

The dissipative resistance of the PG network to fiber motion can be thought of as arising by two different modalities. One situation would be similar to the fibril moving through an entangled solution of PG aggregates with allowed bulk flow of the PG aggregates. In this case the dissipative resistance would simply be a function of the PG aggregate solution viscosity:

$$b_{\parallel} = \frac{2\pi\mu l}{\ln(l/r) - 1.5 + \ln 2}$$
$$b_{\perp} = \frac{4\pi\mu l}{\ln(l/r) - 0.5 + \ln 2} \tag{5.7}$$

calculated by the formula derived by Cox for the drag force on a circular cylinder with radius, r, and of finte length, l [16]. However, the PG aggregate solution is a non-Newtonian fluid and has a shear rate dependent viscosity. Hence, the upper limit of the damping coefficients were calculated from the zero shear rate viscosity measured by Mow *et al* [69]. Their measurement of 2.6 N s/m^2 for the zero shear rate viscosity of 50 mg/ml PG aggregate solution gives $b_{\parallel}$ = 3.64 x 10^{-6} N s/m and $b_{\perp} / b_{\parallel}$ = 1.64.

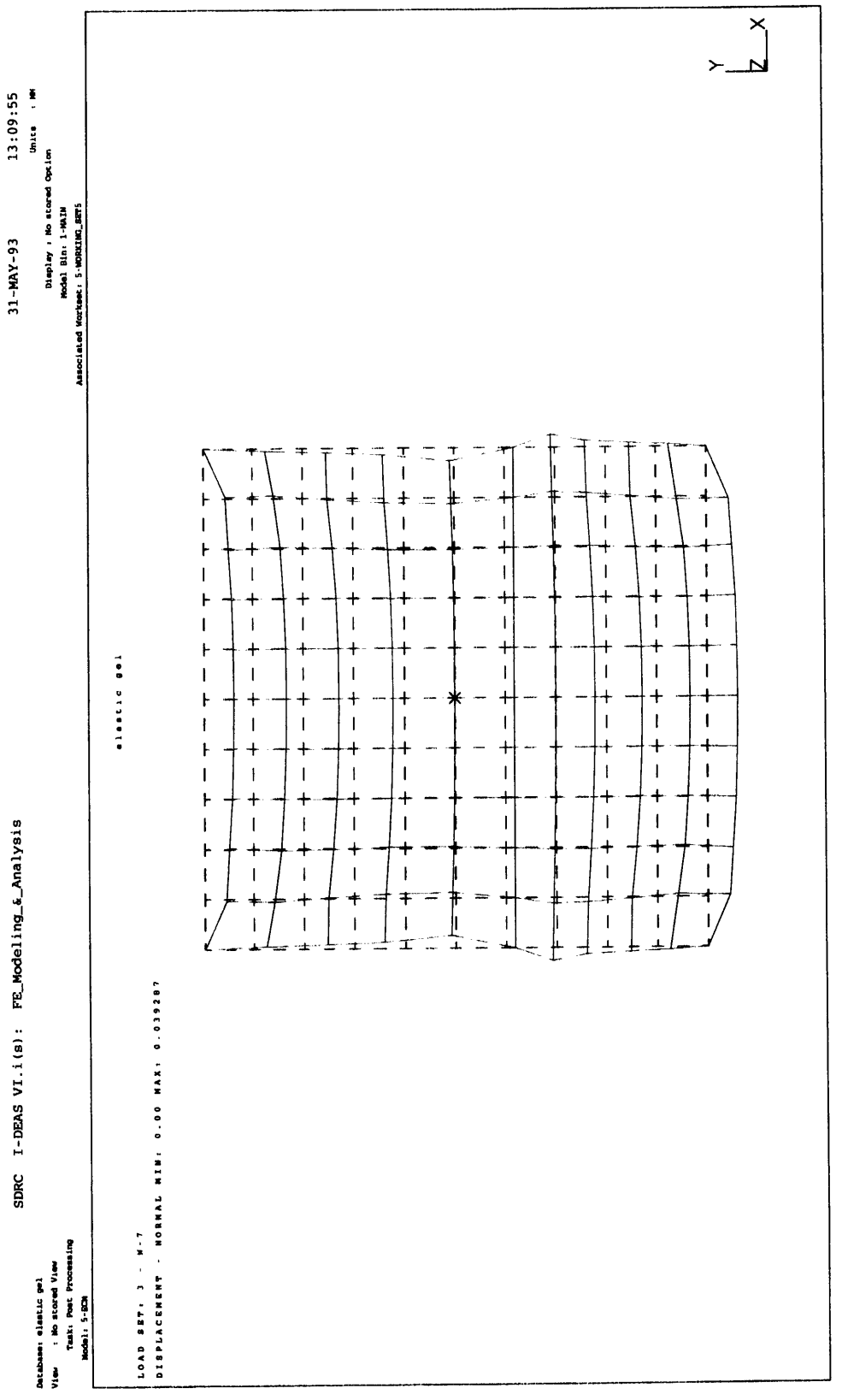

Figure 5.13 FE Model Mesh of Entangled PG Aggregate Gel-like Solution Embedded within a 1 μm Spaced Collagen Fibril Network.

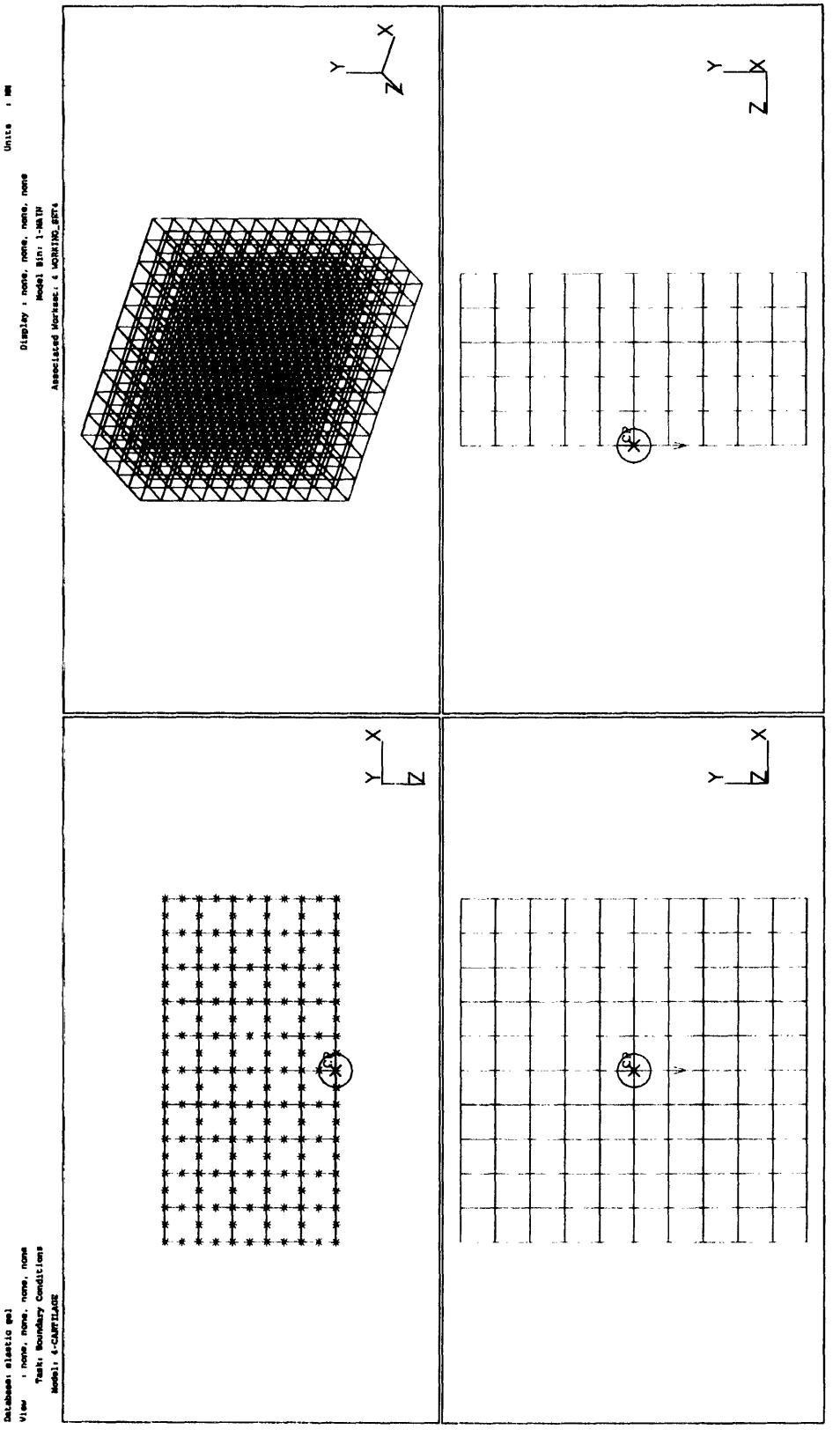

Figure 5.14 Deformed FE Model Mesh of Entangled PG Aggregate Gel-like Solution Embedded within a 1 μm Spaced Collagen Fibril Network.

In the other situation, the fiber moves through the entangled network of PG aggregates, but the PG aggregates are bound at discreet points to the extant collagen network and are not allowed any bulk motion. Calculated from concentrations, the PG aggregates are compressed to as much as 20% of their swollen volume [28]. Hence, the space between the PG monomers attached to the hyaluronate backbone is 4 - 10 nm [80], and is similar to the loose collagen fibril diameter. So, as the fiber moves through the PG network, it displaces the individual PG monomers and deforms the PG aggregates, but would not displace PG aggregates relative to each other (Figure 5.15). Thus, in this case, the dissipative resistance comes from the retardation of the network (dissipative resistance between the network and the interstitial water) rather than the viscosity of the PG aggregate solution because the viscosity is a measure of the bulk flow of PG molecules.

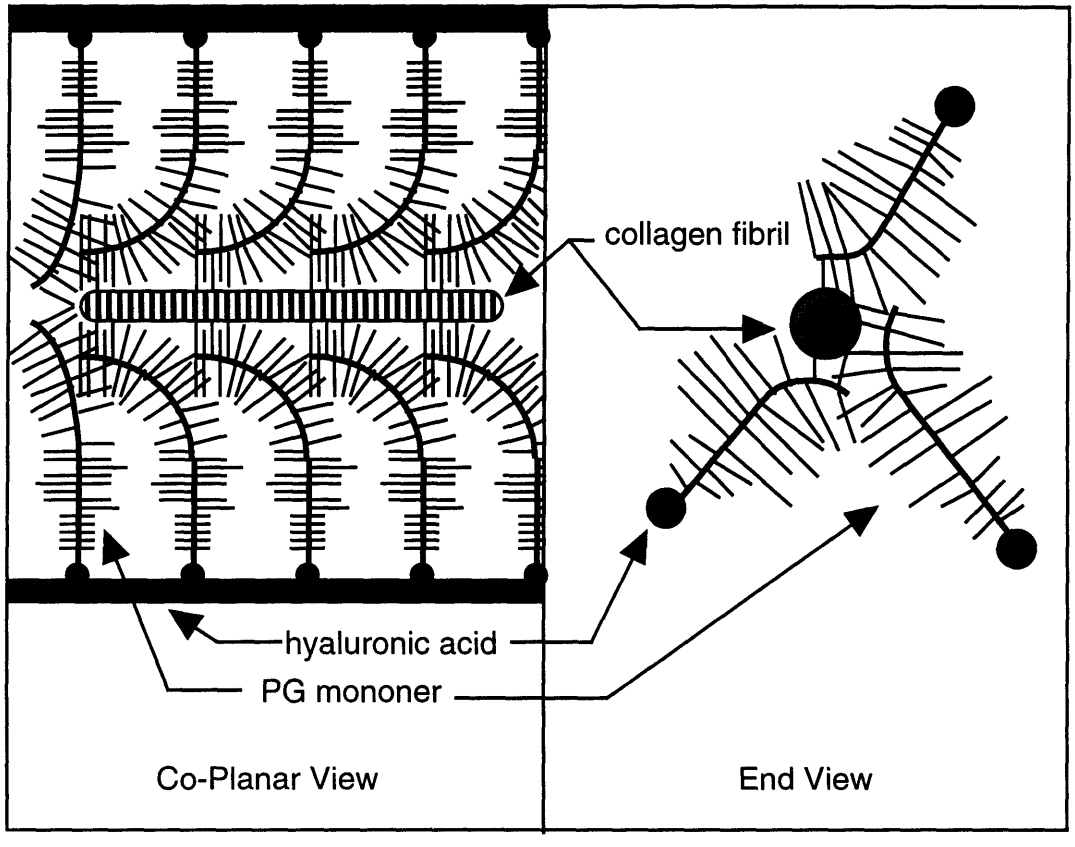

Figure 5.15 Cartoon of Loose Collagen Fibril Moving Parallel to the Fiber Axis through the Entangled PG Aggregate Network Embedded in th Extant Collage Network.

The dissipative resistance in this case was calculated from the retardation time constant derived by Hardingham *et al* from the fit of a four parameter Oldroyd rate-type model to rheological measurements of PG aggregate solutions [26]. They found that the retardation time constant was 0.073 sec for a 50 mg/ml 80% PG aggregate solution. Because the retardation time constant, λ, is a measure of the creep, the damping coefficient can be approximated by equating this to the time constant of a Voigt model of viscoelasticity: $b = k\lambda$, where b is the damping coefficient and k is the stiffness. In the perpendicular direction (w.r.t. the fiber axis) the stiffness is that calculated above for the 1 μm loose collagen fibril in the entangled PG aggregate solution embedded in the extant collagen network. The stiffness in the parallel direction (w.r.t. the fiber axis) is not so straight forward. From the distributed force over a part of the boundary of a semi-infinite solid, the ratio of the stiffness parallel, $k_{\parallel}$, to the stiffness perpendicular, $k_{\perp}$, (w.r.t. to the fiber axis) can be calculated [97]. Since this relationship is approximately correct for an infinite viscoelastic body, the ratio for the geometry of the loose collagen fibril is:

$$\frac{K_{\parallel}}{K_{\perp}} = \frac{0.54}{0.37}\sqrt{\frac{2l}{r}} = 29 \tag{5.8}$$

and the estimated $b_{\parallel}$ is 6.29×10^{-9} N s/m and $b_{\perp} / b_{\parallel}$ is 29.

5.4.3 APPLICATION TO CARTILAGE

The estimated parameter values for the two situations were used to simulate the orientation of loose collagen fibrils in the ECM of cartilage, Figures 5.16 to 5.18.

The path and the orientation along the path are quite different for the two conditions, Figure 5.16. This difference can be mostly attributed to the difference in ratio between the damping coefficients ($\perp / \parallel$). The two conditions also predict turning rates which differ by three orders of magnitude, Figure 5.17 and 5.18. This was not unexpected because the rate of turning is proportional to the forward velocity of the fiber, and the dissipative resistance parallel to the fiber axis calculated from the vicosity measurement is three orders of magnitude larger than that calculated from the retardation time constant. Since the two conditions provide such diverse results, the appropriateness of either condition to the situation in the cartilage ECM must be clarified before the results can be used to examine the potential of this mechanism.

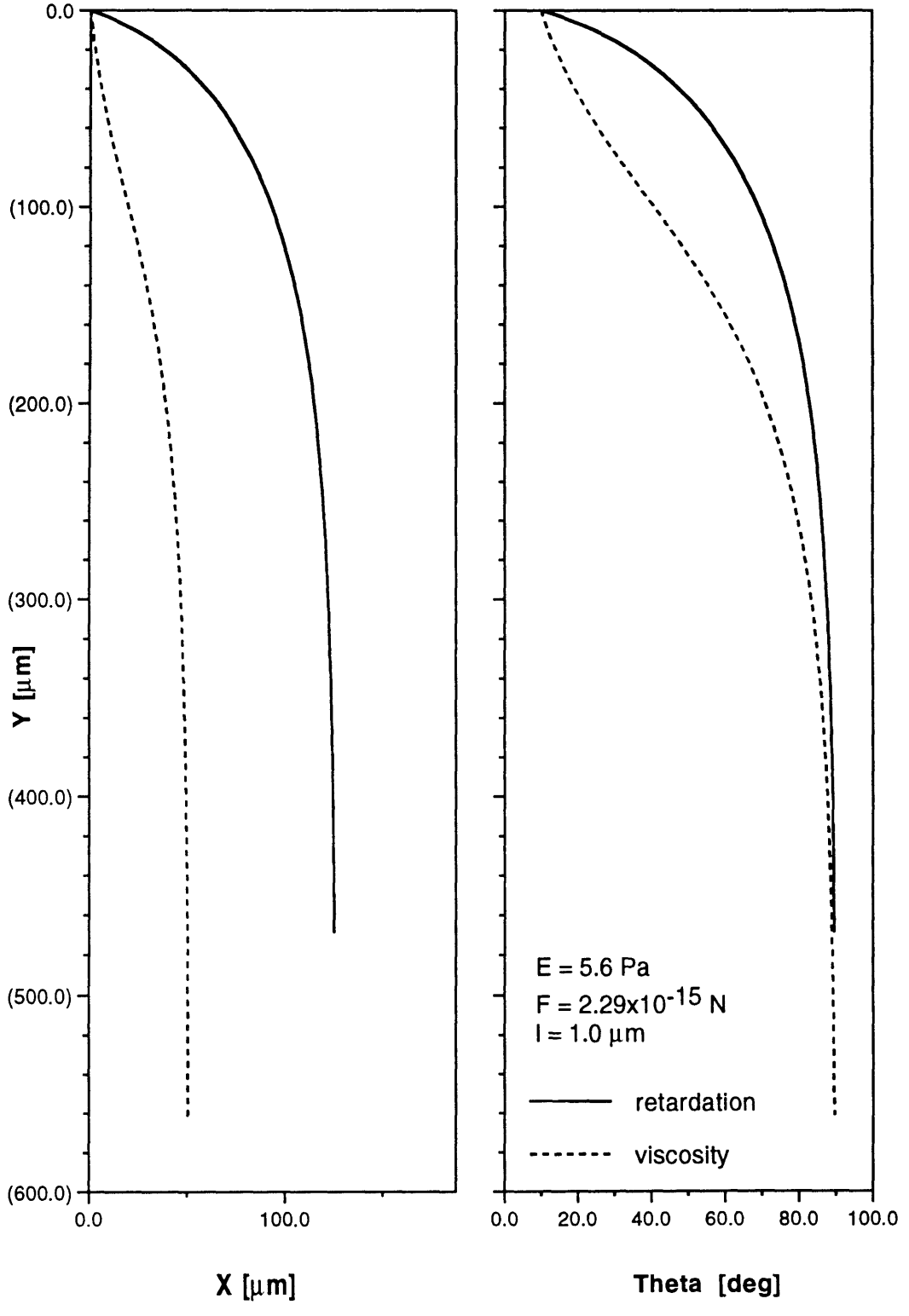

Figure 5.16 Discreet Time Dependent Model Predicted Path of the Loose Collagen Fibril in the cartilage ECM.

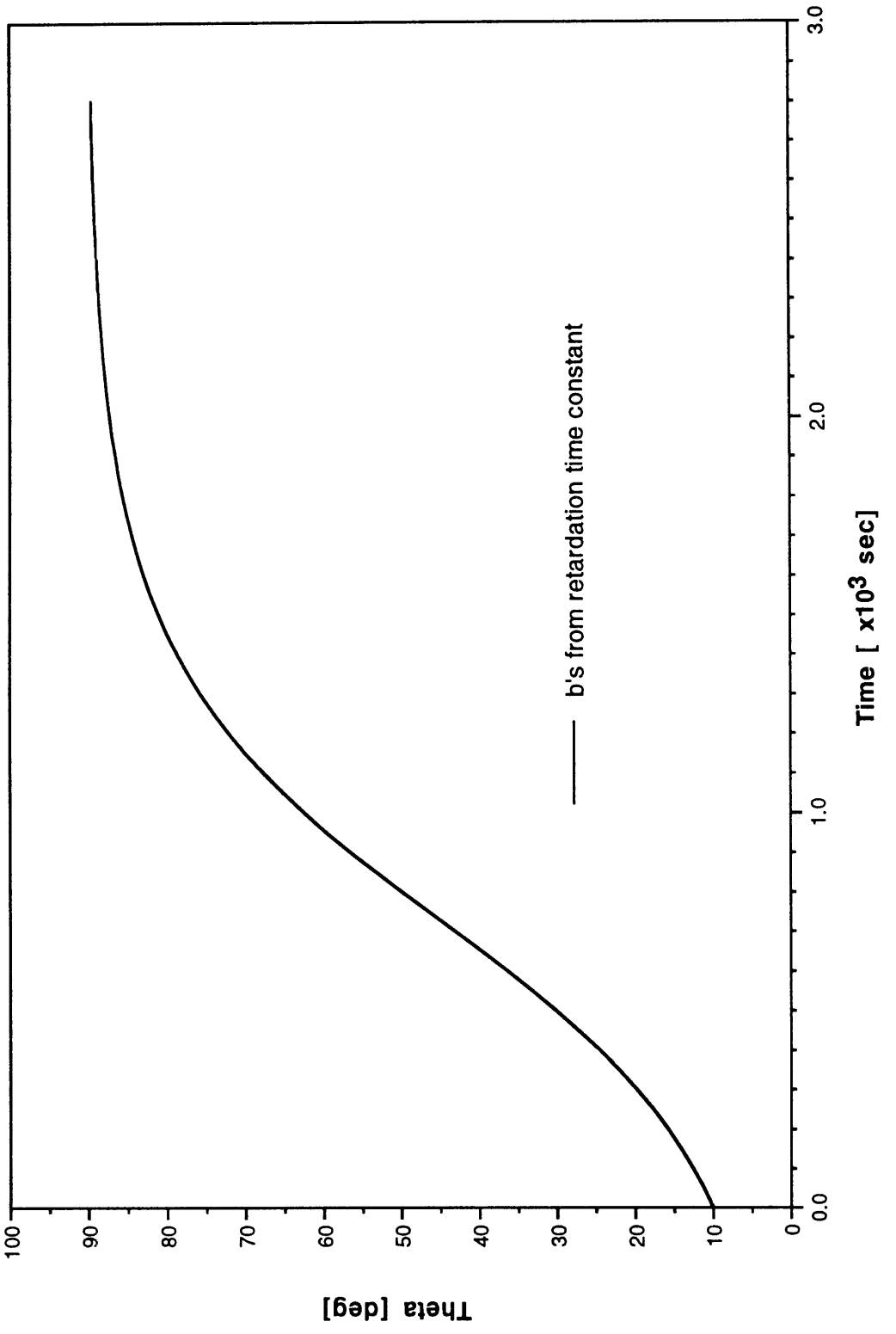

Figure 5.17 Discreet Time Dependent Model Predicted Orientation of the Loose Collagen Fibril in the cartilage ECM (dissipative properties of PG network calculated from retardation time constant of PG Aggregate Solution).

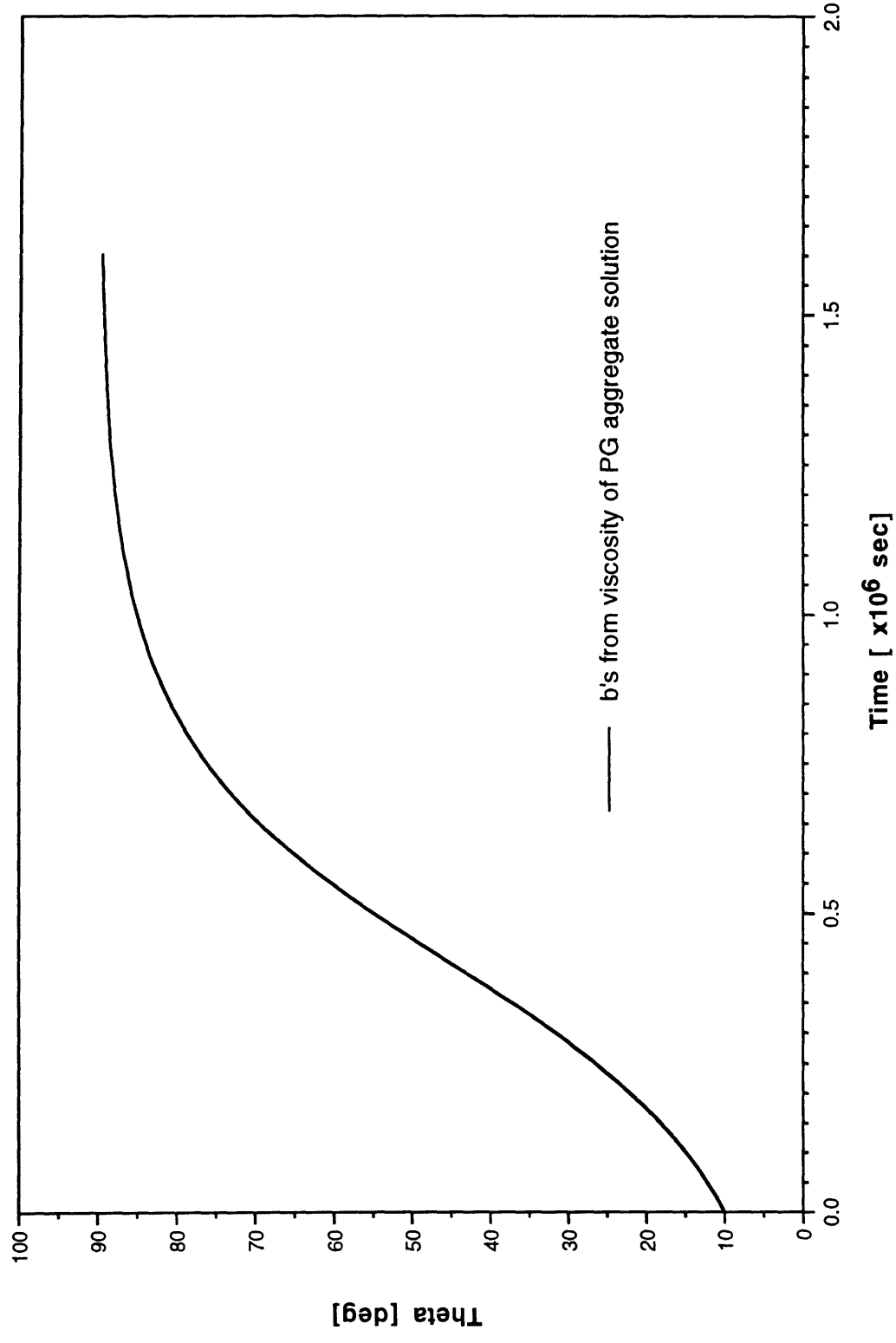

Figure 5.18 Discreet Time Dependent Model Predicted Orientation of the Loose Collagen Fibril in the cartilage ECM (dissipative properties of PG network calculated from zero rate shear viscosity of PG Aggregate Solution).

The work of Laurent *et al* with diffusion of linear polymers in hyaluronate solutions indicates that the appropriate parameter values for the cartilage ECM should be not at either extreme, but rather at some point within this range [43]. In earlier work, they studied the retardation of globular particles through polymer networks and showed that the rate of transport is exponentially related to the diameter of the particle and network dimensions [42]. This relationship was later mathematically modelled by Ogston *et al* [75], and was used to calculate the equivalent (Stoke's) radii for globular particles from the exponential relationship fit to sedimentation measurements in hyaluronate. They found that these equivalent radii were the same as the equivalent radii calculated from sedimentation measurements in water and viscosity measurements. However, for a small rigid linear polymer of sodium deoxyribonucleate, the effective radius calculated from sedimentation in hyaluronate was almost one quarter of that calculated from sedimentation in water or viscosity measurements. This difference was an indication that the rigid linear polymer was moving end wise rather than randomly oriented through the network.

If the rigid linear particle transport rate throught the polymeric network was retarded due to the viscous interaction of the network with the particle, then the ratio of the effective radii for random oriented motion and endwise motion can be calculated from the creep motion equation of Cox (Eqn 5.7). Let the random oriented motion be a result of a force, F, applied for unit time, to the fiber perpendicular to its axis resulting in a displacement, a, and then for another unit time parallel to the fiber axis resulting in a displacement, 1.64 a. Then, the effective radius, r_e, can be calculated by equating this displacement to that of a sphere with radius, r_e (Stokes flow around a sphere):

$$r_e = \frac{F}{6\pi\mu}\sqrt{\frac{2}{1+1.64^2}} \tag{5.9}$$

where μ is the viscosity of the media. For a fiber which only moved endwise the effective radius, $r_{||}$, would be:

$$r_{||} = \frac{F}{6\pi\mu}\frac{\sqrt{2}}{3.28} \tag{5.10}$$

and the ratio of effective radii, $r_{||} / r_e$, is 0.59. Because the ratio of effective radii produced by purely viscous interaction between the rigid fiber and the network is more than twice that calculated by Laurent, the retardation of the endwise moving fiber by the network is due to

some weaker resistance than pure viscosity of the PG network. This is also in agreement with the theoretical work of Ogston *et al*, who described the transport as a stochastic process in which the decrease in the transport rate in a polymer network was dependent on the probability that a particle finds a network 'hole' into which it can move. Hence the resistance to the endwise motion of a loose fibril in PG network is less than that due purely to viscosity of the PG network. Similarly to Laurent's work with hyaluronate, this resistance can be calculated from the molecular dimensions of the PG network and the sedimentation or viscosity measurments of the loose collagen fibrils, but unfortunately, there was not sufficient time in our investigation to develope this further, and the the resistance was assumed to be within the estimated limits.

The loose collagen fibrils oriented by the drag induced mechanism are believed to assemble with other loose fibrils, after orientation, into larger banded fibrils which then become incorporated into the extant collagen network. Leblond *et al* have investigated this incorporation rate, and have shown with radioautography that this occurs within one to several days for dentin and bone matrix [44]. Assuming that the rate of collagen fibril incorporation into the extant network for cartilage is similar to that of bone, the mechanism must orient the loose collagen fibrils within days, under physiological loading conditions. The discreet time dependent model, with dissipative parameter values calculated from the retardation time constant of the PG aggregate solution, predicts that the loose collagen fibril will become oriented within an hour under a constant drag force produced by interstiatial flows of 1μm/sec. However, for dissipative parameter values calculated from the viscosity of the PG aggregate solution, the loose collagen fibril would require more than two weeks for orientation under similar conditions.

In the superficial tangential zone (STZ), the collagen fibrils lie tangential to the articulating surface with local orientation corresponding to the split-line patterns. In this zone, Maroudas has shown via the fixed charged density that the GAG content is 40% of that found in the middle zone [51]. Thus in this zone, the concentration of the PG aggregates are approximately 20mg/ml and the properties of the PG aggregate network are different from that in the deeper zones. From the viscoelastic measurements of Mow *et al* [69], the corresponding complex shear modulus is 1.1 N/m^2 and the tangent of the phase shift is 3, at 1 Hz. From Eqn 5.6, this gives an elastic modulus of 1.04 Pa for the PG network and a stiffness of 0.46×10^{-6} N/m for the entangled PG aggregate network embedded in the extant collagen network. Also with a lower PG concentration, the zero shear rate viscosity becomes 0.5 N

s/m^2 and the corresponding $b_{||}$ is 7.0 x 10^{-7} N s/m for the dissipative resistance to fiber motion.

In addition to these different PG network characteristics, the interstitial fluid velocity is also higher in this zone. With a surface displacement rate 1 μm/sec, the volume flow rate, V, of fluid expressed from a circular area of cartilage with radius, r, is πr^2 μm^3/sec, where r is in μm. Some of this expressed fluid will flow through the interarticular gap, but the rest will flow tangentially through the STZ where the cartilage permeability is lowest. Macirowski developed an FE model based on *in situ* measurements of cartilage geometry and constitutive properties in the hip joint, and showed that the conductance of the interarticular gap is less than 1/3 of the conductance through the tissue [46]. Therefore, 2/3 of this expressed fluid will flow tangentially through the STZ and the tangential velocity is given by:

$$v = \frac{V}{2\pi r d}\frac{2}{3} = \frac{r}{3d} \tag{5.11}$$

where, d is the depth of the STZ. From ultrasound geometrical measurments of cartilage in the human hip joint, the width of the contact area in the acetabulum is approximately 20 mm [94]. Thus, for a radius of 10 mm and a STZ depth of 100 μm [59], the tangential velocity is approximately 30 μm/sec. This tangential flow rate is just an average estimate, but the flow rates will have local variations due to the incongruency of the articulating surfaces [94], and so a more conservative flow rate of 5 μm/sec and a corresponding drag force of $F_{\perp}$ = 1.15 x 10^{-14} N (Eqn 5.4) was used for model simulations

Using these estimated parameter values for the STZ, the orientation of loose collagen fibrils in cartilage ECM was simulated using the discreet time dependent model. The resulting predicted path and orientation is shown in Figure 5.19 and 5.20.

Thus, the discreet time dependent model, with even the extremely retarded motion calculated from viscosity measurement on PG aggregate solutions, predicts that loose collagen fibrils in the STZ will become oriented within an hour under a constant drag force produced by physiological interstitial tangential flows.

All of the above discussion and simulations were conducted with drag forces produced by constant flow. However, under the activities of daily life, the articular cartilage in the joint is subjected to cyclical loads, and hence the drag forces and fluid flows are cyclical. Sufficient time was not available to develop a discreet time dependent cyclically loaded model. Nevertheless, some characteristics of the cyclical reponse from such a model can be inferred

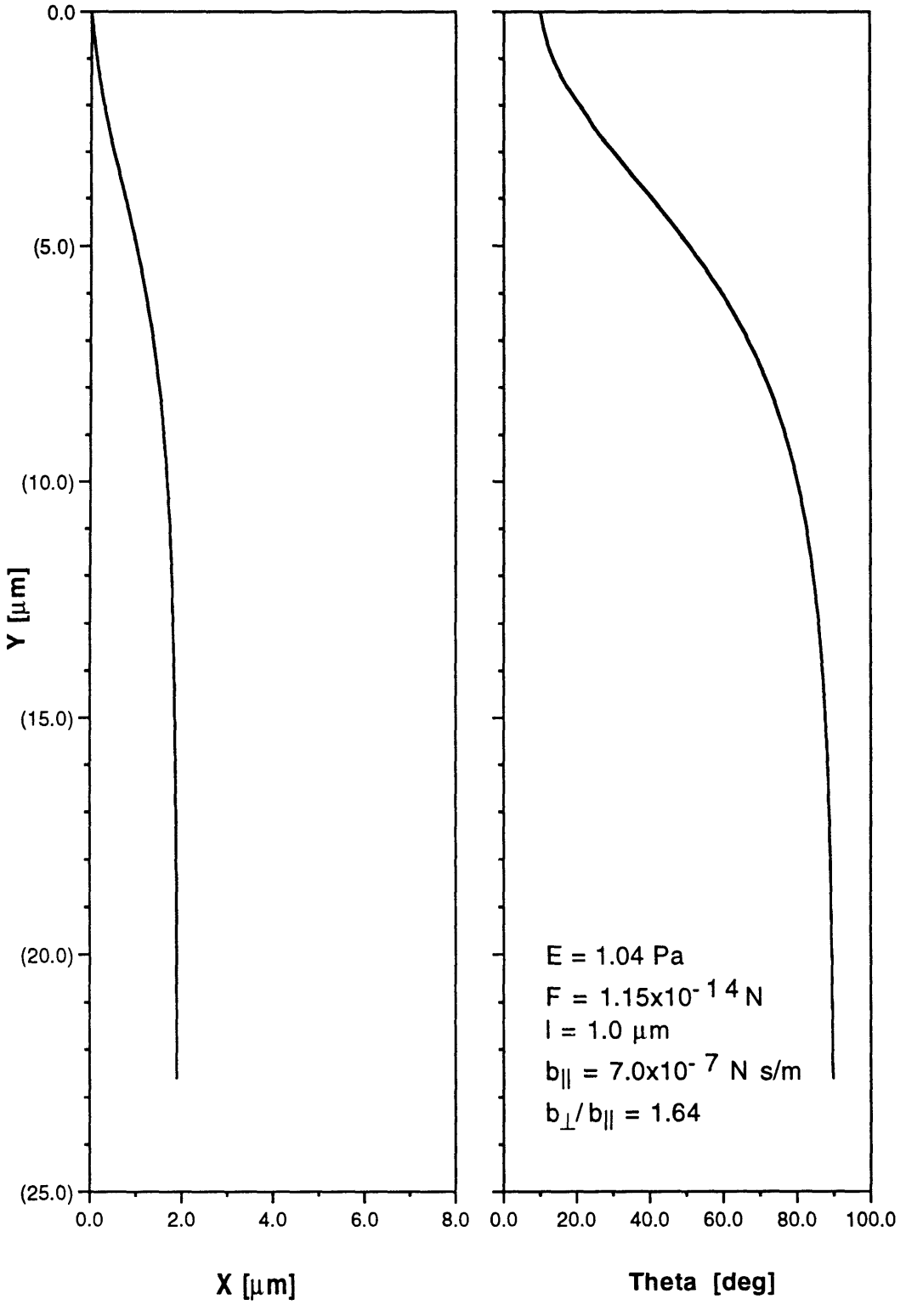

Figure 5.19 Discreet Time Dependent Model Predicted Path of the Loose Collagen Fibril in the Superficial Tangential Zone of cartilage ECM.

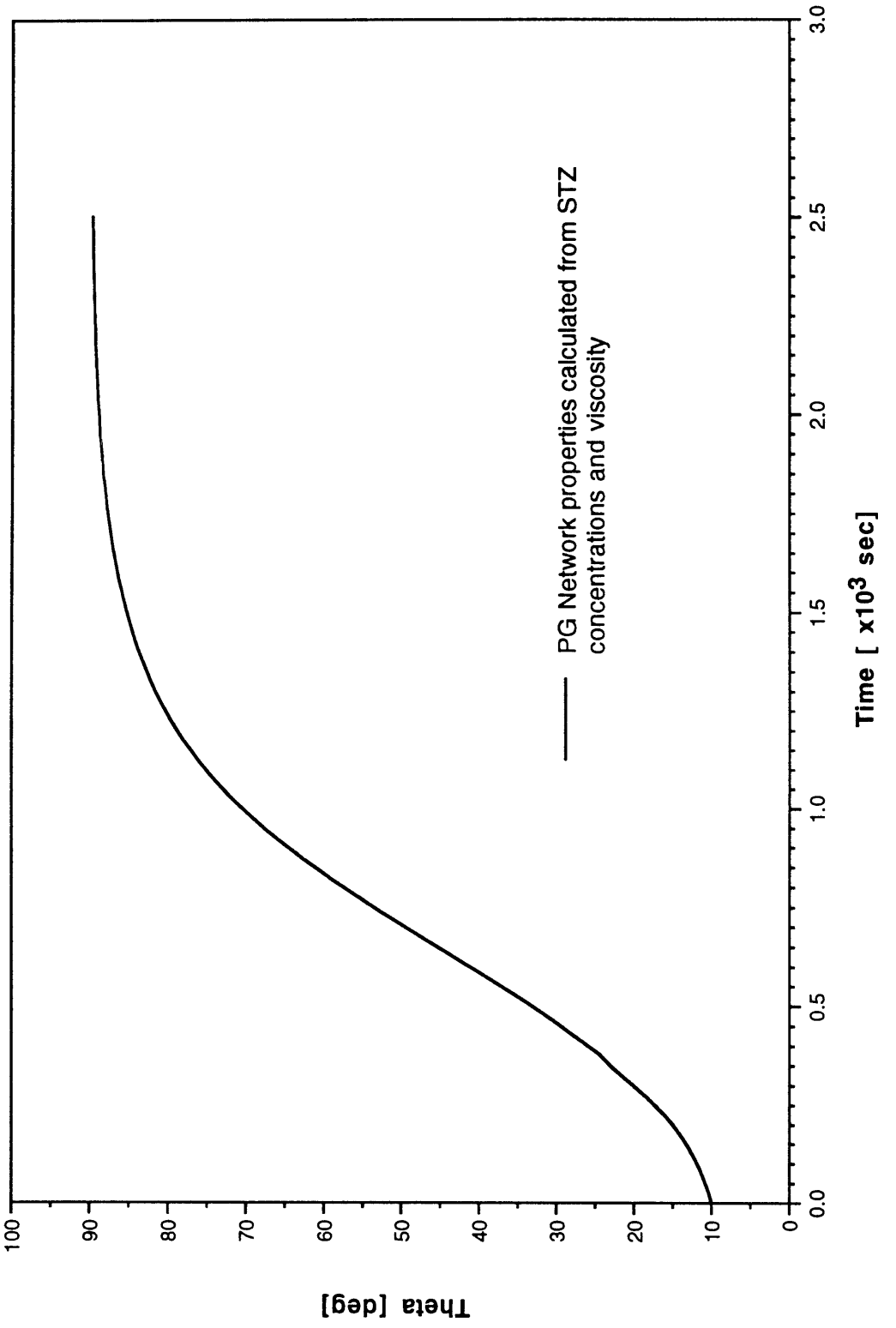

Figure 5.20 Discreet Time Dependent Model Predicted Orientation of the Loose Collagen Fibril in the Superficial Tangential Zone of cartilage ECM (dissipative properties of PG network calculated from viscosity of PG Aggregate Solution).

from the step load response. Under a step load, the predicted translational movement of the fibril can be up to 0.6 mm for flow rates of 1 μm/sec (Figure 5.16) and 23 μm for flow rates of 5 μm/sec in the STZ (Figure 5.19). These considerable movements are rather unlikely, but under cyclical loading, the fiber would be dragged to and fro, gradually orienting, but not translating significantly. Of course, the average intensity of the flow would also be decreased with cyclical loads and the orientation would require more time, but for sinusoidal flow cycles, the intensity would only decrease by one half, and the fibril should become oriented within 24 hr. Finally, in the discreet time dependent model, the relaxation of the proteoglycan network was neglected, but since the motion of the fibril is driven by a load input there will always a portion of the network directly under the fibril which is elastically deformed, but as the cyclical motion decreases in frequency, the PG network is allowed to relax, and the elastic nature of the network diminishes. This change in the elastic nature of the PG network with frequency was compensated for by calculating the elastic nature of the PG network from the complex shear modulus and phase shift at 1 Hz, the physiological loading rate.

5.5 CONCLUSIONS

A model was developed to examine the potential of the hypothesis that loose collagen fibrils formed within the entangled molecular network of PGs in cartilage ECM may become oriented by the drag force which is produced from interstitial fluid flows which are a result of joint loading. It was beyond the scope of this thesis to determine both the necessary physical relationships and the parameter values required for the mechanism to function in cartilage. Hence the necessary physical relationships were incorporated into models of increasing complexity, until a model was developed which could simulate the drag induced orientation mechanism for a variety of gel-like media. Then, the complete model was used with physiological parameter values estimated from known literature values and the isolation of loose collagen fibrils described earlier in this document to examine the potential of the mechanism in cartilage.

First quasi-static FE and discreet models were developed to investigate the importance of the elastic nature of the network to the orientation mechanism. It was found that although the stiffer network provided increased turning moments with less translation perpendicular to the fiber axis, the fiber required increased translation parallel to its axis in order to become oriented. Next dissipative resistances were incorporated into the discreet model, to simulate the time dependent nature of the orientation mechanism. This model was shown as sufficient

to simulate both motion of a fiber in a viscous liquid and the motion of a steel fiber in a 1% gelatine gel.

Finally, the discreet time dependent model was used to simulate a drag induced orientation mechanism for loose collagen fibrils in cartilage ECM. The geometrical dimensions of the loose collagen fibril were taken from the isolated collagen fibrils presented in Chapter 4. The drag forces were calculated by estimating the flow rates from roentographic and ultrasound measurements of *in vitro* loaded hip joints and applying these flow rates to the theory of low Reynolds number flow around a finite length cylinder. The properties of the entangled PG network were estimated from rheological measurements of near physiological concentration PG aggregate solutions and a FE model of such a PG network entangled in the extant collagen network of cartilage ECM. The dissipative resistance to motion of the fiber was calculated from two different physical interpretations. One set of parameter values were estimated from the retardation constant of PG aggregate solutions and the other set from the viscosity of the same solutions. The parameter values calculated from these two conditions represent the two extremes of the range, and the investigation of Laurent of the transport of rigid linear particles in hyaluronate indicate that the actual parameters value are within this range.

For the parameter values calculated from the retardation time constant, the model predicted that the loose collagen fibril would become oriented by this mechanism under a constant drag force resulting from a fluid flow rate of 1 μm/sec anywhere in the articular cartilage ECM. For the parameter values calculated from viscosity, the model predicted that the loose collagen fibril would become oriented by this mechanism under a constant drag force resulting from a tangential fluid flow rate of 5 μm/sec only in the superficial tangential zone of articular cartilage. Although the physiological flow rates are cyclic in nature, the results of the model are still relevant. The actual translation of the fibrils would be decreased and the turning rate would also be decreased compared with a constant load. However, the turning rates are still sufficient to orient the fibril within 24 hr. Thus, the drag induced orientation mechanism has the potential to orient loose collagen fibrils in the superficial and possibly the middle zones of articular cartilage. In the deep zones of articular cartilage, the flow velocity are do not appear sufficient for such an orientation mechanism to function, and the radial orientation of the large fibrils observed in this zone may be a result of tissue growth rather than active organization.

CHAPTER
SIX

CONCLUSIONS

6.1 REVIEW

This thesis has covered many topics and it is worth reviewing how these topics relate to the thesis' objectives and conclusions. Cartilage provides lubricated surfaces for load transmission in synovial joints. This structural function is dependent on the mechanical properties of its ECM. The ECM is a poroelastic material with a solid organic matrix, composed of a fine molecular scale network of entangled PG aggregates, embedded and possibly bound to a coarser network of collagen fibrils, swollen in ionized aqueous fluid. Individually, the PGs resist compressive deformations, and the collagen fibrils exhibit a significant tensile strength, but since the PG's are embedded within the collagen network, the collagen network and the orientation of the fibrils within the network contribute to all mechanical properties of cartilage. However, the physiological mechanisms which establish and maintain the individual collagen fibril orientation within a highly organized fibrous framework of normal cartilage are mostly unknown.

To date, the prevalent approach to this problem in biomechanics has been teleological in nature. The apparently optimal structure of load bearing tissues have been well studied, and the stress distribution within the ECM appears to satisfy a possible criteria which matches the architecture of collagen in cartilage. Although this criterion is important, unless the

mechanism can be understood, it is difficult to apply. While a biological system may normally function governed by some optimization principle, interventions for treatment of pathological conditions may be misguided by applications of this principle. Thus understanding of collagen fibril orientation mechanisms is prerequisite to a rational approach to controlling the process of cartilage repair. Although understanding of such a mechanism is no guarantee for success, no scientific approach is possible without it.

Since cartilage is poroelastic, loading it entails fluid movement as well as deformation. In this thesis, it is proposed that collagen orientation is induced by fluid movement, and two novel mechanisms are presented: (i) orientation of collagen fibrils induced by their movement through the gel-like medium of the fluid-saturated PG network, (ii) orientation of collagen fibrils by flow-induced interstitial fluid shear fields. In the former, orientation arises through the elastic interaction of the fibril and the PG network, while the driving force is the viscous drag of the fluid against the fibril (drag induced orientation, DO). In the latter, although global tissue flows do not generate shear fields of sufficient intensity, flow channels created through the process of flow-induced PG network disentanglement could generate local collagen-network-scale velocity gradients (shear flow induced orientation, SFO).

Since, present knowledge of the physical properties and interactions among the ECM components are insufficient, and their determination is not within the scope of this thesis, undeniable demonstration of these hypotheses is not possible. Nevertheless, evidence for both hypotheses were examined and their mechanistic potentials were demonstrated. From the experiments and the development of models, several conclusions and suggestive results have been uncovered that were not previously known or understood.

6.2 CONCLUSIONS

6.2.1 ISOLATION OF LOOSE COLLAGEN FIBRILS IN CARTILAGE ECM

In both hypotheses, the orientation of the collagen fibrils within the network is a result of the orientation of smaller loose collagen fibril building units which assemble into larger fibrils after orientation and become incorporated into the extant network. In this thesis, a new technique was developed to isolate these collagen filaments. In this technique, the PGs were digested from cartilage explants, and the collagen filaments were washed out of the explant by irrigation in a liquid chromatography apparatus.

1) The presence of tapered ends on mature banded fibrils of Ø40 nm and the presence of fibrils with diameters varying by as much as 4 times indicate that these mature fibrils are in the process of growth, both lengthwise and diametrically, and that these fibrils may have at least one loose end in the ECM.

2) Ø10.4 ± 0.5 nm x 1.06 ± 0.03 μm filaments were observed in the irrigation fluid. These unbanded filaments were similar to those isolated from chick embryo sterna, and were larger than the multimolecular SLS-units observed previously. Although no immunolabelling was conducted (due to technical reasons), it is hard to imagine that any macromolecular substance with this structure, other than collagen, could exist in cartilage.

6.2.2 SHEAR FIELD INDUCED ORIENTATION

Orientation of fibers suspended in fluid under shear has been analyzed first by Jeffrey and later by Forgacs and Mason. The global shear fields produced by the fluid flow between opposing layers of cartilage have been studied and found to be of low intensity and not corresponding to observed patterns of collagen orientation [95]. However, possibility of transport of larger molecules through the ECM of cartilage under cyclical load has led to the proposal that a few larger openings or channels may form through the PG network. These channels would then create local shear fields which could orient loose collagen fibrils. The investigations pertaining to this hypothesis centered on the detection of these channel formation.

1) High pressure freezing, freeze substitution, and conventional embedding was investigated as a method of studying PG ultrastructure within the intact cartilage ECM. It was found by comparison to electron diffraction on cryosections that the traditional criteria of a non-segregated nucleus for the determination of adequate cryoimmobilization was inadequate for cartilage whose matrix contains up to 80% water by weight. The ECM was found to be a more sensitive indicator for ice crystal formation, but without detection by electron diffraction, it is difficult to distinguish between the PG network and ice crystal segregation patterns.

2) Acetone freeze substitution was found to preserve finer details of the PG network over freeze substitution with methanol. This was believed to be due to the more aggressive nature of substitution for water by methanol over that by acetone. Although no

immunostaining was conducted, distinctive structures similar to isolated PG aggregates by the Kleinschmidt technique were evident.

3) Using the methods of preparation developed for the study of PG ultrastructure, specimens were osmotically compressed and allowed to freely imbibe colloidal solutions of Ø11 nm BSA coated gold particles or Ø12 nm ferritin particles. No channels or larger pore formations were observed under examination by TEM. However, these cartilage specimens were only exposed to one cycle of loading, and channel formation may occur under prolonged cyclical loading as experienced during physiological activities.

4) Experimental creep consolidation of cartilage in both compression and imbibing modes were compared to various physical models of cartilage. The general response of cartilage was found to be well modeled by the simple linear gel diffusion theory model. However, two different constant value permeabilities are required to model both the compression and imbibing creep behavior, and since no differences exist in the physical interaction of the ECM components for these two creep situations, constant permeability and stiffness are insufficient to describe the poroelastic response of cartilage.

5) Various strain dependent permeability functions, consistent with those used by other investigators, were incorporated into the linear lumped parameter model, and found to correctly simulate the compression or imbibing creep behavior, but not both. Regardless of the permeability function, strain dependent permeability alone (decreasing permeability with increasing compressive strain) could not account for the imbibing and compression creep behavior differences observed experimentally. Furthermore, models with strain dependent permeability alone predicted creep response differences opposite to those experimentally observed.

6) Since no experimental evidence necessitated a linear stiffness at low compressive strains and non-linear stiffness functions were shown to describe the entire range of compressive strains, a linear strain dependent permeability function and a hyperbolic strain dependent equilibrium modulus were incorporated into the linear lumped parameter model. The parameter values for the stiffness function was then optimized to match the experimental creep data for both imbibing and compression. It was found that this model correctly simulates the creep response of cartilage, and with one set of parameter values describing the interaction of fluid and the poroelastic material, predicts the differences between compression and imbibing creep observed experimentally.

7) Velocity dependent permeability was not observable in the experimentally measured creep responses. Because the mean error of the k (ε) & L (ε) optimized lumped parameter model simulations compared to the experimental data was only 1.45 ± 0.16 μm, and the resolution of the experimental measurements is only 2.0 μm, it was impossible to detect any decrease in permeability with increased interstitial fluid velocity by comparison of experimental data to simulations of a velocity dependent permeability model.

6.2.3 DRAG INDUCED ORIENTATION

To determine the potential of drag induced orientation for the loose collagen fibril isolated above in cartilage, various models of increasing complexity were developed to understand the important physical relationships necessary for the general mechanism in gel-like media.

1) A discreet model was developed to investigate the importance of the elastic nature of the network to the orientation mechanism. It was found that although the stiffer network provided increased turning moments with less translation perpendicular to the fiber axis, the fiber required increased translation parallel to its axis in order to become oriented.

2) Dissipative resistances were incorporated into the discreet model, to simulate the time dependent nature of the orientation mechanism. This model was shown as sufficient to simulate both motion of a fiber in a viscous liquid and the motion of a steel fiber in a 1% gelatin gel.

3) The discreet time dependent model was used to simulate drag induced orientation mechanism for loose collagen fibrils in cartilage ECM. Dimensions of the loose collagen fibril measured earlier and experimentally measured parameter values in the literature were used to calculate the values of the required parameters. Using the parameter values calculated from the retardation time constant of PG solutions, the model predicted that the loose collagen fibril would become oriented by this mechanism under a constant drag force resulting from a fluid flow rate of 1 μm/sec in the general articular cartilage ECM. Using the parameter values calculated from viscosity, the model predicted that the loose collagen fibril would become oriented by this mechanism under a constant drag force resulting from a tangential fluid flow rate of 5 μm/sec only in the superficial tangential zone of articular cartilage. Although under physiological cyclic flows, translation and turning rates are decreased, they are still sufficient to orient the fibril within 24 hr. Thus, the drag induced orientation mechanism has the potential to orient loose collagen fibrils in the superficial and possibly the middle zones of articular cartilage.

6.3 FUTURE WORK

In this thesis, two hypotheses for the orientation mechanism of collagen fibrils in the ECM of cartilage were presented. Both cases involved the orientation of a loose collagen fibril by its physical interaction with the ECM, before assembly with other oriented fibrils and incorporation into the extant collagen network. Although these fibril building blocks were isolated, the problems associated with the isolation of the loose collagen fibrils by irrigation of the partially PG digested cartilage explant plugs should be resolved. The apparatus should be redesigned to provide consistent irrigation of the tissue. Once the filaments can be isolated, monoclonal antibodies for type II collagen should be used to identify these structures.

The shear field induced orientation mechanism was not validated by the presence of any shear field creating channels within the PG network, but this mechanism has also not been eliminated as a potential orientation mechanism. It is still possible that the formation of channels requires prolonged cyclical loading, like that seen under physiological conditions. The imbibing of particles should be conducted under cyclical loading conditions and with various size particles and controls to determine the distribution of pore sizes in the cartilage ECM.

The creep response measurements also did not support the contention that channels may open. However, they did demonstrate the need to include strain dependent equilibrium modulus of cartilage if high strain response (> 10%) is to be modelled completely. It was shown that previous investigations where model parameters were optimized to only consolidation data is not sufficient for creating a consistent model of complete cartilage poroelastic behavior. For a more complete model with strain dependent permeability and equilibrium modulus, more stiffness and creep response measurements are required for the same cartilage plugs.

Finally, the potential of the drag induced orientation mechanism was exhibited by development of a model. Although, the exact parameter values were estimated from literature values, the range of possibilities were examined and the possibility of the mechanism was shown for the most stringent conditions in the cartilage STZ. Some transport experiments in cartilage ECM should be conducted with radiolabelled fibrils to measure exactly these values and to validate the model. Furthermore, the cyclical model should also be developed and validated. In addition to completing the modeling, the drag-induced mechanism should be validated *in vitro* in organ culture or *in vivo* under controlled conditions. Then we can start to

develop rational approaches for controlling the repair environment of cartilage in order to foster the appropriate collagen architecture and proper repair.

BIBLIOGRAPHY

[1] Armstrong, C.G., A.S. Bahrani, and M.A. Gardner, In vitro measurement of articular cartilage deformations in the intact human hip joint under load. *J. Bone Joint Surg.*, **61A**:p.744-755, 1979.

[2] Arsenault, A.L., F.P. Ottensmeyer, and I.B. Heath, An electron microscopic and spectroscopic study of murine epiphyseal cartilage analysis of fine structure and matrix vesicles preserved by slam freezing and freeze substitution. *J. Ultrastruct. Mol. Struct. Res.*, **98**(1):p.32-47, 1988.

[3] Athianasiou, K.A., *et al.*, Interspecies comparisons of in situ intrinsic mechanical properties of distal femoral cartilage. *J. Orthop. Res.*, **9**:p.330-340, 1991.

[4] Baer, E., J.J. Cassidy, and A. Hiltner, Heirarchical structure of collagen and its relationship to the physical properties of tendon. In *Collagen,* M.E. Nimni, ed(s). Boca Raton, FL, CRC Press Inc., 1988, p.177-199.

[5] Birk, D.E. and R.L. Trelstad, Extracellular compartments in matrix morphogenesis: collagen fibril, bundle, and lamellar formation by corneal fibroblasts. *J. Cell Biol.*, **99**:p.2024, 1984.

[6] Birk, D.E. and R.L. Trelstad, Extracellular compartments in tendon morphogenesis: collagen fibril, bundle, and macroaggregate formation. *J. Cell Biol.*, **103**:p.231-240, 1986.

[7] Birk, D.E., *et al.*, Collagen fibrillogenesis in situ: fibril segments are intermediates in matrix assembly. *Proc. Natl. Acad. Sci. U.S.A.*, **86**:p.4549-4553, 1989.

[8] Bradley, S.P., A.C. Hax, and T.L. Magnanti, *Applied Mathematical Programming*, Boston, MA, Addison-Wesley, 1977.

[9] Bruckner, P., *et al.*, Induction and prevention of chondrocyte hypertrophy in culture. *J. Cell Biol.*, **109**:p.2537-2545, 1989.

[10] Bruns, R.R., *et al.*, Procollagen segment-long-spacing crystallites: their role in collagen fibrillogenesis. *Proc. Natl. Acad. Sci. U.S.A.*, **76**:p.313, 1979.

[11] Bullough, P. and J. Goodfellow, The significance of the fine structure of articular cartilage. *J. Bone Joint Surg.*, **50B**:p.852, 1968.

[12] Chandler, J., Personal Communication, 1993.

[13] Chen, K. and T.N. Wight, Proteoglycans in arterial smooth muscle cell cultures: an ultrastructural histochemical analysis. *J. Histochem. Cytochem.*, **32**:p.347-357, 1984.

[14] Chun, L.E., T.J. Koob, and D.R. Eyre, Sequential enzymatic dissection of the proteoglycan complex from articular cartilage. In *Trans. 32nd Annual Meeting of the Ortho. Res. Society*, 1986:p.96.

[15] Clarke, I.C., Articular cartilage: a review and scanning electron microscope study. *J. Anat.*, **118**:p.216-280, 1974.

[16] Cox, R.G., The motion of long slender bodies in a viscous fluid part I: general theory. *J. Fluid Mech.*, **44**:p.791-810, 1970.

[17] Dubochet, J., *et al.*, Cryo-electron microscopy of vitrified specimens. *Quart. Rev. of Biophys.*, **21**:p.129-228, 1988.

[18] Edelmann, L., Adsorption staining of freeze substituted and low temperature embedded frog skeletal muscle with cesium: A new method for the investigation of protein-ion interactions. *Scanning Microscopy*, **Suppl. 5**:p.S75-S84, 1991.

[19] Engfeldt, B. and S.-O. Hjertquist, Studies on the epiphyseal growth zone I. The preservation of acid gycosaminoglycans in tissues in some histochemical procedures for electron microscopy. *Virchows Arch. Abt. B. Zellpath.*, **1**:p.222-229, 1968.

[20] Engfeldt, B., *et al.*, Ultrastructure of hypertrophic cartilage - histochemical procedures compared with high pressure freezing and freeze substitution. *to be submitted for publication*, 1993.

[21] Fleischmajer, R., *et al.*, Regulation of collagen fibril formation. In *49th Annual Scientific Meeting of the American Rheum. Assoc.*, Anaheim, CA, 1985.

[22] Forgacs, O.L. and S.G. Mason, Particle motions in sheared suspensions, IX: spin and deformation of threadlike particles. *J. Colloid Sci.*, **14**:p.457-472, 1959.

[23] Frank, E.H. and A.J. Grodzinsky, Cartilage electromechanics II: a continuum model of cartilage electrokinetics and correlation with experiments. *J. Biomech.*, **20**(6):p.629-639, 1987.

[24] Handley, P.A., J.T. Alexander, and S. Chien, The design and use of a simple device for rapid quench-freezing of biological samples. *J. Microscopy*, **121**(3):p.273-282, 1981.

[25] Happel, J. and H. Brenner, *Low Reynolds Number Hydrodynamics,* Den Hague, Martinus Nijhoff, 1983.

[26] Hardingham, T.E., *et al.*, Viscoelastic properties of proteoglycan solutions with varying proportions present as aggregates. *J. Orthop. Res.*, **5**:p.36-46, 1987.

[27] Hascall, G.K., Cartilage proteoglycans: comparison of sectioned and spread whole molecules. *J. Ultrastruct. Res.*, **70**(3):p.369-375, 1980.

[28] Hascall, V.C. and G.K. Hascall, Proteoglycans. In *Cell Biology of Extracellular Matrix,* E.D. Hay, ed(s). N.Y., Plenum Press, 1981, p.39-63.

[29] Hayes, W.C., *Mechanics of Human Articular Cartilage*. Ph.D., Northwestern Univeristy, 1970.

[30] Heinegård, D. and Å. Oldberg, Structure and biology of cartilage and bone matrix noncollagenous macromolecules. *FASEB J*, **3**:p.2042-2051, 1989.

[31] Heuser, J.E., *et al.*, Synaptic vesicle exocytosis captured by quick freezing and correlated with quantal transmitter release. *J. Cell Biol.*, **81**:p.275-300, 1979.

[32] Hodge. W.A., *et al.*, Contact pressures from an instrumented hip prosthesis. *J Bone Joint Surg.*, **71A**:p.1378-1386, 1989.

[33] Humbel, B.M. and M. Müller, Freeze substitution and low temperature embedding. In *The Science of Biological Specimen Preparation,* M. Müller, *et al.*, ed(s). AMF, O'Hare, IL, SEM Inc., 1986, p.175-183.

[34] Hunziker, E.B. and W. Hermann, In situ localization of cartilage extracellular matrix components by immunoelectron microscopy after cryotechnical tissue processing. *J. Histochem. Cytochem.*, **35**:p.647-655, 1987.

[35] Hunziker, E.B., W. Hermann, and R.K. Schenk, Improved cartilage fixation by ruthenium hexaamine trichloride (RHT). A prerequisite for morphometry in growth cartilage. *J. Ultrastruc. Res.*, **81**:p.1-12, 1982.

[36] Hunziker, E.B., *et al.*, Cartilage ultrastructure after high pressure freezing, freeze substitution, and low temperature embedding. I. Chondrocyte ultrastructure - implications for the theories of mineralization and vascular invasion. *J. Cell Biol.*, **98**(Jan.):p.267-276, 1984.

[37] Hunziker, E.B., A. Ludi, and W. Hermann, Preservation of cartilage matrix proteoglycans using cationic dyes chemically related to ruthenium hexamine trichloride. *J. Histochem. Cytochem.*, **40**:p.909-917, 1992.

[38] Hunziker, E.B. and R.K. Schenk, Cartilage ultrastructure after high pressure freezing, freeze substitution, and low temperature embedding. II. Intercellular matrix

ultrastructure - preservation of proteoglycans in their native state. *J. Cell Biol.*, **98**(1):p.277-82, 1984.

[39] Jeffrey, G.B., *Proc. Royal Soc. (London)*, **A102**:p.161, 1922.

[40] Kadler, K.E., Y. Hojima, and D.J. Prockop, Collagen fibrils in vitro grow from pointed tips in the C- to N-terminal direction. *Biochem. J.*, **268**:p.339-343, 1990.

[41] Lai, W.M. and V.C. Mow, Drag-induced compression of articulat cartilage during a permeation experiment. *Biorheology*, **17**:p.111-123, 1980.

[42] Laurent, T.C., *et al.*, *Biochim. Biophys. Acta*, **78**:p.351-359, 1963.

[43] Laurent, T.C., *et al.*, Diffusion of linear polymers in hyaluronate solutions. *Eur. J. Biochem.*, **53**:p.129-136, 1975.

[44] LeBlond, C.P. and G.M. Wright, Steps in the elaboration of collagen by odontoblasts and osteoblasts. In *Methods in Cell Biology,* A.R. Hand and C. Oliver, ed(s). New York, Academic Press Inc., 1981, p.167-189.

[45] Luft, J.H., Ruthenium red and violet. I: Chemistry, purification, methods of use for electron microscopy and mechanism of action. *Anat. Rec.*, **171**:p.347-368, 1971.

[46] Macirowski, T., S. Tepic, and R.W. Mann, Cartilage stresses in the human hip joint. *J. Biomech. Engng.*, accepted for publ. 1994.

[47] Mansour, J.M. and V.C. Mow, The permeability of articular cartilage under compressive strain and at high pressures. *J. Bone Joint Surg.*, **58A**(4):p.509-516, 1976.

[48] Maroudas, A., Distribution and diffusion of solutes in articular cartilage. *Biophys. J.*, **10**:p.365-379, 1970.

[49] Maroudas, A., Balance between swelling pressure and collagen tension in normal and degenerate cartilage. *Nature*, **260**:p.808-809, 1976.

[50] Maroudas, A., Transport of solutes through cartilage: permeability to large molecules. *J. Anat.*, **122**:p.335-347, 1976.

[51] Maroudas, A., Physicochemical properties of articular cartilage. In *Adult Articular Cartilage,* M.A.R. Freeman, ed(s). Kent, U.K., Pitman Medical, 1979, p.215-290.

[52] Maroudas, A. and C. Bannon, Measurement of the swelling pressure in cartilage and comparison with osmotic pressure of constituent proteoglycans. *Biorheology*, **18**:p.619-632, 1981.

[53] Maroudas, A., *et al.*, The permeability of articular cartilage. *J. Bone Joint Surg.*, **50B**:p.166-177, 1968.

[54] Maroudas, A., H. Muir, and J. Wingham, The correlation of fixed negative charge with glycosaminoglycan content of human articular cartilage. *Biochim. Biophys. Acta*, **177**:p.492-500, 1969.

[55] Maroudas, A. and R. Schneiderman, "Free" and "exchangeable" or "trapped" and "non-exchangeable" water in cartilage. *J. Orthop. Res.*, **5**:p.133-138, 1987.

[56] Maroudas, A. and M. Venn, Swelling of normal and osteoarthrotic femoral head cartilage. *Ann. Rheum. Dis.*, **36**:p.399-406, 1977.

[57] McCutchen, C.W., Mechanism of animal joints. Sponge-hydrostatic and weeping bearings. *Nature*, **184**:p.1284-1285, 1959.

[58] McCutchen, C.W., The frictional properties of animal joints. *Wear*, **5**:p.1-17, 1962.

[59] Meachim, G. and R.A. Stockwell, The matrix. In *Adult Articular Cartilage,* M.A.R. Freeman, ed(s). Kent, U.K., Pitman Medical, 1979, p.1-50.

[60] Mendler, M., *et al.*, Cartilage contains mixed fibrils of collagen types II, IX, and XI. *J. Cell Biol.*, **108**:p.191-197, 1989.

[61] Michel, M., H. Gnägi, and M. Müller, Diamonds are a cryosectioner's best friend. *J. Microscopy*, **166**(1):p.43-56, 1992.

[62] Michel, M., T. Hillmann, and M. Müller, Cryosectioning of plant material frozen at high pressure. *J. Microscopy*, **163**(1):p.3-18, 1991.

[63] Moor, H., Theory and practice of high pressure freezing. In *Cryotechniques in Biological Electron Microscopy,* K. Zierol and R.A. Steinbrecht, ed(s). Berlin, Springer-Verlag, 1987, p.175-191.

[64] Moor, H. and U. Riehle, Snap-freezing under high pressure: A new fixation technique for freeze-etching. In *Proc. 4th Eur. Reg. Conf. Electron Microsc.*, Rome, 1968. Vol. 2:p.33-34.

[65] Mow, V.C., *et al.*, Biphasic indentation of articular cartilage II: a numerical algorithm and an experimental study. *J. Biomech.*, **22**(8/9):p.853-861, 1989.

[66] Mow, V.C., M.H. Holmes, and W.M. Lai, Fluid transport and mechanical properties of articular cartilage: a review. *J. Biomech.*, **17**:p.377, 1984.

[67] Mow, V.C., *et al.*, Biphasic creep and stress relaxation of articular cartilage in compression: theory and experiments. *J. Biomech. Engng.*, **102**:p.73-84, 1980.

[68] Mow, V.C. and W.M. Lai, Mechanics of animal joints. *Ann. Rev. Fluid Mech.*, **11**:p.247-288, 1979.

[69] Mow, V.C., A.F. Mak, and W.M. Lai, Viscoelastic properties of proteoglycan subunits and aggregates in varying solution concentrations. *J. Biomech.*, **17**(5):p.325-338, 1984.

[70] Muir, H., The chemistry of the ground substance of joint cartilage. In *The Joints and Synovial Fluid,* L. Sokoloff, ed(s). N.Y., Academic Press, 1980, p.27-94.

[71] Müller, M., N. Meister, and H. Moor, Freezing in a propane jet and its application in freeze fracturing. *Mikroscopie*, **36**:p.129-140, 1980.

[72] Nimni, M.E., Molecular structure and function of collagen in normal and diseased tissues. In *Dynamics of Connective Tissue Macromolecules,* P.M. Burleigh and A.R. Poole, ed(s). New York, American Elsevier, 1975, p.33-79.

[73] O'Conner, P., C. Bland, and D.L. Gardner, Fine structure of artificial splits in femoral condylar cartilage of the rat: a scanning electron microscopic study. *J. Path.*, **132**:p.169-179, 1980.

[74] O'Hara, B.P., J.P.G. Urban, and A. Maroudas, Influence of cyclical loading on the nutrition of articular cartilage. *Ann. Rheum. Dis.*, **49**:p.536-539, 1990.

[75] Ogston, A.G., B.N. Preston, and J.D. Wells, *Proc. Royal Soc. (London)*, **A333**:p.297-309, 1973.

[76] Orkin, R.W., R.M. Pratt, and G.R. Martin, Undersulfated chondroitin sulfate in the cartilage matrix of brachymorphic mice. *Develop. Biol.*, **50**(1):p.82-94, 1976.

[77] Pauwels, F., *Biomechanics of the Locomotor Apparatus,* Berlin, Springer-Verlag, 1980.

[78] Press, W.H., *et al.*, *Numerical Recipes in C. The Art of Scientific Computing,* Cambridge, Cambridge University Press, 1990.

[79] Reynolds, E., The use of lead citrate at high pH as an electron-opaque stain in electron microscopy. *J. Cell Biol.*, **17**:p.208-212, 1963.

[80] Rosenberg, L.C., W. Hellman, and A.K. Kleinschmidt, Electron microscopic studies of proteoglycan aggregates from bovine articular cartilage. *J. Biol. Chem.*, **250**:p.1877-1883, 1975.

[81] Roth, V. and V.C. Mow, The intrinsic tensile behavior of the matrix of bovine articular cartilage and its variation with age. *J. Bone Joint Surg.*, **62A**:p.1102-1117, 1980.

[82] Roux, W., Beitrag für morphologie der funktionellen anpassung. 3. Beschriebung und erlauterung einer knochernen kniegelenksankylose. *Archiv. Anat. Phys. Wissensch. Med.*, :p.pp120-158, 1885.

[83] Sauren, Y.M.H.F., *et al.*, Polyethyleneimine as a contrast agent for ultrastructural localization and characterization of proteoglycans in the matrix of cartilage and bone. *J. Histochem. Cytochem.*, **39**(3):p.331-340, 1991.

[84] Scott, J.E., Proteoglycan - collagen interactions. In *Ciba Foundation Symposium*, 1986. Vol. 124:p.104-116.

[85] Shepard, N. and N. Mitchell, Ultrastructural modifications of proteoglycans coincident with mineralization in local regions of rat growth plate. *J. Bone Joint Surg.*, **67A**(3):p.455-464, 1985.

[86] Singer, S.J. and A.F. Schick, The properties of specific stains for electron microscopy prepared by the conjugation of antibody molecules with ferritin. *J. Biophys. Biochem. Cyt.*, **9**:p.519-537, 1961.

[87] Skerry, T.M., *et al.*, Load-induced proteoglycan orientation in bone tissue in vivo and in vitro. *Calcified Tissue Int.*, **46**:p.318-326, 1990.

[88] Snowden, J. and A. Maroudas, The ditribution of serum albumin in human normal and degenerate cartilage. *Biochim. Biophys. Acta*, **428**:p.726-, 1976.

[89] Stopak, D., N.K. Wessells, and A.K. Harris, Morphogenetic rearrangement of injected collagen in developing chiken limb buds. *Proc. Natl. Acad. Sci. U.S.A.*, **82**:p.2804-2808, 1985.

[90] Studer, D., M. Michel, and M. Müller, High pressure freezing comes of age. *Scanning Microscopy*, **Suppl. 3**:p.S253-S269, 1989.

[91] Tanaka, T. and D.J. Fillmore, Kinetics of swelling gels. *J. Chem. Phys.*, **70**:p.1214, 1979.

[92] Taylor, G.I., Motion of axisymmetric bodies in viscous fluids. In *Problems of Hydrodynamics and Continuum Mechanics*. Philadelphia, SIAM, 1969, p.718-724.

[93] Tepic, S., *Congruency of the human hip joint*. M.S., Massachusetts Institute of Technology, 1980.

[94] Tepic, S., *Dynamics of and entropy production in the cartilage layers of the synovial joint*. Sc.D., Massachusetts Institute of Technology, 1982.

[95] Tepic, S., Personal Communication, 1990.

[96] Thyberg, J., S. Lohmander, and U. Friberg, Electron microscopic demonstration of proteoglycans in guinea pig epiphyseal cartilage. *J. Ultrastruc. Res.*, **45**:p.407-427, 1973.

[97] Timnoshenko, S.P. and J.N. Goodier, *Theory of Elasticity*, 3rd ed. N.Y., McGraw-Hill, 1970.

[98] Tomlinson, N. and A. Maroudas, The effect of cyclic and continuous compression on the penetration of large molecules into articular cartilage. *J. Bone Joint Surg.*, **B62**(2):p.251, 1980.

[99] Vanderplaats, G.N., *Numerical Optimization Techniques for Engineering Design: with Applications*, N.Y., McGraw-Hill, 1984.

[100] Venn, M. and A. Maroudas, Chemical composition of normal ans osteoarthrotic femoral head cartilage. *Ann. Rheum. Dis.*, **36**:p.121-129, 1977.

[101] Wolff, J., *The Law of Bone Remodelling,* Berlin, Springer-Verlag, 1986.

[102] Woo, S.L.-Y., W.H. Akeson, and G.F. Jemmott, Measurement of nonhomogeneous directional mechanical properties of articular cartilage. *J. Biomech.*, **9**:p.785-791, 1976.

```
/* Initialize */

x_l = 0.0;
y_l = 0.0;

/* Read in parameter values */

printf(" Ratio of Delta/Length?: ");
scanf("%f", &delta_l);
printf(" Length?: ");
scanf("%f", &length);
printf(" Inital Theta?: ");
scanf("%f", &old_theta);

printf ("Output file name?: ");
scanf ("%s", out_file_name);
while((out_file = fopen (out_file_name, "w")) == NULL)
  {
  printf ("*** %s could not be opened. ***\n", out_file_name);
  printf ("Output file name?: ");
  scanf ("%s", out_file_name);
  }
fprintf(out_file,"Theta [deg]\tX [length]\tY [length]\n");

theta = old_theta/180*PI;
old_theta = theta - 1.0;

force_k = cos(theta)*delta_l*SQR(length);

/* Set inital conditions */

for(i=1;i<=N;i++) {stress_k[i] = force_k/length;}
old_theta = -0.1;
do
  {
  if ((theta -old_theta)  > 8.72e-2)
    {
    fprintf(out_file,"%e\t%e\t%e\n",theta*180.0/PI,x_l,y_l);
    printf("%10.6f %10.6f %10.6f \n"
     ,theta*180.0/PI,x_l,y_l);
    old_theta = theta;
    }

  /* slip fiber */

  stressn_k[1] = 0.0;
  for(i=2;i<=N;i++)
    stressn_k[i] = stress_k[i-1];

  x_l += 1.0/N*cos(theta);
  y_l += 1.0/N*sin(theta);

/* turning */

  moment_k = 0.0;
  for(i=1;i<=N;i++)
    moment_k += (-length/2.0 + length/N/2 + length/N*(i-1))
     *stressn_k[i]*length/N;
```

APPENDIX A

DISCREET MODEL

```
/*
  This program numerically simulates a discreet model of movement
  induced orientation of a massless rigid fiber moving in a elastic media.

  1) Given parameter values, a 4th order Runga-Kutta integrator is run to
     numerically simulate a set of ODE's.
*/

#include <stdio.h>
#include <math.h>
#include"nr.h"
#include "nrutil.h"

#define PI 3.14159265
#define SQR(a) ((a)*(a))
#define CUBE(a) ((a)*(a)*(a))
#define N 100

main()
{
  int i;
  float *stress_k,*stressn_k,force_k,theta,moment_k;
  float length,sumn_k,dtheta;
  float x_l,y_l,old_theta,delta_l;

  char out_file_name[81];
  FILE *out_file, *fopen();

  /* Allocate output space for integration */

  stress_k = vector (1,N);
  stressn_k = vector (1,N);
```

```
    dtheta = 12.0*moment_k/CUBE(length);

  /* new stress */

  /* due to turning */

    for(i=1;i<=N;i++)
    stressn_k[i] += (length/2.0 - length/N/2 -  length/N*(i-1))
       *dtheta;

  /* due to reduction in supporting stress */

    sumn_k = 0.0;
    for(i=1;i<=N;i++)
      sumn_k += stressn_k[i]*length/N;

    for(i=1;i<=N;i++)
      stressn_k[i] += (force_k-sumn_k)/length;

  /* Movement downward due to reduction in supporting stress */

    x_l -= sin(theta)*(force_k-sumn_k)/SQR(length);
    y_l += cos(theta)*(force_k-sumn_k)/SQR(length);

  /* turning of fiber */

  theta += dtheta;

  /* reduction in force and stress due to new orientation */

  force_k = delta_l*SQR(length)*cos(theta);

  for(i=1;i<=N;i++)
    stress_k[i] = stressn_k[i]*cos(theta)/cos(theta-dtheta);

  }
  while(theta < 89.9/180*PI);
  printf("%10.6f %10.6f %10.6f \n",theta*180.0/PI,x_l,y_l);
  fprintf(out_file,"%e\t%e\t%e\n",theta*180.0/PI,x_l,y_l);

  fclose(out_file);
  free_vector(stressn_k,1,N);
  free_vector(stress_k,1,N);
  exit(0);
}

#undef PI
#undef N
#undef SQR(a)
#undef CUBE(a)
```

APPENDIX B

DISCREET TIME DEPENDENT MODEL

```
/*
  This program numerically simulates a time_dependent discreet model of
  drag induced orientation of a massless rigid fiber moving in a
  poro-elastic media.

  1) Given parameter values, a 4th order Runga-Kutta integrator is run to
     numerically simulate a set of ODE's.
*/

#include <stdio.h>
#include <math.h>
#include"nr.h"
#include "nrutil.h"

#define PI 3.14159265
#define SQR(a) ((a)*(a))
#define CUBE(a) ((a)*(a)*(a))
#define N 100

main()
{
  int i, drag_flag;
  float *stress_k,*stressn_k,force_k,theta,moment_k;
  float length,sumn_k,dtheta;
  float x_l,y_l,old_theta,delta_l;
  float time,time_old,dt,damp,force,damp_ratio,time_end,time_incr;
  FILE *out_file, *fopen();

  /* Allocate output space for integration */

  stress_k = vector (1,N);
  stressn_k = vector (1,N);
  x_l = 0.0;
```

```
y_l = 0.0;
time = 0.0;

printf(" Ratio of Delta/Length?: ");
scanf("%f", &delta_l);
printf(" Force which gives delta?: ");
scanf("%f", &force);
printf(" Body force [0] or drag force [1]?: ");
scanf("%i", &drag_flag);
printf(" Length?: ");
scanf("%f", &length);
printf(" Damping in the parallel direction?: ");
scanf("%f", &damp);
printf(" Perpendicular/Parallel Damping?: ");
scanf("%f", &damp_ratio);
printf(" Inital Theta?: ");
scanf("%f", &old_theta);
printf(" Simulate time [sec]?: ");
scanf("%f", &time_end);
printf(" Output time increments [sec]?: ");
scanf("%f", &time_incr);
theta = old_theta/180*PI;
old_theta = theta - 1.0;
force_k = cos(theta)*delta_l*SQR(length);

/* Set inital conditions */

for(i=1;i<=N;i++) {stress_k[i] = force_k/length;}
time_old = -time_incr-1.0;

if((out_file = fopen("dscrt.out", "w")) == NULL)
    printf("*** DSCRT.OUT could not be opened. ***\n");
fprintf(out_file, "%s\t%s\t%s\t%s\n", "Time [sec]","X [mm]","Y [mm]",
     "Theta [deg]");
do
  {
  if ((time-time_old)  > time_incr)
    {
    printf("%10.6f %10.6f %10.6f %10.6f \n"
     ,time,theta*180.0/PI,x_l*length,y_l*length);
    fprintf(out_file, "%10.4f\t%e\t%e\t%e\n", time,x_l*length,y_l*length
     ,theta*180/PI);
    time_old = time;
    }

  /* slip fiber */

  stressn_k[1] = 0.0;
  for(i=2;i<=N;i++)
    stressn_k[i] = stress_k[i-1];
  x_l += 1.0/N*cos(theta);
  y_l += 1.0/N*sin(theta);

  /* turning */

  moment_k = 0.0;
  for(i=1;i<=N;i++)
    moment_k += (-length/2.0 + length/N/2 + length/N*(i-1))
```

```
      *stressn_k[i]*length/N;
    dtheta = 12.0*moment_k/CUBE(length);

    /* new stress */
    /* due to turning */

    for(i=1;i<=N;i++)
      stressn_k[i] += (length/2.0 - length/N/2 -  length/N*(i-1))
       *dtheta;

    /* due to reduction in supporting stress */

    sumn_k = 0.0;
    for(i=1;i<=N;i++)
      sumn_k += stressn_k[i]*length/N;

    /* reduction in stress due to reduction in force */

    for(i=1;i<=N;i++)
      stressn_k[i] += (force_k-sumn_k)/length;

    x_l -= sin(theta)*(force_k-sumn_k)/SQR(length);
    y_l += cos(theta)*(force_k-sumn_k)/SQR(length);

    if (drag_flag > 0)
      dt = length/N/(0.612*force*sin(theta)/damp);
    else
      dt = length/N/(force*sin(theta)/damp);

    time += dt;

    x_l -= 1.0/damp_ratio/N*cos(theta);
    y_l += 1.0/damp_ratio/N/tan(theta)*cos(theta);

    theta += dtheta;
    force_k = delta_l*SQR(length)*cos(theta);

    for(i=1;i<=N;i++)
      stress_k[i] = stressn_k[i]*cos(theta)/cos(theta-dtheta);

    }
  while(time < time_end);

  printf("%10.6f %10.6f %10.6f %10.6f \n"
       ,time,theta*180.0/PI,x_l*length,y_l*length);
  fprintf(out_file, "%10.4f\t%e\t%e\t%e\n", time,x_l*length,y_l*length
       ,theta*180/PI);

  fclose(out_file);
  free_vector(stressn_k,1,N);
  free_vector(stress_k,1,N);
  exit(0);
}

#undef PI
#undef N
#undef SQR(a)
#undef CUBE(a)
```